

Accelerating the Development of LLZO in Solid-State Batteries Toward Commercialization: A Comprehensive Review

Yang Wang, Zhen Chen,* Kai Jiang, Zexiang Shen, Stefano Passerini,* and Minghua Chen*

Solid-state batteries (SSBs) are under development as high-priority technologies for safe and energy-dense next-generation electrochemical energy storage systems operating over a wide temperature range. Solid-state electrolytes (SSEs) exhibit high thermal stability and, in some cases, the ability to prevent dendrite growth through a physical barrier, and compatibility with the “holy grail” metallic lithium. These unique advantages of SSEs have spurred significant research interests during the last decade. Garnet-type SSEs, that is, $\text{Li}_7\text{La}_3\text{Zr}_2\text{O}_{12}$ (LLZO), are intensively investigated due to their high Li-ion conductivity and exceptional chemical and electrochemical stability against lithium metal anodes. However, poor interfacial contact with cathode materials, undesirable lithium plating along grain boundaries, and moisture-induced chemical degradation greatly hinder the practical implementation of LLZO-based SSEs for SSBs. In this review, the recent advances in synthesis methods, modification strategies, corresponding mechanisms, and applications of garnet-based SSEs in SSBs are critically summarized. Furthermore, a comprehensive evaluation of the challenges and development trends of LLZO-based electrolytes in practical applications is presented to accelerate their development for high-performance SSBs.

have triggered the development of solid-state batteries (SSBs),^[1] as one of the most promising secondary batteries to replace the traditional lithium-ion batteries (LIBs).^[2] In general, SSBs utilize lithium metal anode and solid-state electrolytes (SSEs) instead of graphite anode, organic liquid electrolyte, and separator that are used in commercial LIBs. The revival of lithium metal anode and high-safety batteries largely relies on developing SSEs with high thermal stability and mechanical strength, especially for the inorganic electrolytes. Nevertheless, the practical applications of SSEs for SSBs not only require complex and rigorous physical/chemical properties (e.g. high Li-ion conductivity (σ_{Li^+}) ($> 10^{-4} \text{ S cm}^{-1}$), high stability in the air, high chemical/electrochemical stability against lithium metal anode, sufficient interfacial contact with cathodes), they should also offer the features of easy manufacturing, low cost, and the ability for mass production. Unfortunately, no existing SSE can satisfy all these requirements.^[3] The urgency and

overwhelming complex challenges cause the exponential growth of research efforts on SSEs.^[4]

Up to now, numerous SSE materials have been developed, including sulfides (i.e., $70\text{Li}_2\text{S}\cdot 30\text{P}_2\text{S}_5$, $\text{Li}_{10}\text{GeP}_2\text{S}_{12}$), oxides (i.e.,

1. Introduction

The growing demands for safe, energy-dense, long lifespan, and wide operating temperature range energy storage technologies

Y. Wang, Z. Chen, K. Jiang, Z. Shen, M. Chen
Key Laboratory of Engineering Dielectric and Applications (Ministry of Education)
School of Electrical and Electronic Engineering
Harbin University of Science and Technology
Harbin 150080, China
E-mail: chen.zhen@hrbust.edu.cn; mhchen@hrbust.edu.cn

K. Jiang
State Key Laboratory of Advanced Electromagnetic Engineering
School of Electrical and Electronic Engineering
Huazhong University of Science and Technology
Wuhan 430074, China
S. Passerini
Helmholtz Institute Ulm (HIU)
Helmholtzstrasse 11, D-89081 Ulm, Germany
E-mail: stefano.passerini@kit.edu

S. Passerini
Karlsruhe Institute of Technology (KIT)
P.O. Box 3640, D-76021 Karlsruhe, Germany
S. Passerini
Sapienza University of Rome
Chemistry Department
P. Aldo Moro 5, Rome 00185, Italy

 The ORCID identification number(s) for the author(s) of this article can be found under <https://doi.org/10.1002/smll.202402035>

© 2024 The Author(s). Small published by Wiley-VCH GmbH. This is an open access article under the terms of the [Creative Commons Attribution License](https://creativecommons.org/licenses/by/4.0/), which permits use, distribution and reproduction in any medium, provided the original work is properly cited.

DOI: 10.1002/smll.202402035

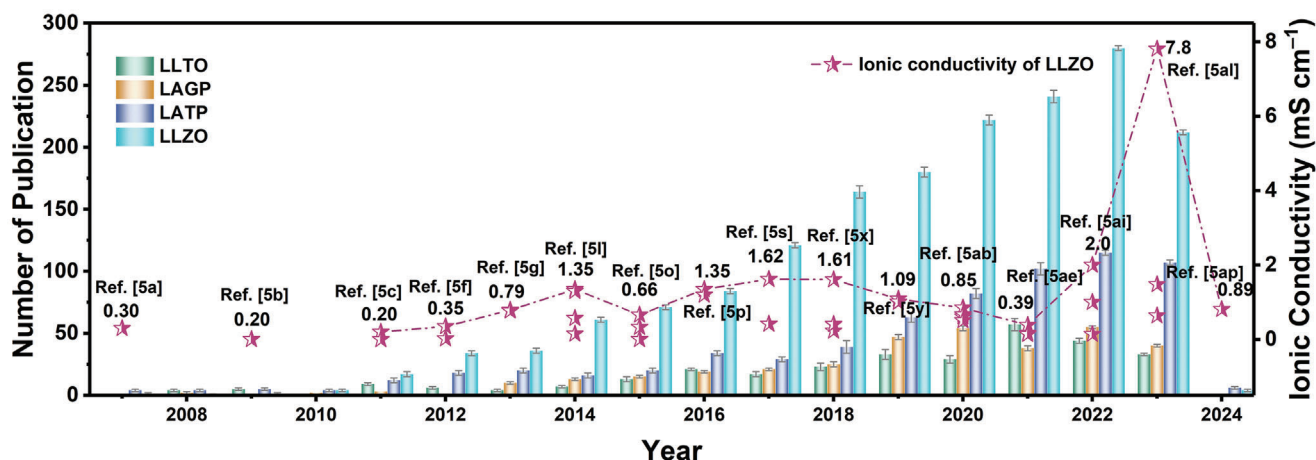


Figure 1. The number of published articles on four common oxide solid-state electrolytes from 2007 until 2023 (retrieval time: January 14, 2024); and the development of room temperature ionic conductivity over time from 2007 to 2024.^[5]

$\text{Li}_{0.34}\text{La}_{0.51}\text{TiO}_{2.94}$, $\text{Li}_{1.3}\text{Al}_{0.3}\text{Ti}_{1.7}(\text{PO}_4)_3$ and $\text{Li}_5\text{La}_3\text{M}_2\text{O}_{12}$ ($\text{M} = \text{Nb}$, Ta , and Zr) and halides (i.e., Li_3YCl_6 , Li_3YBr_6), etc. The ionic conductivity of sulfide electrolytes is generally the highest ($1.2 \times 10^{-2} \text{ S cm}^{-1}$),^[6] reaching and even exceeding the level of liquid organic electrolytes.^[7] Unfortunately, the progress of sulfide electrolytes is largely hindered by their high sensitivity against moist air causing the generation of toxic gas (i.e., H_2S), and their instability with both cathode and anode leading to severe battery degradation upon cycling. Similarly, halide electrolytes exhibit high ionic conductivity ($>1 \text{ mS cm}^{-1}$), superior oxidation stability, and good mechanical properties, they can directly adopt cold sintering to achieve tight solid-solid contact. However, halide electrolytes absorb water quickly and liquefy within hours because of the high sensitivity in a natural air environment. The oxides can be divided into four categories: garnet family ($\text{Li}_7\text{La}_3\text{Zr}_2\text{O}_{12}$ (LLZO)), perovskite ($\text{Li}_{3x}\text{La}_{(2/3-x)}\text{TiO}_3$ (LLTO)), NASICON-type phosphates ($\text{Li}_{1+x}\text{Al}_x\text{Ti}_{2-x}(\text{PO}_4)_3$ (LATP) and $\text{Li}_{1+x}\text{Al}_x\text{Ge}_{2-x}(\text{PO}_4)_3$ (LAGP)) and LISICON. The NASICON- and perovskite-type oxides generally exhibit superior stability in air, whereas the garnet-type oxides are known for their chemical instability against moist air resulting in the formation of LiOH and Li_2CO_3 . However, the garnet oxides display good chemical/electrochemical stability toward lithium metal. In contrast, the NASICON- and perovskite-type oxides suffer severe side reactions with lithium metal.^[5ac]

Perovskite-type LLTO possesses a very high bulk conductivity ($1 \times 10^{-3} \text{ S cm}^{-1}$ at room temperature (RT)). However, due to the barrier effect of the grain boundary (GB), the overall ionic conductivity of LLTO ($1 \times 10^{-5} \text{ S cm}^{-1}$) is significantly lower than that of single crystal material. Moreover, the spontaneous reduction of Ti^{4+} in LLTO with Li metal forbids their direct contact. LATP and LAGP are well known NASICON-type SSEs. LATP can conduct both sodium ions and lithium ions, with high ionic conductivity (close to $1 \times 10^{-3} \text{ S cm}^{-1}$ at 298 K), low density ($\approx 2.9 \text{ g cm}^{-3}$), and excellent stability in water and air (due to strong P—O bonds). However, Ti^{4+} is also easily reduced to Ti^{3+} because LATP is thermodynamically unstable when in contact with Li metal anode. The aggressive and continuous reduction reactions form reactants (P, LiTiPO_5 , AlPO_4 , Li_3PO_4) that precipi-

tate at the SSE/Li interface forming mixed ion-electron conductive interphases, destabilizing the electrolyte material. A similar two-step chemo-mechanical process of the interface degradation (reactants containing Ge, GeO_2 , $\text{Li}_4\text{P}_2\text{O}_7$, AlPO_4) takes place at the LAGP/Li interface.^[8] LISICON-type electrolytes have been reported less frequently in battery systems due to their relatively low ionic conductivity ($10^{-7} \text{ S cm}^{-1}$ at RT) and poor stability in contact with lithium and air. Although some doping elements have been proposed to improve the ionic conductivity, the results are not satisfactory.^[9] In contrast, cubic- $\text{Li}_7\text{La}_3\text{Zr}_2\text{O}_{12}$ (c-LLZO) stands out among other garnet electrolytes and other oxides SSE due to its high RT ionic conductivity ($\approx 10^{-4}$ – $10^{-3} \text{ S cm}^{-1}$), low activation energy, high thermal stability against lithium metal (LLZO > LLTO > LATP > LAGP),^[10] and high electrochemical stability (electrochemical window above 5 V).^[11] Li-garnet ($\text{Li}_5\text{La}_3\text{M}_2\text{O}_{12}$ ($\text{M} = \text{Nb}$, Ta)) was first reported by Thangadurai et al. in 2003.^[12] Following the discovery of garnet solid-state electrolyte by Weppner et al.^[5a] in 2007 and its first application in polyethylene oxide (PEO) based composite solid electrolyte (CSE) in 2015,^[13] considerable research efforts have been conducted focusing on the commercialization process of LLZO. Evident from the growing publication number between 2007 and 2023 (Figure 1) and the fruitful achievements since the pioneering work discovered in 2003 (Figures 1 and 2), LLZO has great potential for use in SSBs with high power/energy density due to its numerous attractive features.^[14]

Herein, garnet SSEs are reviewed outlining the synthesis methods of LLZO with different morphologies and structures, as well as the advantages and disadvantages of differing methods, to propose approaches with greater applicability. Meanwhile, starting with LLZO, the Li^+ transfer pathways of garnet SSEs are systematically summarized, followed by an overview of the methods as well as the in-depth mechanism to improve both their grain boundary and bulk ionic conductivities. For potential practical applications, a comprehensive investigation of LLZO is carried out based on two of their major applications in lithium metal batteries, that is as a Li^+ conductor within positive electrodes and as a solid-state electrolyte. The former case covers the aspects of serving as a coating layer of cathode active materials,

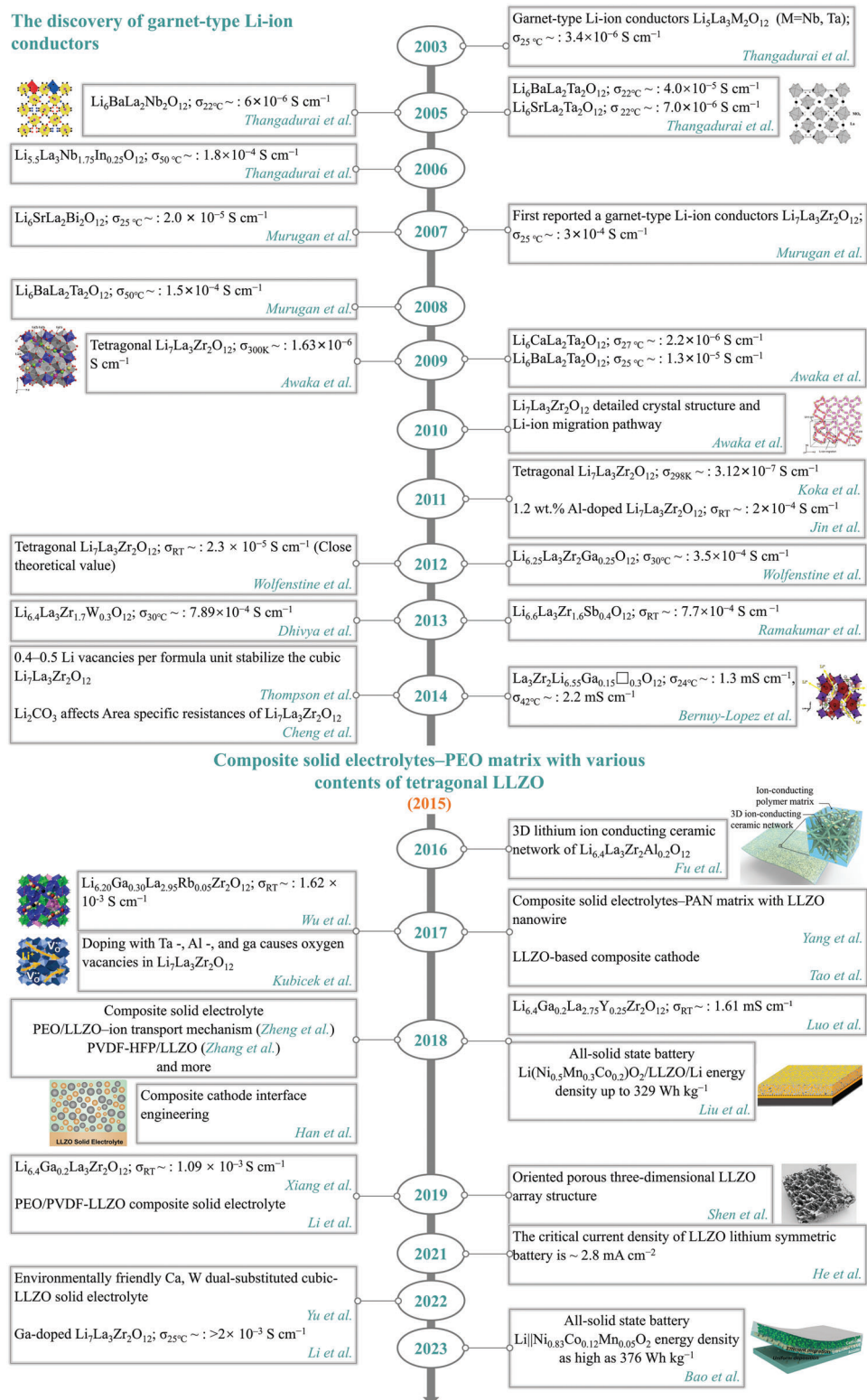


Figure 2. Overview of the chronological development of garnet-type SSEs. Reproduced with permission.^[15a] Copyright 2005, Wiley. Reproduced with permission.^[15b] Copyright 2005, Wiley. Reproduced with permission.^[5b] Copyright 2009, Elsevier. Reproduced with permission.^[15g] Copyright 2011, Wiley. Reproduced with permission.^[5i] Copyright 2014, American Chemical Society. Reproduced with permission.^[15r] Copyright 2016, National Academy of Sciences. Reproduced with permission.^[15s] Copyright 2017, American Chemical Society. Reproduced with permission.^[15j] Copyright 2017, American Chemical Society. Reproduced with permission.^[15w] Copyright 2018, Elsevier. Reproduced with permission.^[15s] Copyright 2018, Elsevier. Reproduced with permission.^[15o] Copyright 2019, The Royal Society of Chemistry. Reproduced with permission.^[15u] Copyright 2023, Wiley.^[5a–e,g–i,s,x,y,ai,12,13,15]

and as a catholyte to provide 3D Li⁺-conducting networks in the positive electrode. The standing problems and solutions of inorganic solid electrolytes (ISEs) and CSEs are also reviewed. Different challenges (e.g. insufficient chemical/electrochemical stability, relatively inferior ionic transportation properties, poor electrode/electrolyte interfacial contact, and non-uniform Li⁺ flux-induced dendrite growth) are interconnected and thus should be considered when conceiving the design strategies. Furthermore, the realization of mass production of LLZO-based SSEs requires evaluation of their scalability, controllability, cost, as well as practical performance when integrated into SSBs. This review summarizes the progress of LLZO from its synthesis, modification, and application, offering a robust framework for realizing LLZO-based SSBs with high power density, energy density, and safety.

2. Morphological Controlled Synthesis Methods of LLZO-Based Materials

The industrialization of garnet LLZO requires finding a process that enables the production of materials in large quantities and with high quality. In this section, the general synthesis routes, corresponding advantages, and disadvantages are thoroughly discussed, especially the critical progress of morphologically controlled 0D particles, 1D fibers, 2D sheets, and 3D frameworks. Relevant synthesis methods that have emerged recently are also reviewed. For each method, the key challenges for practical applications are outlined.

2.1. 0D Particles

2.1.1. Solid-State Reaction (SSR) Method

The SSR is the most promising method for mass production of LLZO coarse powders, which are ground into submicron particles before sintering to increase their activity.^[16] To check the quality of synthesized coarse powder (i.e., ionic conductivity), some synthesis-related research usually involves the preparation and performance test of the pellet. Because the contact of LLZO with water causes Li⁺/H⁺ ion-exchange and releases LiOH,^[17] the ion-exchanged LLZO powder is thermodynamically unstable, resulting in decomposition during the sintering process. Organic solvents such as ethanol or isopropanol are commonly used in the grinding process. However, for large-scale industrial production, organic solvents present limitations such as poor safety, high cost, and difficulty in recovery. Huang et al.^[18] replaced the organic solvent with a water-based solvent as the grinding media to prepare Ta-doped LLZO and additional LiOH was added to the water to prevent the ion-exchange (Figure 3a,b). The utilization of water instead of highly volatile organic solvents ensures the high safety feature of this method. Meanwhile, the relatively low sintering temperature (900–1000 °C) reduces the risk of combustion and explosion, avoids abnormal grain growth,^[19] and can directly synthesize nano-particles.^[20] Nonetheless, this approach is limited because the large-scale synthesis through reversible reaction cannot guarantee high uniformity and will generate impurity phases.

2.1.2. Pechini Method

The Pechini method uses carboxylic acids (citric acid, tartaric acid, polyacrylic acid, etc.) and metal ions to form complexes, and then uses metal carboxylic acid complexes and polyhydroxy alcohols (ethylene glycol, glycerol, polyvinyl alcohol etc.) to heat for polyester reaction to form combustible polymers, which can chelate metal ions by the presence of carboxylic acid. Compared with the traditional sol–gel method (see the discussion later in Section 2.1), the biggest advantage of the Pechini method is that the transition metal elements have stronger dispersion. Fe-doped LLZO (1–3 μm), Al-doped LLZO, or Ga-doped LLZO (40–50 nm) powders were successfully synthesized by this method.^[21] However, the cost is generally high, the precursor raw materials are harmful, and the reaction involves a large number of process variables that hinder its further expansion and application.

2.1.3. Sol–Gel Method

The conventional sol–gel method uses uniformly mixed metal nitrate, citric acid, and ethylene glycol as reaction precursors to form a gel with extensive metal-oxygen bonds and subsequently is subjected to a calcination step in Ar atmosphere to obtain LLZO nano-particles (Figure 3c).^[22] The sol–gel method is known as a suitable method for the synthesis of small-size particles. Cheng et al.^[23] compared the air sensitivity, densification rate, interface impedance, and cycling performance of LLZO with varying particle size (large: 100–200 μm; small: 20–40 μm). It was determined that small-particle LLZO is more stable in air and can resist the reaction with ambient CO₂ and water vapor. Meanwhile, it also shows lower interfacial resistance, higher densification rate, and enhanced cycling behavior than those of the large-particle LLZO.^[24] According to Kim et al.,^[25] it is also revealed that sol–gel derived LLZO with an average grain size of 260 nm has higher total conductivity at higher temperatures than those prepared by the SSR method (average grain size: 3.3 μm). However, the sol–gel-derived LLZO exhibits much higher activation energy than that of the SSR-derived LLZO activation energy (0.41 versus (vs) 0.26 eV). This is contrary to the previous research results that high ionic conductivity corresponds to a low activation energy, which can be seen from the examples summarized in Table 1. Meanwhile, this conclusion is in line with the Arrhenius equation.^[26] The citrate-nitrate method is also a new sol–gel preparation method, which involves the blending and burning of metal nitrate and citric acid. The citrate-nitrate method is simpler, because one reaction precursor is omitted when compared with the traditional sol–gel method, and one-step polyester reaction is omitted when compared with the Pechini method.^[27] Notably, the raw materials and solvents used in the sol–gel method are organic matter, which raises the overall cost and causes more damage to the environment, thereby the sol–gel method is not suitable for large-scale production.

2.1.4. Combustion Synthesis (CS) Method

Most synthetic precursors of the traditional sol–gel method are metal nitrates, which generate a lot of excess heat during the calcination process and are prone to combustion and explosion.^[28]

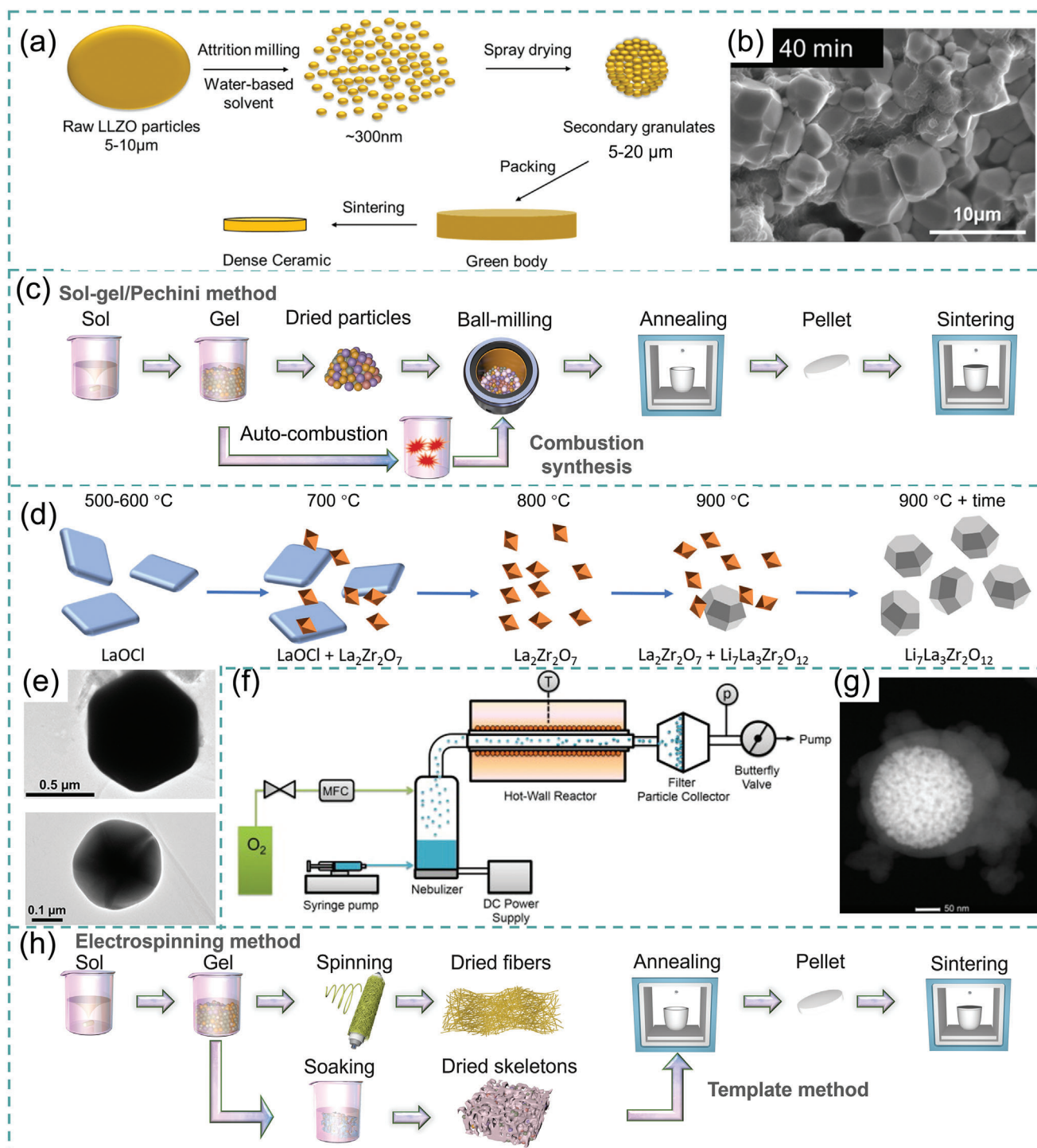


Figure 3. a) Scheme for attrition milling and spray drying; b) The cross-sectional microstructure of sample. Reproduced with permission.^[18] Copyright 2018, American Chemical Society. c) Synthesis scheme of LLZO based on the Pechini, sol-gel, and combustion methods; d) Overall formation process of $\text{Li}_7\text{La}_3\text{Zr}_2\text{O}_{12}$ in eutectic $\text{LiCl}:\text{KCl}$; e) Transmission electron microscopy (TEM) images showing faceted particles of c-LLZO. Reproduced with permission.^[5v] Copyright 2018, American Chemical Society. f) NSP experimental setup; g) Scanning transmission electron microscopy image of $\text{Li}_{6.7}\text{La}_3\text{Zr}_2\text{Al}_{0.1}\text{O}_{12}$. Reproduced with permission.^[37] Copyright 2014, Elsevier. h) Synthesis scheme of LLZO based on the electrospinning method and template method.

Table 1. Advantages and disadvantages of various synthesis methods.

Preparation methods		Advantages	Disadvantages	Morphology
Solid-based	SSR	<ul style="list-style-type: none"> • Easy to scale up 	<ul style="list-style-type: none"> • High sintering temperature • Long ball milling time 	0D
Liquid-based	Pechini	<ul style="list-style-type: none"> • More dispersible transition metal ions 	<ul style="list-style-type: none"> • High cost • Harmful precursor materials • Large number of process variables 	0D
	Sol-gel	<ul style="list-style-type: none"> • Low sintering temperature 	<ul style="list-style-type: none"> • High cost • Low security • Long preparation time 	0D
	CS	<ul style="list-style-type: none"> • Simple process • Fast preparation 	<ul style="list-style-type: none"> • High cost 	0D, 2D, and 3D
	Co-pre.	<ul style="list-style-type: none"> • Short production cycle • Low cost 	<ul style="list-style-type: none"> • Possible agglomeration 	0D
	MSS	<ul style="list-style-type: none"> • Low crystallization temperature • Low cost 	<ul style="list-style-type: none"> • High requirements for raw material selection 	0D
	NSP	<ul style="list-style-type: none"> • No organic solvents • Simple process • Low cost 	<ul style="list-style-type: none"> • High requirements for equipment and operation 	0D, 2D, and 3D
	Electrospinning	<ul style="list-style-type: none"> • Low sintering temperature • Simple process • Controlled morphology 	<ul style="list-style-type: none"> • Low yield • Unfriendly environment 	1D, 3D
	Template	<ul style="list-style-type: none"> • Controlled morphology • Simple process 	<ul style="list-style-type: none"> • Limited template material 	2D, 3D

Solution combustion, on the other hand, is relatively safe because it is based on the gelation and subsequent combustion of an aqueous solution containing the required metal salts and organic fuels (Figure 3c). For example, Weller et al.^[5ac] proposed a combustion synthesis method, the carbonaceous foam formed by combustion provides an in situ sacrificial template for the reaction, which controls the size of the LLZO particles. The aforementioned method, however, faces the same challenge of high cost as the traditional sol-gel method and requires the selection of a suitable fuel that does not introduce impurity phases. Therefore, selecting combustion agents poses a challenge for this method.

2.1.5. Co-Precipitation (Co-pre.) Method

Co-precipitation is a method that involves two or more homogeneous solution components that are simultaneously precipitated with a precipitating agent. In general, soluble salts of various metal elements are used as raw materials, such as lithium nitrate, lanthanum nitrate hexahydrate, zirconium nitrate, etc. The precipitation agent is usually ammonia water. The raw materials of co-precipitation are usually inorganic substances with lower cost than metallic organics.^[29] Different from the sol-gel method, the co-precipitation method can obtain several components simultaneously.^[30] $\text{Li}_7\text{La}_3\text{Zr}_2\text{O}_{12}$ ($\approx 0.5\text{--}1\ \mu\text{m}$) and $\text{Li}_{6.75}\text{La}_3\text{Zr}_{1.75}\text{Ta}_{0.25}\text{O}_{12}$ ($\approx 2\text{--}3\ \mu\text{m}$) were prepared by the co-precipitation method.^[31] However, nitrate is easy to absorb moisture in the air, and is easily decomposed by heat to produce oxygen. Compared with oxide raw materials, the storage conditions are strict, which will increase the cost to a certain extent. In addition, the use of ammonia increases the environmental burden and poses certain safety risks. Therefore, the co-precipitation

method is not regarded as the best choice for industrial production.

2.1.6. Molten Salt Synthesis (MSS) Method

MSS is an efficient method to synthesize garnet SSEs. It utilizes a salt or salt mixture heated above its melting point as a precursor solvent, which in turn generates products through dissolution, precipitation, and crystal growth.^[32] Compared with the sol-gel and co-precipitation methods, the advantages of MSS include the cheaper raw materials, the relatively lower crystallization temperature, and the well-controlled particle size and morphology.^[33] Zhang et al.^[34] demonstrated that the MSS is an effective and low-cost method that not only greatly reduces the material mixing time to <30 min but enables mass production. Zhang et al.^[35] demonstrated fast mass transport and diffusion in the molten salt phase, fine $\text{Li}_{6.25}\text{Al}_{0.25}\text{La}_3\text{Zr}_2\text{O}_{12}$ powders can be prepared at low reaction temperature (950 °C). Weller et al.^[5v] synthesized LLZO with primary particle sizes ranging from 0.3 to 3 μm in a less volatile salt (LiCl: KCl) eutectic mixture (Figure 3d,e). Studies have shown that the evaporation of the reaction medium (such as salt and solvent) will damage the uniformity and morphology of the obtained powder. In this regard, it is best to choose less volatile salts. Therefore, the challenges of this molten salt method predominantly lie in the material selection.

2.1.7. Nebulized Spray Pyrolysis (NSP) Method

NSP is an aerosol-based synthesis method that produces ceramic powders directly from the solution and obtains a high

production yield (98%) and relatively high production rate ($\approx 0.3 \text{ g h}^{-1}$) on a laboratory scale.^[36] Compared to other solution-based technologies, NSP technology can significantly reduce or even avoid the use of organic solvents. Furthermore, the thermal decomposition and annealing of NSP occur simultaneously so that the nanocrystalline powder is free of organic residues, excluding the need for a time-consuming annealing process and thus greatly reducing the cost. Djenadic et al.^[37] successfully fabricated Al-doped $\text{Li}_7\text{La}_3\text{Zr}_2\text{O}_{12}$ SSE using NSP. According to the reaction principle (Figure 3f,g), the ultrasonic generator is used to atomize the prepared precursor solution in the glass chamber. The injection pump delivers the precursor solution continuously at a constant rate. A mist of precursor solution is transported to a hot-wall reactor with the aid of flowing oxygen. Nano-particles are synthesized at high temperatures (900 °C) and collected using a filter-based collector. The NSP approach is more intelligent and reduces labor costs, which makes it more attractive than the SSR process. However, the NSP method requires high temperature, vacuum condition, sophisticated equipment, and precise operational procedures, making it unsuitable for industrial applications.

2.2. 1D Fibers

Generally, the fabrication methods for 1D inorganic compounds include the electrospinning method and template method (Figure 3h). The electrospinning device consists of a syringe with a needle, a metal collector, and a power supply. The electrospinning method is similar to the sol-gel method in principle because its precursor is prepared based on the sol-gel method that involves some polymer (such as polyvinyl pyrrolidone) as a thickening agent to obtain a viscous solution. First, the precursor solution is loaded into a syringe in advance to expel air. Then, a voltage is applied to the needle and the receiver is grounded. As the droplets are charged, they are then pulled into filaments under an electric field and collected by a collector to obtain felts. Finally, LLZO fibers with high ionic conductivity are obtained by further sintering the fiber felt with the solvent removed.^[38] This method has been shown to synthesize pure phase c-LLZO (Figure 4a–c).^[52,39] However, with a typical production rate of $0.08\text{--}0.1 \text{ g h}^{-1}$ using single-needle electrospinning; a very long spinning time is required to obtain enough materials for material characterization and performance evaluation of LLZO-based SSEs in SSBs.^[40] Due to its limited scalability in LLZO production, this method is primarily employed for laboratory-scale investigations. In addition to the electrospinning method, LLZO fibers can also be obtained via a template method. First, by impregnating the template materials into a sol-gel precursor solution and removing the template via calcination, the final LLZO fibers can be obtained (Figure 4d).^[41] For instance, naturally biomass Kapok fibers served as a template for the successful synthesis of LLZO fiber (Figure 4e).^[42] The advantage of the template method is that it can derive products of different dimensions by selecting templates with different forms. However, any incomplete pre-treatment or post-treatment process will lead to impure byproducts.

2.3. 2D Sheets

Compared with 0D, 1D, and 3D fillers/frameworks, reports relating to 2D active ceramic fillers are relatively rare. At present, 2D LLZO is synthesized by water-based methods. Abdel Hamid et al.^[43] prepared the 2D sheet LLZO by sol-gel method using sucrose as a structure-directing agent. Specifically, sucrose was heated in the solution and polymerized, resulting in a brown “cupcake-like” foam from thermal decomposition. After further heating, the organic components were decomposed and oxidized into CO_2 and H_2O gases, and the uniformly distributed metal ions reacted and crystallized into LLZO, showing the flake shape morphology (Figure 4f). Song et al.^[44] reported, for the first time, the garnet $\text{Li}_{6.5}\text{La}_3\text{Zr}_{1.5}\text{Nb}_{0.5}\text{O}_{12}$ nanosheets by co-precipitation utilizing graphene oxide as the template (Figure 4g). Once the 2D nanosheet is thin enough, its advantages (for example, high specific surface area, ultra-thin lamellar structure, and large aspect ratio) can be brought into play, thus forming a larger contact area with the polymer, which is conducive to the transport of lithium ions and thus the enhanced ionic conductivity. Therefore, the primary goal of 2D nanosheets is to reduce the thickness. However, these water-based template sacrificial methods are not suitable for large-scale industrial production.

2.4. 3D Frameworks

There are also interconnected sintered structures made of fiber or sheet LLZO based on the template method. By adjusting the amount of natural cellulose, the interconnecting structure can be achieved during sintering. Therefore, this approach is primarily employed for the fabrication of a 3D LLZO framework.^[45] For example, according to Cai et al.,^[46] a 3D LLZO skeleton structure was obtained by using a porous sponge as a sacrifice template, which retained the structural characteristics of a porous sponge and provided a uniform pore structure for post-processing (Figure 5a,b). At the same time, Li et al.^[47] successfully fabricated a hierarchical “cellulose” garnet-type LLZO monolith by using a sacrificial template of natural cotton (Figure 5c). All the 3D porous structures obtained by the above methods are non-oriented. To shorten the ion diffusion pathways, a vertical array structure was also developed. Therein, the ice-template method is a common method to synthesize 3D array structures, including four processing steps: slurry preparation, solidification, sublimation, and sintering (Figure 5d).^[48] During the controlled solidification process, as the solvent solidifies, phase separation takes place, with the resulting solid phase (usually ice) serving as the template. Afterward, the solidified solvent template is removed by sublimation, while retaining the structural framework, resulting in a well-shaped vertical structure (Figure 5e).^[49] Because these 3D framework structures of LLZO usually do not have good self-supporting ability, polymer electrolytes are incorporated to construct organic-inorganic composite electrolytes (the details are analyzed in Section ‘3D LLZO Network’).^[50]

The advantages and disadvantages of synthesis methods are summarized in Table 1, from the perspectives of reducing cost, improving yield, and reducing pollutant emission, the traditional SSR method is an ideal method for LLZO synthesis, which

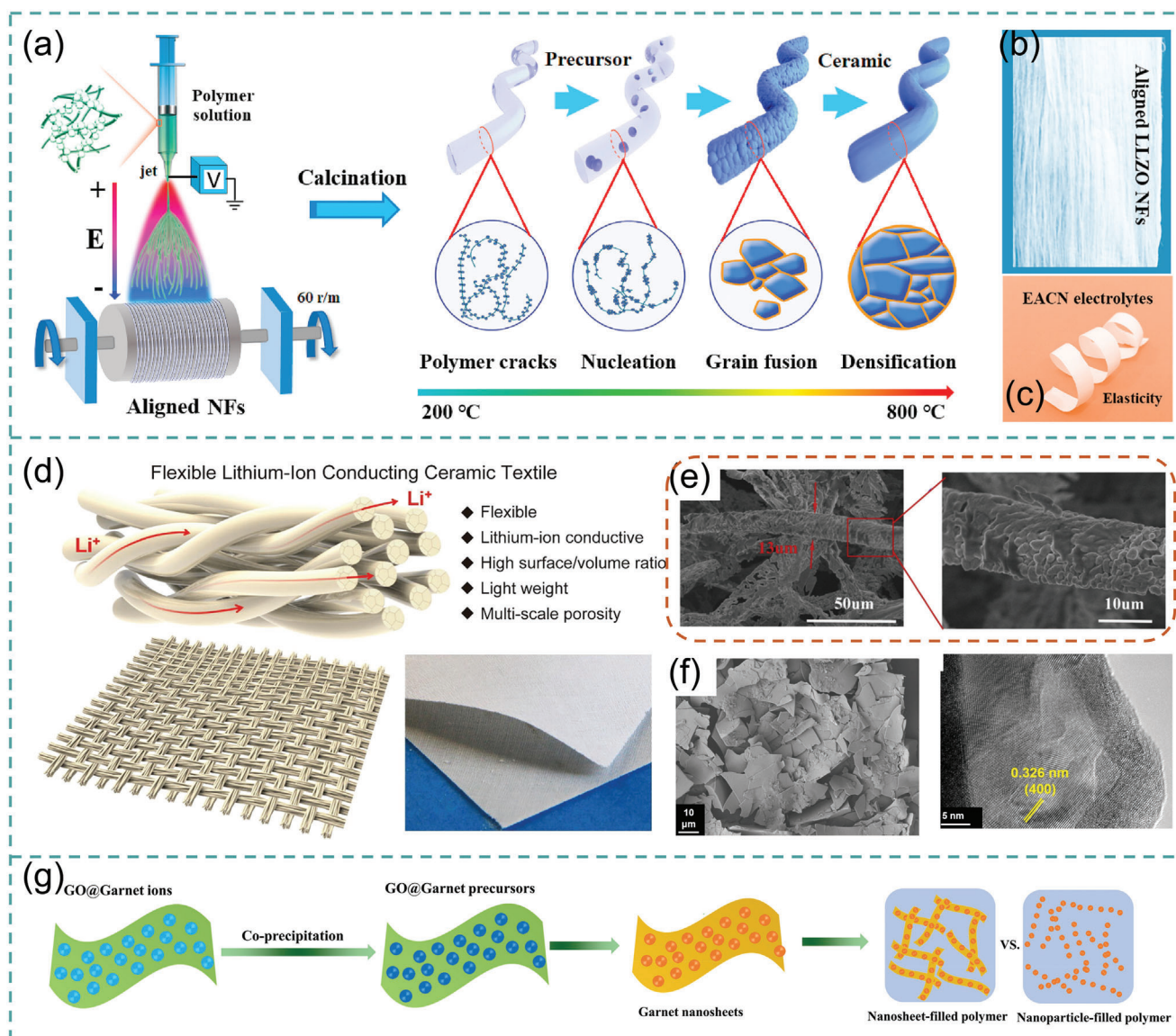


Figure 4. a) Overview of a sol-gel electrospinning method; Digital image of b) aligned $\text{Li}_{6.4}\text{La}_3\text{Zr}_2\text{Al}_{0.2}\text{O}_{12}$ membrane and c) electrolytes membrane. Reproduced with permission.^[52] Copyright 2019, Elsevier. d) Flexible lithium-ion conducting ceramic textile. Reproduced with permission.^[41] Copyright 2018, Elsevier. e) Scanning electron microscopy (SEM) images of LLZO fibers. Reproduced with permission.^[42] Copyright 2018, Elsevier. f) Field emission scanning electron microscopy (FESEM) (left) and TEM image (right) of LLZO sheets. Reproduced with permission.^[43] Copyright 2020, Elsevier. g) Schematic diagram of the preparation of garnet nanosheets. Reproduced with permission.^[44] Copyright 2019, American Chemical Society.

is most suitable for large-scale production.^[51] It is expected to achieve a breakthrough from a few grams, a few kilograms, or even hundreds of kilograms to tons of production.

3. Li-Ion Conductivity

LLZO has two types of crystal phases: tetragonal (t-LLZO) and cubic (c-LLZO) polymorph. The c-LLZO possesses higher Li-ion conductivity than that of the t-LLZO, but the cubic structure is unstable. Also, the intrinsic Li-ion conductivity of c-LLZO still cannot support the demand required for practical applications. To stabilize the c-LLZO and improve the Li-ion conductivity, various design strategies including element doping, the addition of

sintering additives, and increasing the particle density have been proposed.^[52]

3.1. Li-Ion Conduction Mechanism

Garnet-type electrolytes can be classified into four different subtypes: Li3 (i.e., $\text{Li}_3\text{Ln}_3\text{Te}_2\text{O}_{12}$, Ln = Y, Pr, Nd, Sm-Lu), Li5 (i.e., $\text{Li}_5\text{La}_3\text{M}_2\text{O}_{12}$, M = Nb, Ta), Li6 (i.e., $\text{Li}_6\text{LnLa}_2\text{M}_2\text{O}_{12}$, Ln = Ca, Sr, Ba; M = Nb, Ta), and Li7 (i.e., $\text{Li}_7\text{La}_3\text{M}_2\text{O}_{12}$, M = Zr, Sn, Ta). LLZO is a Li7 type SSE. Compared with the other three types (i.e., Li3 type, Li5 type, and Li6 type), the Li7 type LLZO exhibits one order of magnitude higher Li-ion conductivity (25 °C,

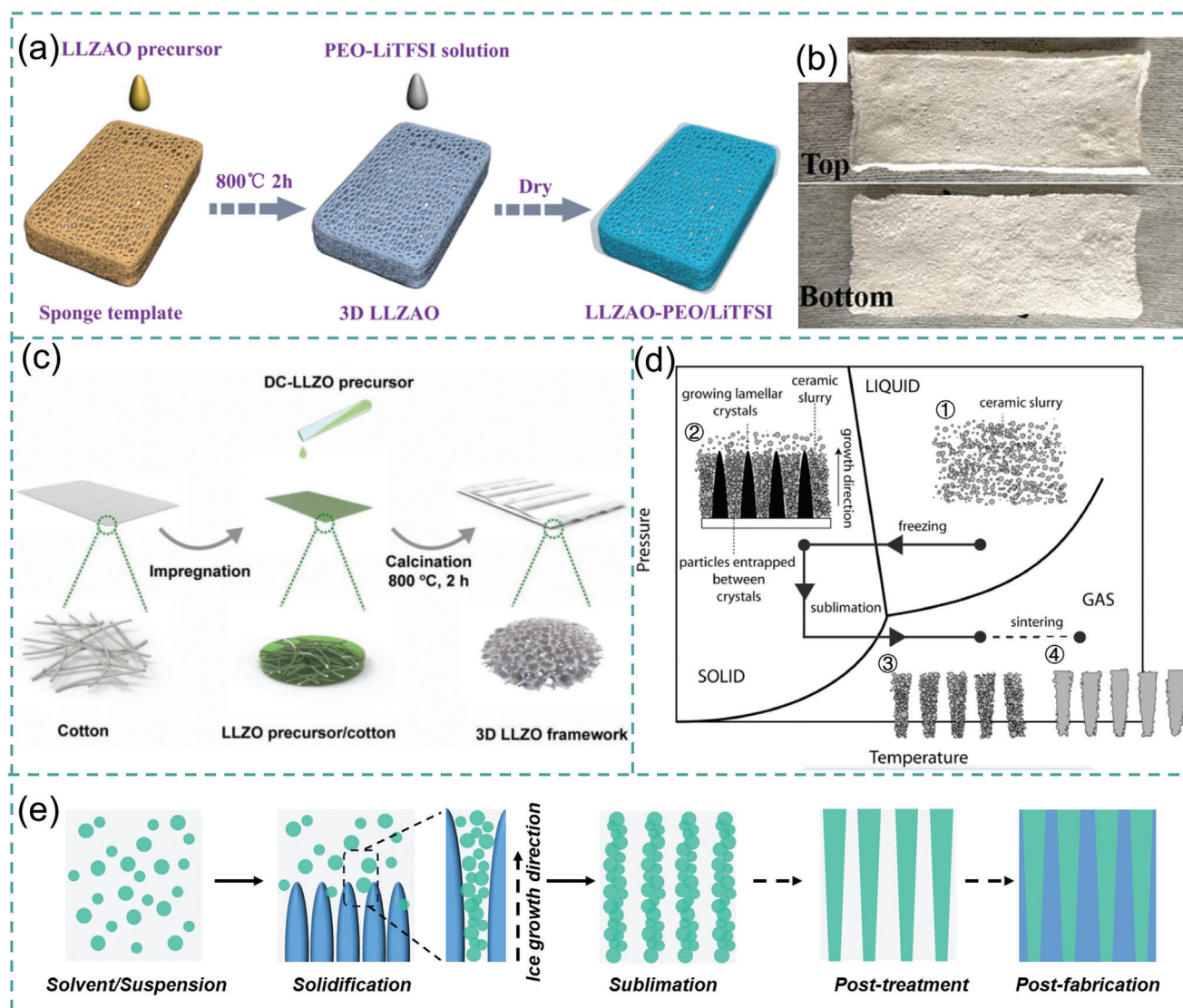


Figure 5. a) Schematic illustration for the synthesis of the composite electrolyte; b) Photographs showing the top and bottom view of the LLZO framework. Reproduced with permission.^[46] Copyright 2020, Elsevier. c) Schematic illustration for the preparation of the 3D LLZO framework. Reproduced with permission.^[47] Copyright 2019, Wiley. d) The four processing steps of freeze-casting: slurry preparation, solidification, sublimation, and sintering. Reproduced with permission.^[48] Copyright 2008, Wiley. e) Schematic illustration for the synthesis of the 3D framework via an ice-template method.

$3 \times 10^{-4} \text{ S cm}^{-1}$ vs $10^{-5} \text{ S cm}^{-1}$). The c-LLZO has disordered Li sites while the t-LLZO has fully ordered Li sites with 100% occupancy. It is confirmed that the crystal structure can significantly affect the Li-ion transport properties of LLZO. Specifically, the garnet skeleton structure consists of dodecahedral LaO_8 and octahedral ZrO_6 . The refined garnet framework reveals that La, Zr, and O atoms are located at the Wyckoff sites at 24c, 16a, and 96h, respectively. In the vacancies of the cubic framework structure, Li atoms occupy two types of crystal sites, for example, the tetrahedral 24d position (Li1) and the distorted octahedral 96h position (Li2), respectively (Figure 6a).^[15g] In an ideal garnet structure, the Li2 site is empty. The disorder and partial occupation of lithium atoms at the Li2 site greatly impact the Li-ion conduction.^[53] On the other hand, the t-LLZO comprises three types of occupied lithium ions, which completely oc-

cupy the corresponding 8a, 16f, and 32g lattice sites, with high symmetry. This high degree of symmetry of t-LLZO results in its total Li-ion conductivity (bulk and grain boundary) being 1–3 orders of magnitude lower than that of the c-LLZO due to the transformation of the space group from Ia-3d to I-43d.^[5b,54] However, Jayaraman et al.^[55] identified an inaccurate depiction of the Li3 atom in tetragonal LLZO as an octahedron. Through crystal structure investigation using VESTA software, it was determined that the Li3 atoms at the 32g site exhibited a “tetrahedral” configuration rather than the previously proposed “distorted octahedral” arrangement (Figure 6b). The ab initio calculations reported by Xu et al.^[56] uncover two possible pathways for Li-ion transport in a garnet framework: one bypasses the 24d tetrahedral sites and the other is via the 24d sites (Figure 6c). Meier’s calculations show that the motion of lithium ions in

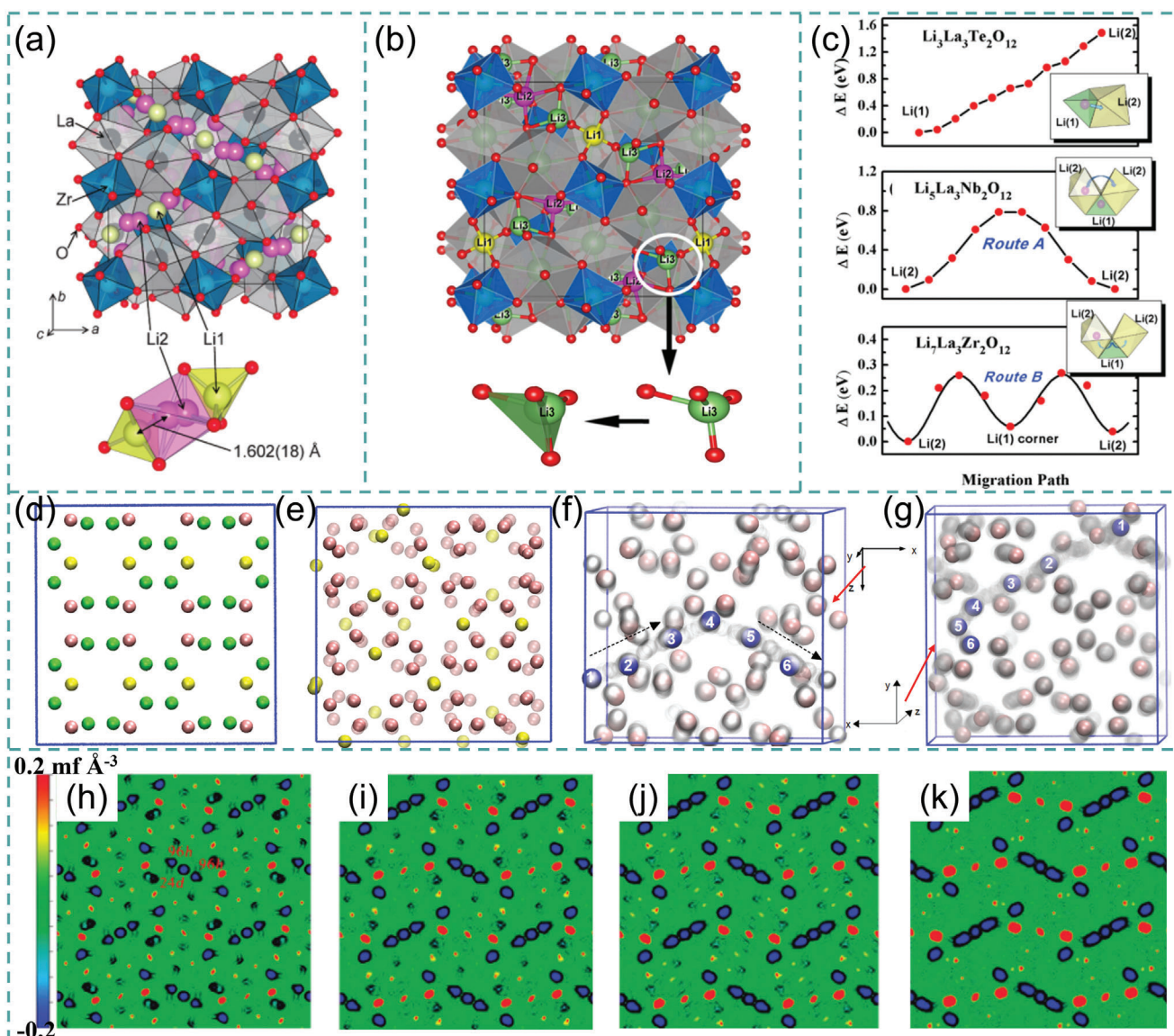


Figure 6. a) Crystal structure of c-LLZO (coordination polyhedral around the Li1 and Li2 sites. Reproduced with permission.^[158] Copyright 2011, Wiley. b) Crystal structure of tetragonal LLZO. Reproduced with permission.^[55] Copyright 2023, American Chemical Society. c) A plot showing the energy cost to move one Li^+ from the Li1 site to the neighboring Li2 site and two predominant mechanisms of Li^+ migration. Reproduced with permission.^[56] Copyright 2012, American Physical Society. Arrangement of Li ions in d) tetragonal and e) cubic LLZO model structure; Li-ion positions of f) tetragonal and g) cubic LLZO. Reproduced with permission.^[57] Copyright 2014, American Chemical Society. 2D contour maps sliced on the (001) plane with $z = 0.4$ at h) RT, i) 200, j) 400 and k) 600 °C. Reproduced with permission.^[58] Copyright 2012, Royal Society of Chemistry.

t-LLZO is fully collective or synchronized (Figure 6d,f), which requires higher activation energy. Whereas, in the case of c-LLZO it is an asynchronous mechanism dominated by single-ion jumping and induced collective motion with lower activation energies (Figure 6e,g).^[57] Han et al.^[58] studied the migration path of lithium ions and the change of lithium-ion motion with temperature by neutron diffraction technique and entropy maximization method. It is confirmed that the Li-ion displacements form a Li 3D diffusion pathway consisting of interlocking Li(24d) – Li(96h) – Li(48g) – Li(96h) – Li(24d) chain segments (Figure 6h–k). The Li^+ diffusion path of c-LLZO contains the tetrahedral 24d site, and there is no evidence that Li^+ bypasses the 24d site. The re-

sults of several calculations confirm that the c-LLZO has the advantage of faster lithium-ion transport, showing high Li-ion conductivity. Understanding the mechanism that causes the significant difference in terms of Li-ion conductivity between tetrahedral phase and cubic phase is closely related to the design of SSEs with high Li-ion conductivity by providing a basis for improving the bulk and grain boundary Li^+ conductivity. Therefore, how to obtain stable cubic LLZO with high Li-ion conductivity becomes the key. In this regard, we studied the common methods and depth mechanisms to enhance the Li-ion conductivity of LLZO by improving the grain boundary ion conductivity and bulk ion conductivity.

3.2. Strategies to Enhance the Li-Ion Conductivity

LLZO has a high bulk ion conductivity, but it is challenging to directly measure the Li⁺ conductivity of LLZO powder. Alternatively, a sintered LLZO pellet is prepared to evaluate the Li-ion conductivity using ion-blocking electrode cells. To evaluate the quality of LLZO powder, the relative density of the sintered pellet is calculated, which is <100%. Because of the existing grain boundaries, the total Li-ion conductivity of LLZO is lower than that of its bulk conductivity.^[59] To narrow the gap between the actual Li-ion conductivity and the intrinsic value of LLZO powder, pressing technology and sintering additives are used to obtain dense ceramic pellets and improve the Li-ion conductivity of grain boundaries. Furthermore, it is found that the cubic phase of LLZO could be stabilized by element doping to improve the bulk Li-ion conductivity. Therefore, this section summarizes methods to improve the bulk and grain boundary Li-ion conductivity of LLZO-based SSEs.

3.2.1. Improving the Grain Boundary Conductivity

Traditional solid-state sintering is usually conducted in atmospheric conditions, which require high sintering temperature, long sintering time (>10 h), multi-step repeated and intermittent heat treatment, and grinding, leading to not only a great loss of lithium but also a reduced pellet density. As a result, the phase purity and Li-ion conductivity will be negatively affected. A positive correlation between the ion conductivity and the relative density is uncovered by Sakamoto.^[60] The hot-pressing sintering method reduces the grain boundary resistance and increases the relative density through rapid heating and high pressure (Figure 7a,b).^[61] This is further validated by Kim's group who reported a variation of Li-ion conductivity between 9.4×10^{-6} S cm⁻¹ and 3.4×10^{-4} S cm⁻¹ in the preparation of polycrystalline LLZO with a relative density in the range of 85–98%.^[62] Nb-doped Li₇La₃Zr_{2-x}O₁₂ with a relative density of 99% and RT Li-ion conductivity of 7.4×10^{-4} S cm⁻¹ was prepared by sol-gel method and hot-pressing sintering (1050 °C, 15.8 MPa).^[63]

Traditional hot-pressing sintering is processed under an external heating field and mechanical pressure, which has limitations on sintering some specific material systems.^[64] In response, researchers have developed a variety of new methods that significantly improve the sintering condition of ceramic materials, such as microwave sintering (MS) (Figure 7c),^[65] spark plasma sintering (SPS) (Figure 7d),^[51,66] flash sintering (FS) (Figure 7e),^[67] cold sintering (Figure 7f),^[68] and so on. Electromagnetic field-assisted sintering technique (FAST), represented by SPS and MS, is deemed as a main breakthrough sintering technology. Adopting FAST to prepare LLZO enables a very short sintering time (10 min) and a relatively low sintering temperature (1150 °C), both of which can effectively reduce the loss of Li. Additionally, there is only one heat treatment process in the whole sintering process, which effectively avoids the introduction of impurities and saves the overall cost. Its axial compression is very beneficial to yield the highly densified LLZO SSEs.^[69] Zhang et al.^[70] confirmed that Ta-doped LLZO with high relative density (≈99.8%)

and Li-ion conductivity (1.01×10^{-3} S cm⁻¹) can be obtained by FAST.

Although hot pressing sintering technologies can greatly reduce the gap between bulk and grain boundary conductivity and improve the reliability of theoretical ($\approx 10^{-3}$ S cm⁻¹) and experimental data ($\approx 10^{-5}$ – 10^{-3} S cm⁻¹),^[71] the pressure-aided sintering system is not as scalable as the atmospheric sintering due to the limitation of the sintering instrument, high production cost, and low output.

The incorporation of sintering additives is widely recognized for its ability to enhance the Li-ion conductivity of LLZO by mitigating the grain boundary impedance. Sintering additives are generally low melting point oxides or non-oxides (i.e., LiF, LiCl, LiBr, Al, and Si elements),^[52b,72] with oxides being the majority, including, MgO, CuO, Al₂O₃, Li₃BO₃ (LBO), LAGP, and so on.^[73] The addition of sintering additives is expected to form a low melting point solid solution, glass phase, or other liquid phase, promote particle rearrangement and viscous flow, obtain dense products, and improve the Li-ion conductivity. The introduction of additives can be divided into two main methods, one is to use excessive initial raw materials as the sintering additive, and the other is to mix LLZO powder with additives before being pressed and sintered to form dense pellets (Figure 8a). For example, adding 5 wt.% of La₂O₃ at the initial stage of material preparation regulates the distribution of Ta element in Li_{6.5}La₃Zr_{1.5}Ta_{0.5}O₁₂, which eliminates the Ta₂O₅ precipitates and achieves a high relative density of ≈98% (Figure 8b).^[74] It can be seen that the sufficient reaction of La₂O₃ with Ta₂O₅ reduces the formation of void defects at the grain boundaries (Figure 8c,d). Most of the sintering additives are added following the second method. Using Li₃PO₄ as a sintering aid, the Li_{6.5}La₃Zr_{1.5}Nb_{0.5}O₁₂ ceramic electrolyte exhibits high Li⁺ conductivity (4.3×10^{-4} S cm⁻¹ at RT).^[75] Similarly, Li₂O, as a sintering aid, melts at the sintering temperature, so that the LLZO powders freely and automatically aggregate together to obtain a dense tetragonal LLZO bulk (Figure 8e).^[76] Its relative density is determined to be 93%, and the Li-ion conductivity is 5.67×10^{-5} S cm⁻¹. Al₂O₃ is a commonly used oxide and is often implemented as a sintering additive for LLZO. The Al₂O₃ sintering additives combined with hot-pressing technology have been proven to have threefold effects on grains, grain boundaries, and voids. As a sintering additive, Al₂O₃ reacts with Li₂CO₃ to form the LiAlO₂ at grain boundaries.^[77] The Li-Al-O secondary phase at the grain boundary reduces the electronic conductivity while maintaining the Li-ion conductivity. Similar conclusions can be found in the work done by Zhang et al.^[78] that Al₂O₃ additives can greatly improve the relative density and Li-ion conductivity of Li₇La₃Zr₂O₁₂ (from 83.6% to 96%; from 4.9×10^{-5} S cm⁻¹ to 3.1×10^{-4} S cm⁻¹ at RT, respectively) (Figure 8f), thereby demonstrating its high potential for practical applications. Chen et al.^[79] coated a conformal and amorphous nano alumina layer as a sintering aid on the grain surface of Ta-doped Li₇La₃Zr₂O₁₂ by atomic layer deposition rather than a conventional physical powder mixing (Figure 8g). The Al₂O₃ layer can not only reduce the sintering temperature but also prevent lithium depletion during sintering (Figure 8h,i). The Al-doped LLZO exhibits a significantly enhanced ionic conductivity of up to ≈0.13 mS cm⁻¹. In general, the incorporation of appropriate sintering additives can effectively

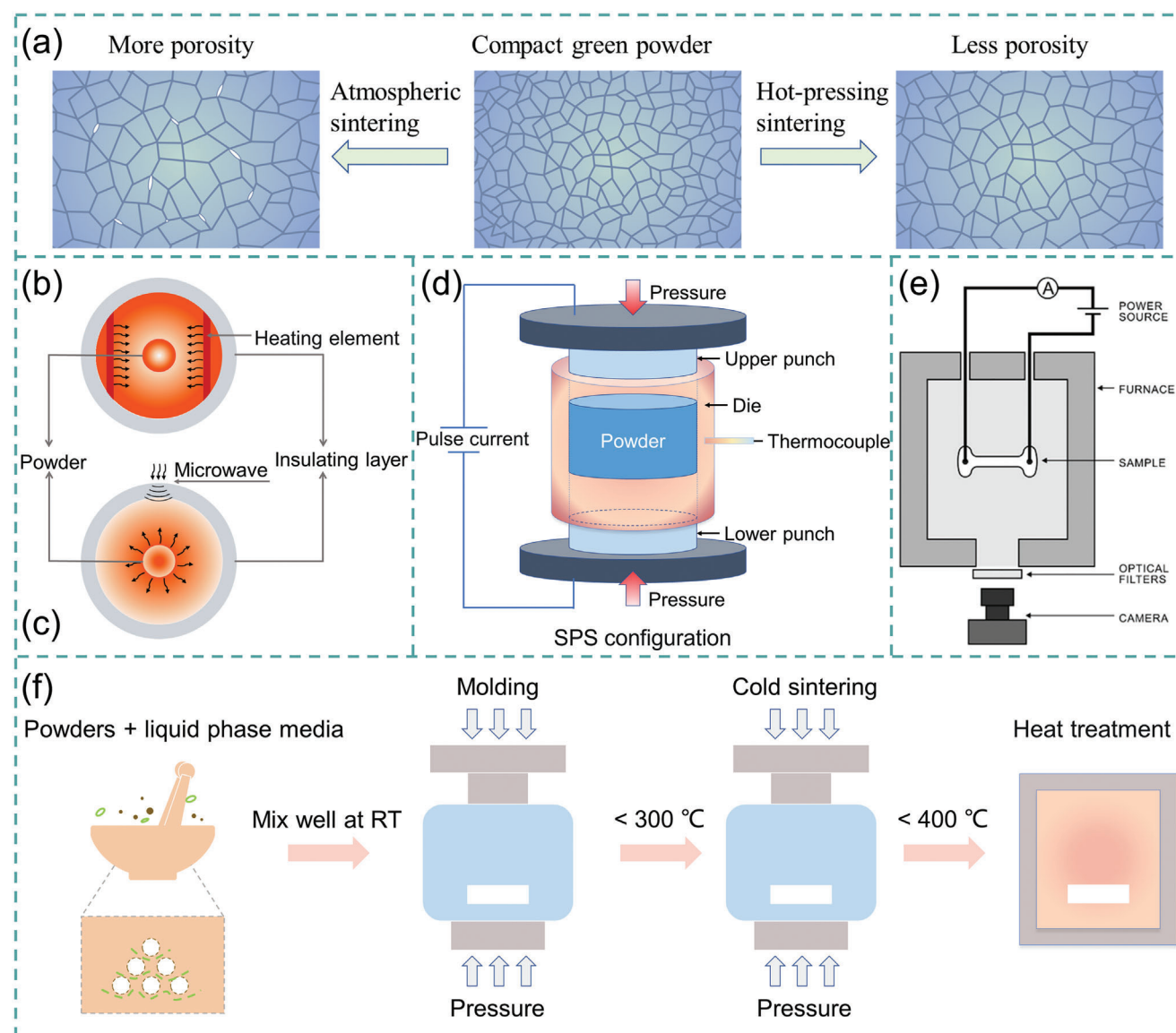


Figure 7. a) Difference in density and grain growth between atmospheric sintering and hot-pressing sintering. b) Traditional sintering. c) Microwave-assisted sintering. d) Schematic diagrams of an SPS device. e) Schematic diagrams of a FS device. Reproduced with permission.^[67] Copyrights 2019, Elsevier. f) Cold sintering process diagram.

regulate abnormal grain growth and mitigate the grain boundary impedance in LLZO, thereby enhancing its Li-ion conductivity.

3.2.2. Improving the Bulk Conductivity

Element doping is the most effective method to improve the bulk Li-ion conductivity of LLZO. The concentration of lithium ions is regulated by altering their arrangement in the crystal lattice to increase the lithium vacancy. By replacing the lithium sites with a small number of heterovalent cations, it is possible to reduce the Li site occupancy and increase the migration of lithium ions of LLZO, thereby increasing the RT bulk conductivity.^[80] Therefore, cation doping is often used to stabilize the c-LLZO at RT and thus improve the Li-ion conductivity. A variety of garnet ma-

terials, which have different physical properties but similar crystal structures, can be obtained by replacing cations with different elements. There are three doping sites in c-LLZO, namely, Li site, La site, and Zr site, respectively. The common replacement elements are Al^{3+} ,^[81] Ga^{3+} ,^[82] Mg^{2+} ,^[83] Fe^{3+} ,^[84] for the Li site; Ce^{4+} ,^[85] Ge^{4+} ,^[86] Sr^{2+} ,^[87] for the La site; and W^{6+} ,^[50,88] Gd^{3+} ,^[5w] Te^{6+} ,^[89] Ta^{5+} ,^[90] Nb^{5+} ,^[91] Ru^{4+} ,^[92] V^{5+} ,^[93] Sb^{5+} ,^[94] Bi^{5+} ,^[95] for the Zr site. Some experimental details are listed in Table 2. According to the density functional theory (DFT) calculation reported by Mira et al.^[96] and the published experimental studies, the type and position of doping elements in LLZO structure are summarized in Figure 9a. Taking Mg^{2+} substitution as an example, the DFT calculation results show that Mg occupation at the Zr site has a lower activation energy and is easier to carry out. However, experimental studies have confirmed that Mg is commonly used to

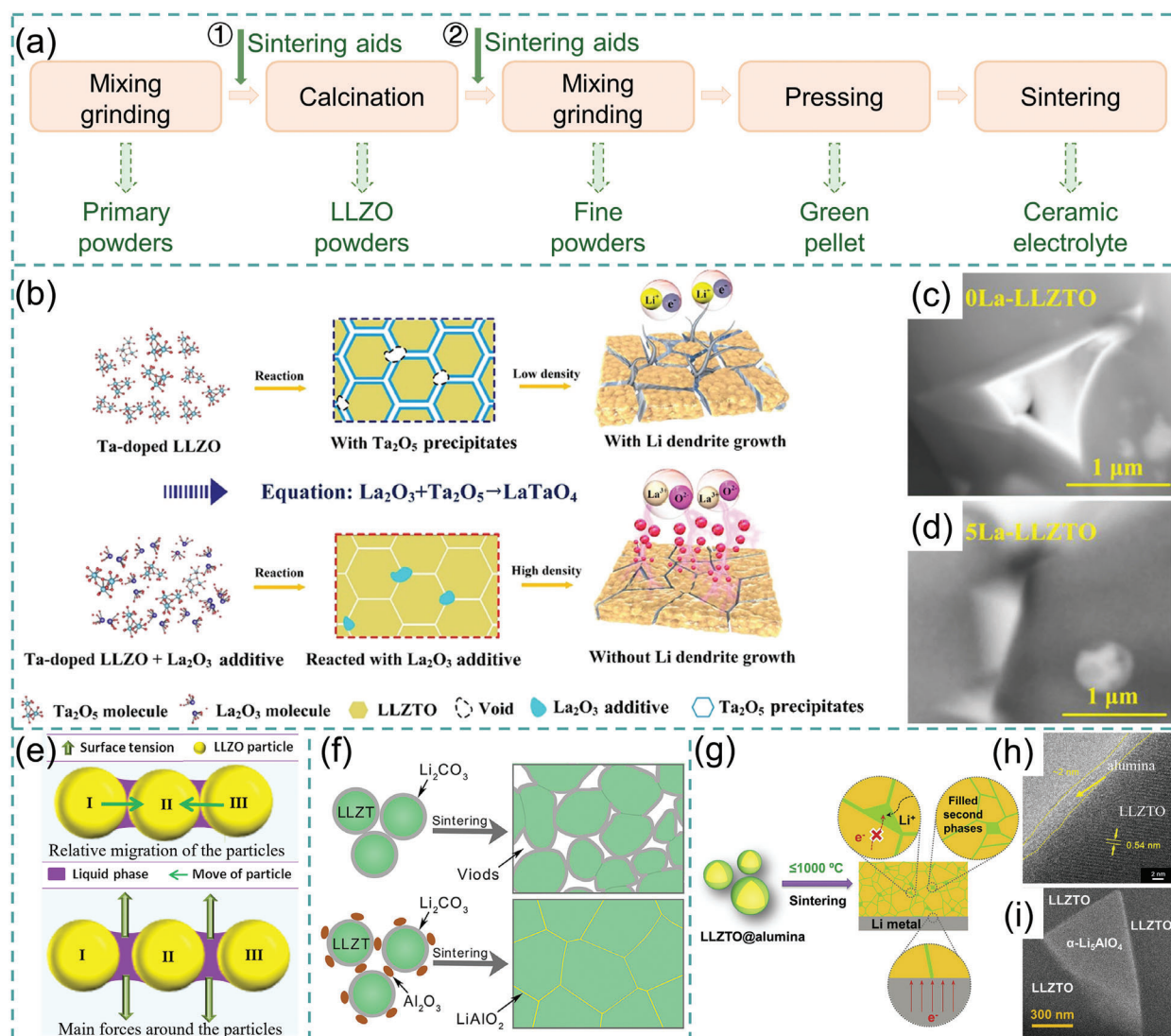


Figure 8. a) A scheme demonstrating the preparation process of sintering additive-assisted LLZO-based ceramic electrolytes; b) Schematic representation of the garnet-type electrolyte reaction mechanism; c,d) Comparative microstructure of LLZTO with and without sintering additive. Reproduced with permission.^[74] Copyright 2022, American Chemical Society. e) Consolidation mechanisms for LLZO powders auto-consolidation. Reproduced with permission.^[76] Copyright 2017, Elsevier. f) Illustration of the function of Al_2O_3 additive in the sintering process of LLZTO. Reproduced with permission.^[78] Copyright 2020, Wiley. g) Schematic diagram of conformal nanocoating with sintering aid; h) High-resolution transmission electron microscope (HRTEM) image of a particle; i) TEM image of the triangular grain boundary region. Reproduced with permission.^[79] Copyright 2021, Elsevier.

replace the Li site.^[97] Hence, it is reasonable to speculate that the actual doping site might be closely related to experimental conditions. The discrepancy between simulation and experiment results necessitates further in-depth investigations to elucidate the fundamental phenomena.

Li-Site Cation Doping. The replacement of Li sites with Al and Ga elements is widely studied. First, Geiger et al.^[98] determined that Al^{3+} in alumina crucible can replace Li^+ , and indicated that Al^{3+} substitution may be the key factor to stabilize the cubic phase. The substitution of 0.2–0.24 mol of Al^{3+} for Li^+ creates 0.4–0.48 mol of Li^+ vacancies per LLZO formula unit, which can facilitate the Li-ion transport and stabilize the cubic phase.^[99] This conclusion was also confirmed via a combination

of DFT and molecular dynamics (MD) calculations.^[100] Furthermore, Al^{3+} doping plays a key role in changing the microstructure of single LLZO grains (Figure 9b).^[101] Although it was experimentally confirmed that Al^{3+} doping could stabilize the cubic phase,^[102] the Al^{3+} source obtained from the sintered crucible could not sustain a constant doping amount. To this end, controllable Al^{3+} doping is a prerequisite for the preparation of LLZO with high Li-ion conductivity.

In addition to Al^{3+} , Ga^{3+} is another ion commonly used to replace the Li site. The bigger Li-ion radius of Ga^{3+} (0.047 nm) than that of the Al^{3+} (0.039 nm) can widen the transport channel of lithium ions and lower the energy barrier, thus showing excellent ionic transport rate. Meanwhile, the Coulombic

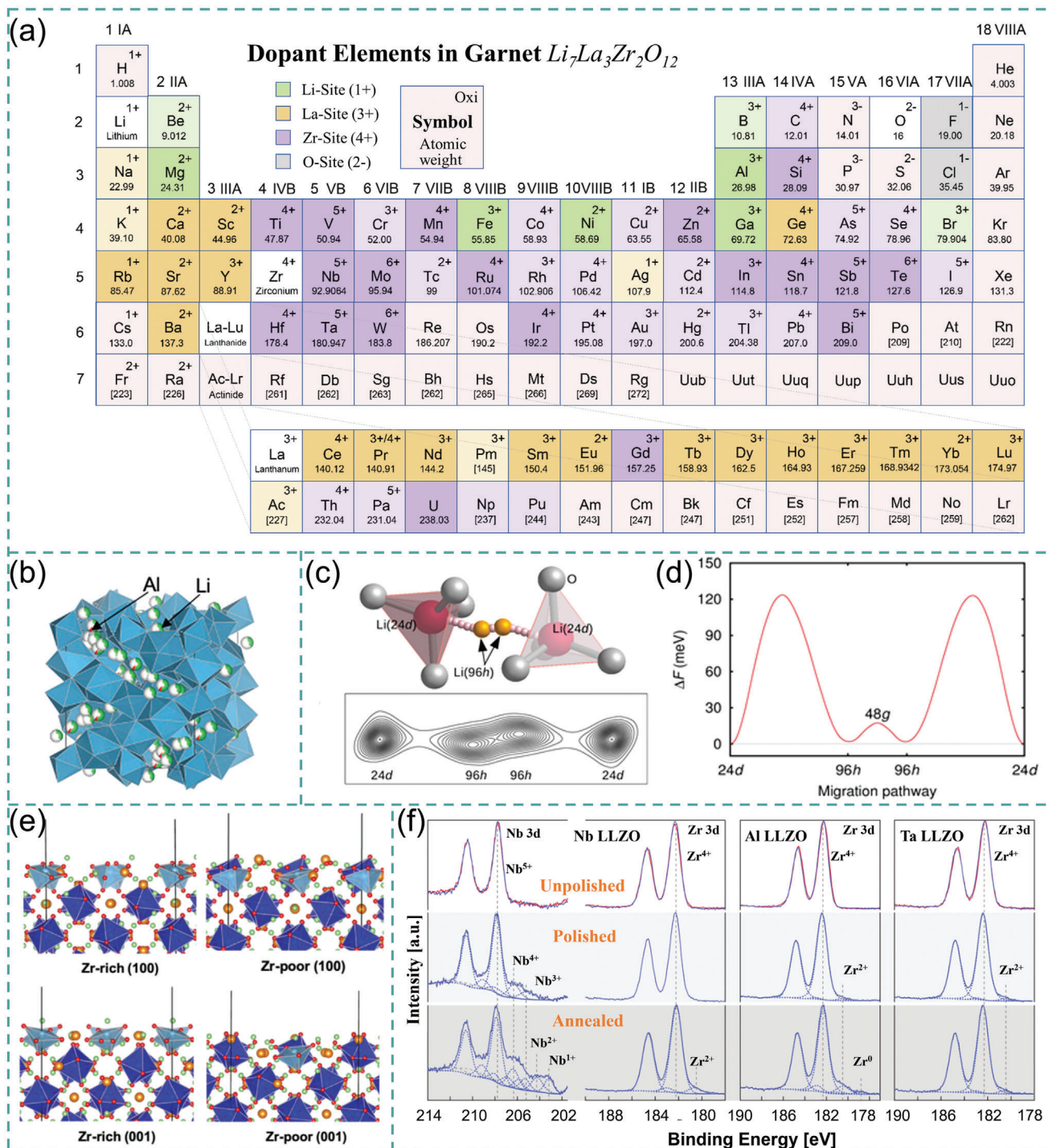


Figure 9. a) Based on DFT calculations by Miara et al.^[96] and some existing experimental studies,^[50,w,81–95,97] the types and positions of doping elements in LLZO are summarized. The colors represent possible doping sites (green: Li site, orange: La site, purple: Zr site, and gray: O site; light colors represent calculated results while dark colors represent specific experimental studies). b) Cubic crystal structure of Al-doped LLZO. Reproduced with permission.^[101] Copyright 2021, American Chemical Society. c) 3D view and contour plot of the Li atom density function; d) Free energy profile along the migration pathway. Reproduced with permission.^[118] Copyright 2018, American Physical Society. e) Energetically stable terminations for LLZO. Reproduced with permission.^[119] Copyright 2020, American Chemical Society. f) Nb 3d and Zr 3d core-level X-ray photoelectron spectroscopy (XPS) spectra from Nb-, Al-, and Ta-doped LLZO. Reproduced with permission.^[120] Copyright 2019, Wiley.

Table 2. Substitution of Li, La, Zr, O sites with heteroatoms of cubic LLZO and their properties (Li-ion conductivity, activation energy, and relative density).

Dopant	Site ^{a)}	X [mol]	Method	σ_{Li^+} [S cm ⁻¹] ^{b)}	Rd [%] ^{c)}	E_a [eV] ^{d)}	Refs.
Cation							
Ga ³⁺	Li ⁺	0.2	SSR	1.24×10^{-3}	97.3	0.311	[14]
Al ³⁺	Li ⁺	0.2	SSR	4.5×10^{-4}	94.25	0.37	[138]
Ta ⁵⁺	Zr ⁴⁺	0.6	SSR	4.19×10^{-4}	93.9	0.43	[18]
Al ³⁺	Li ⁺	0.15	NSP	4.4×10^{-6}	51	0.49	[37]
Ga ³⁺	Li ⁺	–	Co-pre.	$1.2\text{--}1.75 \times 10^{-3}$	98	0.25	[139]
Ta ⁵⁺	Zr ⁴⁺	0.25	Co-pre.	6.9×10^{-4}	92	0.2	[31a]
Ta ⁵⁺	Zr ⁴⁺	0.5	MSS	0.6×10^{-3}	96	0.37	[140]
Ru ⁴⁺	Zr ⁴⁺	0.4	SSR	2.56×10^{-4}	–	0.32	[92]
Mg ²⁺	Li ⁺	0.62	Sol-gel	5.56×10^{-5}	91.5	0.41	[97]
Mg ²⁺	Li ⁺	0.2	Sol-gel	1.1×10^{-4}	93	–	[83]
Fe ³⁺	Li ⁺	0.2	Pechini	4.28×10^{-4}	95.6	0.27	[21c]
Fe ³⁺	Li ⁺	0.2	Sol-gel	1.82×10^{-3}	96	0.25	[84b]
Sr ²⁺	La ³⁺	–	SSR	5×10^{-4}	> 90	0.31	[87]
W ⁶⁺	Zr ⁴⁺	0.35	SSR	6.6×10^{-4}	96	0.42	[5o]
Gd ³⁺	Zr ⁴⁺	0.2	SSR	2.3×10^{-4}	93-95	0.25	[5w]
Bi ⁵⁺	Zr ⁴⁺	1.0	SSR	0.1×10^{-3}	≈94	–	[95]
Ta ⁵⁺	Zr ⁴⁺	0.6	NAP	$0.24\text{--}0.67 \times 10^{-3}$	> 90	0.34–0.42	[5ae]
Al ³⁺	Li ⁺	0.25	MSS	9.13×10^{-6}	–	–	[35]
Ga ³⁺	Li ⁺	0.25	Sol-gel	8.30×10^{-4}	94.8	0.228	[141]
Ba ³⁺	La ³⁺	0.25					
Ta ⁵⁺	Zr ⁴⁺	0.375	SSR	5×10^{-4}		0.41	[91]
Al ³⁺	Li ⁺	0.25	Sol-gel	5.89×10^{-4}	94	–	[99]
Ga ³⁺	Li ⁺	0.3	Sol-gel	5.4×10^{-4}	–	0.32–0.37	[104]
Ga ³⁺	Li ⁺	0.25	SSR	1.46×10^{-3}	94.1	0.25	[103]
Ga ³⁺	Li ⁺	0.25	SSR	1.19×10^{-3}	88.50	0.32	[127]
Al ³⁺		0.25		1.8×10^{-4}	89.83	0.41	
Ce ⁴⁺	La ³⁺	0.4	SSR	1.44×10^{-5}	–	0.48	[109]
Nb ⁵⁺	Zr ⁴⁺	0.25	Sol-gel	5.69×10^{-4}	92.8	–	[116]
Nb ⁵⁺	Zr ⁴⁺	0.4	SSR	3.86×10^{-4}	96.1	0.32	[5af]
Ta ⁵⁺	Zr ⁴⁺	0.6	SSR	1.0×10^{-3}	–	0.35	[121]
Ga ³⁺ , Ba ²⁺ , Ta ⁵⁺	Li ⁺ , La ³⁺ , Zr ⁴⁺	0.05, 0.05, 0.25	SSR	7.2×10^{-4}	99.9	0.28	[132]
Anion							
F ⁻	O ²⁻	0.2	SSR	7.45×10^{-4}	> 95.4	0.288	[135]
F ⁻	O ²⁻	0.2	SSR	3.18×10^{-4}	91	0.24	[136]
F ⁻	O ²⁻	0.2	SSR	1.28×10^{-3}	–	0.28	[137]
F ⁻	O ²⁻	0.25	Calculations	11.23×10^{-3}		≈0.189	[134]
F ⁻	O ²⁻	0.5	Calculations	3.66×10^{-3}		≈0.225	
Cl ⁻	O ²⁻	0.25	Calculations	0.128×10^{-3}		≈0.328	
Cl ⁻	O ²⁻	0.5	Calculations	0.55×10^{-3}		≈0.284	

^{a)} Substitution site; ^{b)} Li-ion conductivity (room temperature); ^{c)} Relative density; ^{d)} Activation energy; ^{e)} Co-pre.

repulsion between Ga³⁺ and Li⁺ is stronger than that between lithium ions, thus lithium ions are activated leading to superior Li-ion conductivity (1.46 mS cm^{-1} at 25 °C).^[103] Shinawi and co-workers reported that only 0.3 mol of Ga³⁺ (per mole of Li₇La₃Zr₂O₁₂) is required to stabilize the cubic phase. In the meantime, the excess Ga³⁺ exists as the form of LiGaO₂ in the LLZO grain boundaries, acting as a sintering aid.^[104] Wagner et al.^[105] used single-crystal X-ray diffraction (XRD) to char-

acterize the Li_{7-3x}Ga_xLa₃Zr₂O₁₂ and confirmed that Ga-doped LLZO with $x > 0.07$ crystallizes in the acentric cubic space group I-43d. ⁷Li nuclear magnetic resonance (NMR) spectrum confirmed that space group I-43d (compared with Ia-3d) has an additional lithium-ion diffusion process. Meanwhile, Huang and co-workers investigated the SSR process of Ga-doped LLZO by in situ TEM at an atomic scale.^[106] It was revealed that Ga doping not only plays a role in stabilizing the cubic LLZO structure

but also skips the tetragonal mesophase and directly transforms it into the cubic phase. Both experimental results and theoretical calculations corroborate the advantages of LLZO doping with Ga³⁺. Compared with Al-doped LLZO, the RT Li-ion conductivity of Ga-doped LLZO is often >10⁻³ S cm⁻¹, and can approach up to 2 × 10⁻³ S cm⁻¹, while the RT Li-ion conductivity of Al-doped LLZO barely reaches 5 × 10⁻⁴ S cm⁻¹.^[107] However, from the perspective of practical application, the raw material precursor of Al₂O₃ is cheaper than Ga₂O₃. To promote the development of LLZO, it is necessary to control the composition and reduce the cost.

La-Site Cation Doping: The La site is usually replaced with alkaline earth metal elements (such as Ce and Sr). Previous works have confirmed that alkaline earth metal doping can increase the Li1 site in LLZO while reducing the Li2 site, and thus effectively increasing the Li-ion conductivity.^[5s,108] Rangasamy et al.^[109] revealed that Ce⁴⁺ can stabilize the cubic phase to improve the conductivity of lithium ions, but the limited solubility of Ce leads to the precipitation of CeO₂ causing increased interfacial impedance. Therefore, it is found that Ce doping is less effective than Al, Ga, Nb, or Ta substitution. Valle and co-workers^[110] investigated the effect of La deficiency on crystal structure and electrochemical properties of Li_{6.5}La_{2+x}Zr_{1.5}Ta_{0.5}O₁₂ by controlling the La content (x spanning from 0 to 1.2). The results show that the highest Li-ion conductivity and critical current density (CCD) are achieved when x is fixed at 1.0. This is also in line with previous work.^[111] However, since La sites not only have considerable influence on the overall structure of LLZO but also determine the Li-ion transport channels, thus La sites are rarely selected for doping modification of LLZO.^[112]

Zr-Site Cation Doping: Nb and Ta are two common doping elements to replace the Zr site.^[113] Nb-doped LLZO (LLZNO) exhibits higher Li-ion conductivity (vs Al-doped LLZO) and lower cost (vs Ga-doped LLZO) thus attracting increased attention.^[114] Ohta's group^[115] reported that LLZNO can stabilize the cubic phase by introducing Li vacancies to interfere with Li sites in the tetragonal phase. Its Li-ion conductivity can reach 8 × 10⁻⁴ S cm⁻¹ at 25 °C. Ishiguro et al.^[116] synthesized the LLZNO with a relative density of 92.8% and a Li-ion conductivity of 5.69 × 10⁻⁴ S cm⁻¹. Ni et al.^[5af] studied the effect of process conditions and doping amount on the crystalline structure, microstructure, and Li-ion conductivity of LLZNO. It is confirmed that the relative density and Li-ion conductivity of LLZNO ceramics are affected by different element doping ratios and preparation processes. The experimental data^[117] align with the results obtained from advanced MD simulations using a machine learning forcefield that achieves ab initio accuracy (Figure 9c,d).^[118] Due to the doping of Nb, the free energy difference between the 24d and 96h sites is negligible, which contributes to the high Li-ion conductivity of LLZNO.

Replacing Zr⁴⁺ in LLZO with Ta⁵⁺ not only stabilizes the cubic phase but also increases the Li-ion conductivity by introducing more Li vacancies through hypervalent cations.^[15i] Li and co-workers^[121] prepared the Li_{6.4}La₃Zr_{1.4}Ta_{0.6}O₁₂ (LLZTO) solid-state electrolyte with a high Li-ion conductivity of 1.0 × 10⁻³ S cm⁻¹ at RT. It is consistent with the results obtained by Adams et al.^[122] MD simulation, bond valence studies, and experimental characterizations disclosed that the enhanced Li-ion conductivity is ascribed to the increased vacancy concentration through reduc-

ing local Li ordering. Gao et al.^[119] demonstrated better chemical stability of Ta and Al dopants using first-principles calculations (Figure 9e). Zhu et al.^[120] investigated the surface chemistry of LLZO (with different doping elements) in contact with Li using X-ray photoelectron spectroscopy (XPS), electrochemical impedance spectroscopy (EIS), and DFT calculations (Figure 9f). The results show that Ta doping has higher chemical stability than the other two elements (Al, Nb), furthermore, its bulk and interface are almost isoenergetic. Inada's group demonstrated that Ta-doped LLZO with high Li-ion conductivity can be recycled, indicating that the Ta-doped LLZO is viable for practical application.^[123]

Zr-Site High-entropy Doping: The cubic phase structure can be stabilized through the substitution of Al/Ga dopants at the Li site, or Ce/Sr dopants at the La site, or Nb/Ta dopants at the Zr site. However, the formation of these vacancies can influence the lithium chemical potential of LLZO and compromise the reduction stability against the lithium metal. Therefore, Jung et al.^[124] developed an entropy-driven solid-state reaction for producing stable cubic garnet SSEs with high lithium content and without vacancy formation (i.e., Li₇La₃Zr_{0.5}Hf_{0.5}Sc_{0.5}Nb_{0.5}O₁₂ and Li₇La₃Zr_{0.4}Hf_{0.4}Sn_{0.4}Sc_{0.4}Ta_{0.4}O₁₂). The nucleation temperature of this high-entropy electrolyte was reduced from 750 to 400 °C. Experimental results confirm that the stability against lithium metal in Li₇La₃Zr_{0.4}Hf_{0.4}Sn_{0.4}Sc_{0.4}Ta_{0.4}O₁₂ without Li vacancy is superior to that of the Li_{6.6}La₃Zr_{0.4}Hf_{0.4}Sn_{0.2}Sc_{0.2}Ta_{0.6}O₁₂. Moreover, Han et al.^[125] successfully synthesized a highly stable high-entropy garnet SSE (Li_{6.2}La₃Zr_{0.4}Hf_{0.4}Ti_{0.4}Nb_{0.4}Ta_{0.4}O₁₂) with exceptional air stability. This research found that there is a trade-off between Li-ion conductivity and air stability in LLZO doped with single elements. Therefore, it is imperative to enhance the Li-ion conductivity and air stability of LLZO through multi-element doping, harnessing the synergistic effects of diverse elements. Through technical optimization, Feng et al.^[126] utilized ultra-fast high-temperature sintering technology to achieve the rapid synthesis of high-entropy garnet Li_{7+a-c-2d}La₃(A³⁺_aB⁴⁺_bC⁵⁺_cD⁶⁺_d)O₁₂ (A = Sc, Y, Bi; B = Zr, Mo, Sn, Te, Hf; C = Nb, Sb, Ta; D = W in merely tens of seconds (Figure 10a). Furthermore, the entropy-stabilization effect was discovered via high-throughput screening of the garnet family, wherein the increase in configurational entropy has been proved to be advantageous for synthesizing cubic-phase garnets (Figure 10b). Among the series of synthesized garnet electrolytes, Li_{6.6}La₃Zr_{0.4}Sn_{0.4}Sc_{0.4}Ta_{0.4}Nb_{0.4}O₁₂ exhibits the highest Li-ion conductivity (3.57 × 10⁻⁴ S cm⁻¹) and a low level of electronic conductivity (5.26 × 10⁻⁹ S cm⁻¹). In summary, the proposal of high-entropy LLZO is expected to simultaneously achieve breakthroughs in both high Li-ion conductivity and high air stability, thus having the potential to become a priority for future research endeavors of LLZO.

Multi-Site Cation Doping: With the progress of doping modification at different occupation sites, multiple cations doping has been further attempted, aiming to exploit the synergy of different sites to perfect the garnet SSE. For example, Chen et al.^[127] studied the microstructure and electrochemical performance of LLZO by adjusting different Al/Ga doping ratios (Al + Ga = 0.25 mol). The results show that the Li-ion conductivity reaches a maximum value of 1.19 × 10⁻³ S cm⁻¹ with a Ga content of 0.25 mol. It also proves that the Li-ion conductivity of Ga³⁺ doped LLZO is higher than that of the Al³⁺ doped in LLZO (Figure 10c). From

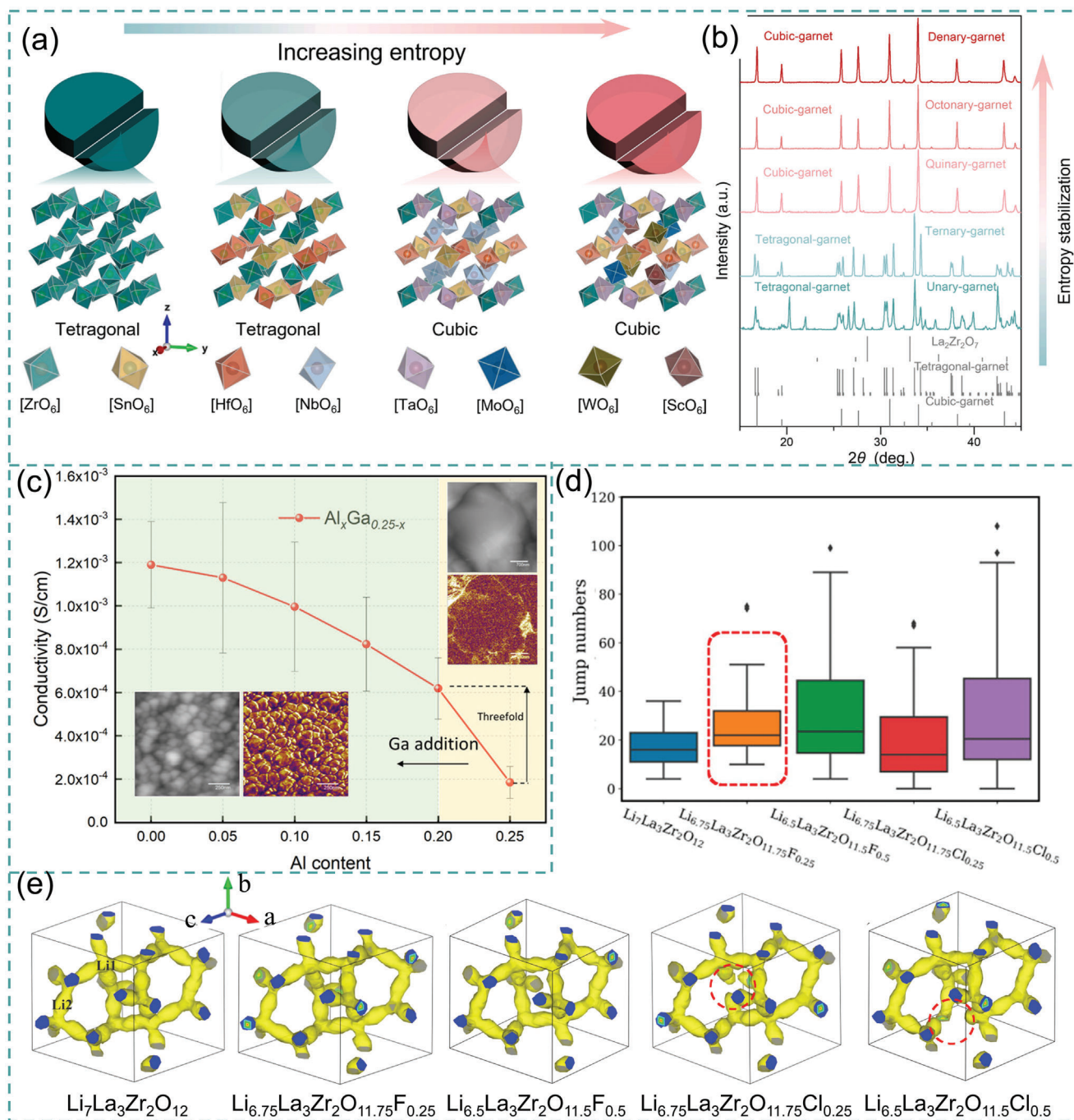


Figure 10. a) Schematic illustration of pellets and lattice structure of garnets; b) XRD patterns of representative unary-garnet, ternary-garnet, quinary-garnet, octonary-garnet, and denary-garnet. Reproduced with permission.^[126] Copyright 2023, Elsevier. c) Diagram of Li-ion conductivity as a function of Al and Ga contents. Reproduced with permission.^[127] Copyright 2020, American Chemical Society. d) Boxplot of jump numbers between Li1–Li2 sites for samples; e) Isosurfaces (yellow) of Li-ion probability density distribution for samples. Reproduced with permission.^[134] Copyright 2022, American Chemical Society.

the current reports, co-doping of Li and Zr sites seems to be favorable, which utilizes the partial substitution of Li sites to stabilize the cubic phase and the partial substitution of Zr sites to increase the number of carriers. The Li-ion conductivity is improved by charge compensation.^[128] For example, the introduction of Ga^{3+}

and Sr^{3+} at the Li and Zr sites enhances the Li-ion conductivity from $1.1 \times 10^{-3} \text{ S cm}^{-1}$ to an optimal value of $1.8 \times 10^{-3} \text{ S cm}^{-1}$ (at 300 K).^[129] Compared with the co-doping of Li and Zr sites, the Li-ion conductivity of La-Zr sites co-doped LLZO is relatively low,^[130] which is presumably due to the negative impact on the

lattice structure of LLZO and blockage of the Li⁺ transport channels after La site doping. Still, the overall Li-ion conductivity can meet the requirements for SSEs ($\sim 10^{-4}$ S cm⁻¹).^[131]

Some studies partially dope Li, La, and Zr sites simultaneously. For example, Meesala and co-workers^[132] confirmed that the tri-doped Li_{6.65}Ga_{0.05}La_{2.95}Ba_{0.05}Zr_{1.75}Ta_{0.25}O₁₂ has the highest Li-ion conductivity (0.72 and 1.24 mS cm⁻¹ at RT and 60 °C, respectively). The increase in total conductivity with an increase of multi-ion doping in the garnet framework can be well explained by the dense microstructure, decreased 96h_{Li2}/24d_{Li1} ratio, and reduced oxygen occupancy. This is consistent with previous studies that Li2 sites should be relatively few in ideal garnet structures to ensure high Li-ion conductivity. As for the tri-doping, only a few works have been reported so far and the corresponding Li-ion conductivity is not higher than the co-doped LLZO materials. Moreover, the doping sites and the synergistic effect between dopants should be thoroughly uncovered.

O-Site Anion Doping: In recent years, anion doping and substitution have gained elevated research momentum due to the critical influence of anion sublattices on the Li-ion conductivity of solid lithium-ion conductors.^[133] According to Yang et al.,^[134] based on ab initio molecular dynamics simulations, the F doping system has a larger median jump number and enhanced Li ion mobility compared with c-LLZO and Cl-doped LLZO (Figure 10d). This is because Cl-doped LLZO has large local structural distortion and uneven diffusion network (Figure 10e). In contrast, the diffusion network of the F-doped system is more uniform, thus showing higher Li-ion conductivity. It is proven that F element doping is more suitable for the system than Cl element doping. Interestingly, the anion and cation co-doping has also achieved excellent results. For example, Ma et al.^[135] prepared the Li_{6.8}Al_{0.2}La₃Zr₂O_{11.8}F_{0.2} solid-state electrolyte with a Li-ion conductivity of 7.45×10^{-4} S cm⁻¹ at 30 °C, a relative density and an activation energy of 95.4% and 0.288 eV. Li_{6.2}Al_{0.2}La₃Zr₂O_{11.8}F_{0.2} synthesized by Sodhiya and co-workers obtains a relative density of 91% and an activation energy of only 0.24 eV.^[136] These results suggest that due to the high electronegativity of the anion sublattice, the fluoride anion induces a more rigid structure with a smaller thermal displacement of the anion sublattice, thus resulting in less resistance against lithium-ion diffusion. Therefore, the Li-ion conductivity is improved and the activation energy is lowered.^[137] Albeit the higher activation energy of Cl ion replacing Li, La, or Zr sites (2–7 eV, calculated by Miara et al.^[96]), Cl has been proven to replace O sites. It can be inferred that elements such as F, S, N, and P may more easily replace O sites, which needs further confirmation.

In summary, this study examines common approaches to enhance the grain boundaries/bulk Li-ion conductivity of LLZO. To improve the Li-ion conductivity of grain boundary, it is necessary to combine the hot-pressing and sintering methods. However, balancing equipment and time costs becomes a challenge. Meanwhile, the commonly used “trial and error” method is also not helpful to quickly selecting high-performance materials. Therefore, finding a way to produce LLZO in high quality, low cost, and high volume is critical. The element doping is a commonly utilized method to improve the bulk conductivity of LLZO. However, single-element doping has been proven to improve the conductivity of lithium ions while weakening its air stability, on the contrary, the single-element doping LLZO with good air stability

has poor ionic conductivity. Fortunately, the novel high-entropy LLZO has demonstrated its potential for achieving comprehensive performance enhancement through the synergistic interplay of multiple constituent elements. However, the ionic conductivity of the current high-entropy LLZO only achieves $\approx 10^{-4}$ S cm⁻¹. To satisfy the requirements of solid-state lithium metal batteries with high energy and power densities, further investigation into high-entropy LLZO is important.

3.3. Investigation of the Mechanism for Improved Ionic Conductivity

The SSEs used in SSBs are usually polycrystalline materials. In addition to the overall ion transport, ion diffusion at grain boundaries has a significant impact on the overall ion conduction and battery performance.^[142] Zhu et al.^[143] found the diffusivity shows a sharp decrease near the grain boundaries. The affected region is localized, in a ≈ 2 nm-thick area across the grain boundary plane. For regions that are beyond 1 nm away from the grain boundary plane, the ionic diffusion appears to be unaffected. The calculated grain boundary ionic conductivity at 300 K (extrapolated from the Arrhenius relationship) is only 0.03 mS cm⁻¹, which is nearly two orders of magnitude lower than that of the bulk conductivity. Gao et al.^[144] calculated the overall diffusion coefficients of the $\sigma 3(112)$ GB and $\sigma 1(110)$ GB models and compared them with those of the bulk LLZO (Figure 11a). It is found that the diffusion coefficient of the $\sigma 3(112)$ GB model is significantly close to the bulk diffusion coefficient, while the $\sigma 1(110)$ GB model exhibits obvious slow diffusion at low temperature. The energetically favorable models reveal that ZrO₆ octahedra are distorted to dissociate ZrO₅ units and isolate O ions at GBs. In contrast, ZrO₅ shows a tendency to trap excess electrons, leading to dendrite growth along poorly contacted grain boundaries (Figure 11b). These effects can be partially minimized by altering the synthesis conditions to increase the density of LLZO (i.e., reducing porosity), increase the grain size (i.e., minimize the volume fraction of GBs), and/or improve contact at the GBs. In this regard, hot pressing or adding sintering additives have been revealed as effective strategies.^[145]

Theoretical calculations have been widely used to study the impact of Li⁺ transport paths, phase transitions, and element doping on bulk ionic conductivity.^[146] Experimental studies have shown that irrespective of the specific dopant or doping site, exceeding the critical vacancy concentration can disrupt the Li order, thereby increasing the ionic conductivity. Miara et al.^[147] investigated the effect of Rb and Ta doping on the ionic conductivity and stability of the garnet (Li_{7+2x-y}(La_{3-x}Rb_x)(Zr_{2-y}Ta_y)O₁₂ ($0 \leq x \leq 0.375$, $0 \leq y \leq 1$)) superionic conductor using first principle calculations. According to the topological analysis, it is found that the migration path is in close agreement with the lithium trajectories along the path, which is consistent with the calculation results of Xu's group.^[56] The results show that doping does not significantly change the topology of the migration path, but mainly changes the lithium concentration, which improves the Li-ion conductivity of LLZO by disrupting the Li order.

F anion doping is a new method to improve the Li-ion conductivity of LLZO. Fluorine is more electronegative than oxygen and therefore binds more strongly to Li ions. Unfortunately, thus far

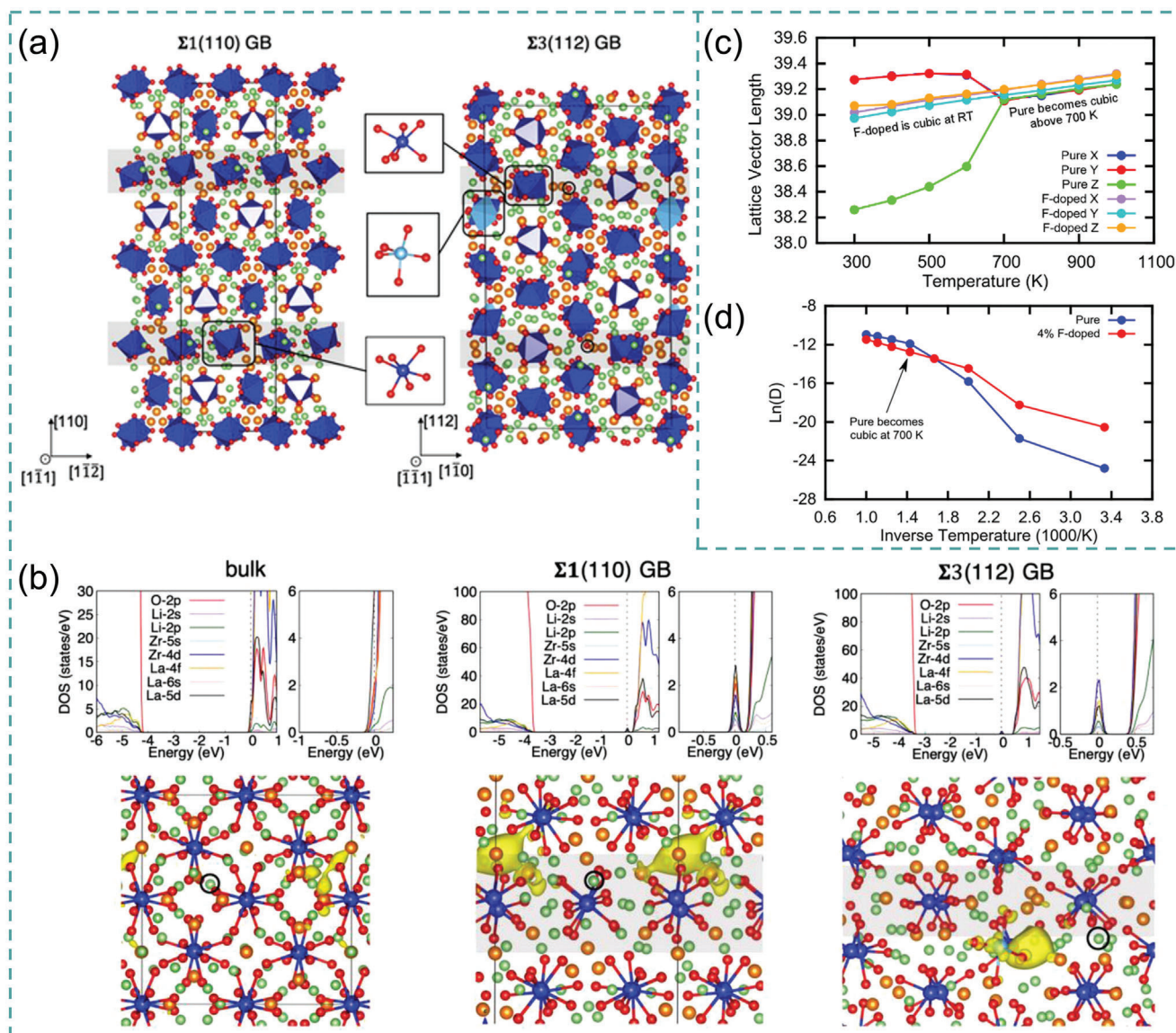


Figure 11. a) Energetically favorable structures of GB models of LLZO; b) Calculated partial densities of states (upper panel) and partial charge densities associated with the states in the energy range from -0.1 to 0.1 eV (lower panel). Reproduced with permission.^[144] Copyright 2021, Wiley. c) Time-averaged lattice parameters of pure and F-doped LLZO as a function of temperature; d) Arrhenius plot of lithium diffusion in pure and F-doped LLZO. Reproduced with permission.^[148] Copyright 2018, American Chemical Society.

little is known about the migration paths and dispersal mechanisms that may occur. Yeandel and co-workers adopted DFT to investigate the effect of F-doping on the relative stability, transport properties, and Li-ion kinetics of LLZO. Low incorporation energies have been calculated, suggesting fluoride anions are stable on the oxygen sites with a compensating lithium-ion vacancy defect (Figure 11c).^[148] Molecular dynamics proved that F is beneficial to stabilize the c-LLZO at low temperatures (Figure 11d).

In summary, a conclusion can be drawn based on simulation results reported thus far: the element doping promotes lithium-ion transport by increasing Li vacancies. Meanwhile, the presence of Li vacancies accompanying heteroatom doping hinders the ordered arrangement of Li in the tetragonal phase, thereby contributing to an enhanced stabilization of the cubic phase.

4. Applications in Lithium Batteries

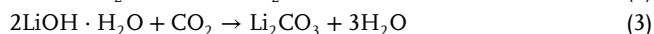
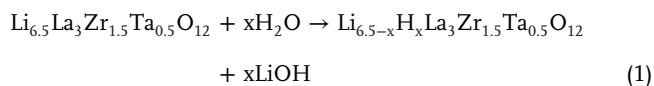
The electrochemical performance of all-solid-state lithium batteries is dependent on the properties of solid-state electrolyte materials, such as Li-ion conductivity, electrochemical stability window, and physicochemical properties (mechanical strength, thermal stability, etc.).^[149] To prevent lithium dendrites from penetrating through the electrolyte and directly contacting the cathode, the hardness of the SSE is required to be rather high. Monroe and Newman used linear elasticity theory to show that the shear modulus of lithium-ion conductor SSEs must be greater than twice that of lithium metal to prevent the growth of dendrites.^[150] The shear modulus of LLZO is calculated to be ≈ 60 GPa, which is much larger than that of lithium metal (4.9 GPa).^[151] As a fast

Li-ion conductor, LLZO is almost insulating to electrons (10^{-8} S cm^{-1}). Thus, it is assumed that garnet LLZO can effectively inhibit the growth of lithium dendrites, indicating that the LLZO can be a substitute for separator and liquid electrolyte for next-generation lithium metal batteries. However, solid-state lithium metal batteries comprising LLZO-based solid-state electrolytes still face many problems in practical applications, such as interface incompatibility and volume expansion during cycling, so it is important to rationally design the positive electrode and electrolyte. Therefore, this section summarizes two major applications of LLZO-based SSEs in SSBs: 1) As a component to construct a composite positive electrode, providing a lithium-ion transportation path within the positive electrode, and improving the interface compatibility between electrode and electrolyte; 2) As a solid-state electrolyte, it blocks the contact between positive and negative electrodes and provides conditions for Li-ion conduction. The serious challenges encountered in the practical application of LLZO, including the formation and removal of the Li_2CO_3 impurity phase, are comprehensively analyzed before the analysis and summary of the aforementioned two applications.

4.1. Impurity Phase of $\text{Li}_2\text{CO}_3/\text{LiOH}$

4.1.1. Formation of $\text{Li}_2\text{CO}_3/\text{LiOH}$

LLZO is known to be unstable in air and will generate a Li_2CO_3 impurity phase, and its presence will cause side reactions leading to battery degradation. Therefore, it is necessary to conduct a detailed analysis of the formation and elimination of Li_2CO_3 impurities.^[152] The formation of Li_2CO_3 can be classified as follows: 1) Garnet reacts directly with dry CO_2 to generate Li_2CO_3 ^[153]; 2) The water in the air reacts with the surface of LLZO through Li^+/H^+ ion exchange to generate LiOH , which then reacts with CO_2 to form Li_2CO_3 ; 3) The spontaneous ion-exchange of Li^+/H^+ in the aqueous solution of garnet subsequently forms Li_2CO_3 (Figure 12a).^[154] The reaction kinetics of the first approach are slow, and the generated Li_2CO_3 can be ignored.^[155] The prerequisite for the occurrence of the third scenario is sufficient H_2O . The second approach seems to be more widely applicable, taking the $\text{Li}_{6.5}\text{La}_3\text{Zr}_{1.5}\text{Ta}_{0.5}\text{O}_{12}$ as an example, the reaction equations are as follows (Equations (1)–(3)):



4.1.2. Remove of $\text{Li}_2\text{CO}_3/\text{LiOH}$

These reactions result in the inability of LLZO to build a good lithium-ion transport channel with active material.^[156] Therefore, a great deal of research work has been carried out to solve the issue of Li_2CO_3 on the LLZO surface. The conventional methods include mechanical polishing and high-temperature treatment.^[157] However, mechanical polishing cannot completely

remove Li_2CO_3 and may induce additional contamination. High-temperature annealing of LLZO for a long period may cause lithium depletion, thus reducing the Li-ion conductivity. Later on, acid etching and plasma reduction methods emerged.^[158] For example, Li_2CO_3 on the surface of $\text{Li}_{6.4}\text{La}_3\text{Zr}_{1.4}\text{Ta}_{0.6}\text{O}_{12}$ pellet can be completely removed in only 30 s after 1M hydrochloric acid solution treatment (Figure 12b,c).^[159] Ruan et al.^[160] dropped 10 μL of hydrochloric acid, deionized water, and LiF onto the LC-LLZO (Ta-doped LLZO with LiOH and Li_2CO_3 surface passivation layers) pellet to synthesize CF-LLZO (CF is LiF-LiCl) (Figure 12d). The 3D cross-linked structure of LiF and LiCl on the pellet surface can promote the wetting of the Li/LLZO interface and greatly reduce the interface impedance ($11.6 \Omega \text{ cm}^2$), so the lithium metal battery exhibits good cycle and rate performance. It has also been confirmed that the plasma method could completely remove surface Li_2CO_3 impurities, while high-temperature treatment could only partially remove Li_2CO_3 impurities (Figure 12e).^[161] Meanwhile, these methods may trigger degeneration of the LLZO structure, which will cause cost problems. More importantly, Li_2CO_3 is only temporarily removed, causing the rapidly regenerated Li_2CO_3 when exposing the treated electrolytes to air again.

4.1.3. Transformation of $\text{Li}_2\text{CO}_3/\text{LiOH}$

A “conversion” response is gradually revealed to be effective. The term “conversion” means the reaction of Li_2CO_3 with other reactants to produce favorable products that inhibit any further reactions in air and meanwhile benefit the electrode/electrolyte interfacial contact. Yang et al.^[162] prepared the LLZTO@ LiCoO_2 (LCO) utilizing the reaction between Li_2CO_3 and Co_3O_4 to form cathode LCO active material on $\text{Li}_{6.4}\text{La}_3\text{Zr}_{1.4}\text{Ta}_{0.6}\text{O}_{12}$ surface. The protective layer formed ensures direct electrode/electrolyte contact. Therefore, the batteries demonstrate superior electrochemical performance over those with Li_2CO_3 . Han and co-workers mixed the Li_3BO_3 , $\text{LCO@Li}_2\text{CO}_3$, and $\text{LLZO@Li}_2\text{CO}_3$ to make a cathode slurry, which was coated on the surface of a $\text{LLZO@Li}_2\text{CO}_3$ pellet, and then co-sintered at 700 °C (Figure 12f). The reaction generates a solid solution of $\text{Li}_3\text{BO}_3\text{-Li}_2\text{CO}_3$, which solves the problem of limited physical contact between bare LCO particles and LLZO by infiltrating the cathode/SSE interface. Furthermore, the introduction of a small amount of LLZO into the cathode is beneficial to ameliorate the battery cycle stability (Figure 12g).^[155]

For solid-state electrolytes, the method of in situ construction of an interfacial wetting layer with Li_2CO_3 has received increased attention. For example, an air-stable and lithiophilic Li_xSiO_y (LSO) layer was in situ constructed on the garnet surface by a double substitution reaction between Li_2CO_3 and SiO_2 (Figure 13a,b). The LSO-modified symmetric cell has a low interfacial impedance of $3 \Omega \text{ cm}^2$ and a high critical current density of 1.2 mA cm^{-2} at 30 °C.^[163] Bi et al.^[164] used molten $\text{NH}_4\text{H}_2\text{PO}_4$ salt to drive the conversion reaction that simultaneously consumed the Li_2CO_3 pollutants and formed the Li_3PO_4 layer on the surface of garnet. Li_3PO_4 is further transformed into $\text{Li}_3\text{P/Li}_2\text{O}$ lithiophilic interlayer by contacting with lithium metal, achieving seamless lithium/garnet interfacial contact and thus reducing the interface resistance to $13 \Omega \text{ cm}^2$ (Figure 13c). This

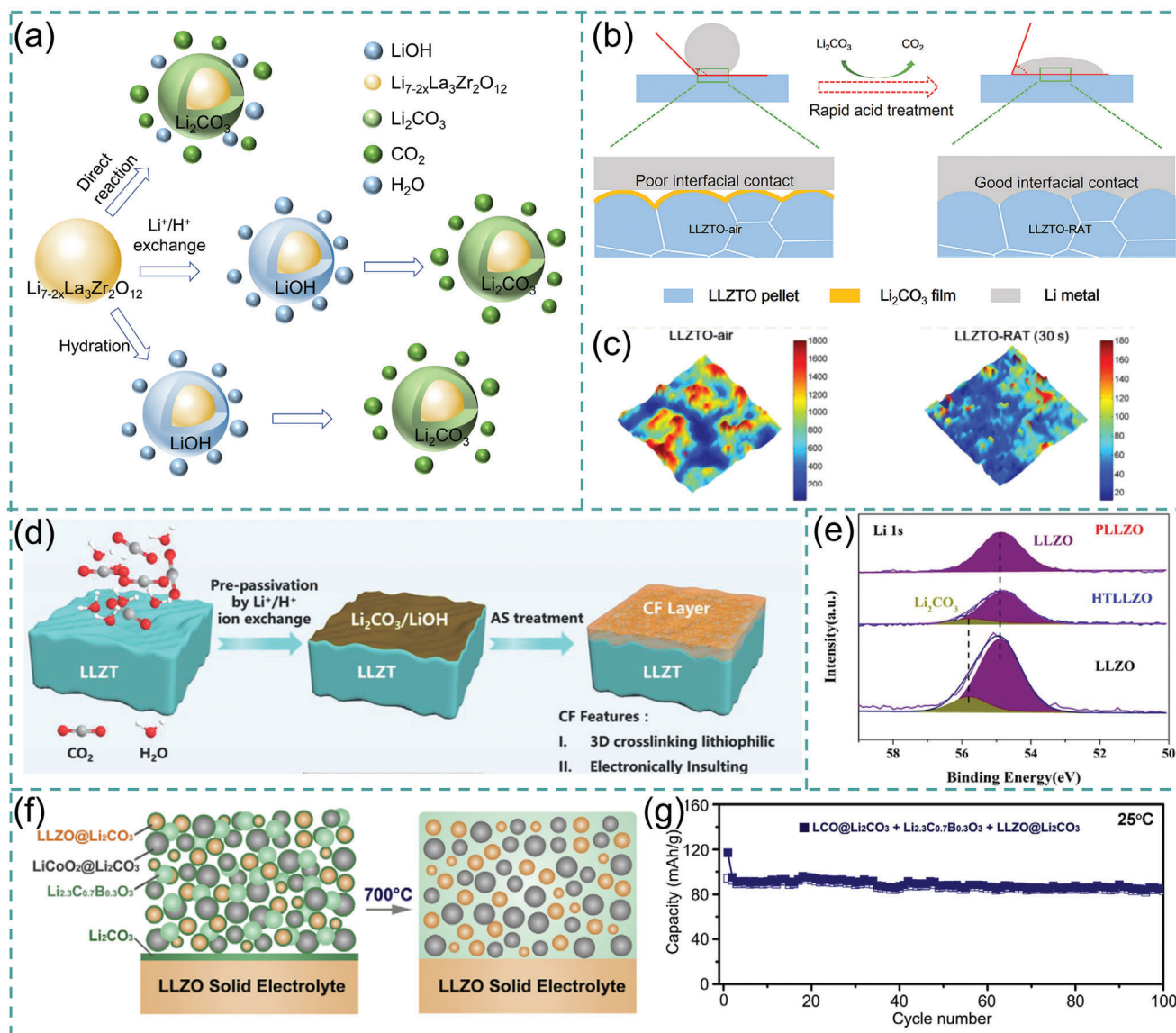


Figure 12. a) Reaction pathways of garnet electrolytes with air; b) Schematic diagram of acid treatment of Li_2CO_3 impurities to improve interfacial contact; c) Raman mappings of the pellet before and after acid treatment. Reproduced with permission.^[159] Copyright 2019, Elsevier. d) Schematic of the construction process of CF-LLZO. Reproduced with permission.^[160] Copyright 2020, Wiley. e) High-resolution Li 1s XPS spectra of different nanoparticles. Reproduced with permission.^[161] Copyright 2021, Elsevier. f) Schematics of the interphase-engineered; g) Cycling performance of the battery. Reproduced with permission.^[155] Copyright 2018, Elsevier.

result is consistent with the DFT calculation that $\text{Li}_2\text{CO}_3/\text{Li}$ has a higher interfacial energy ($0.3558 \sigma \text{ J}^{-1} \text{ m}^{-2}$ vs $0.081 \sigma \text{ J}^{-1} \text{ m}^{-2}$) and a lower work of adhesion ($0.183 \text{ Wad J}^{-1} \text{ m}^{-2}$ vs $2.452 \text{ Wad J}^{-1} \text{ m}^{-2}$) than $\text{Li}_3\text{PO}_4/\text{Li}$ (Figure 13d). Duan et al.,^[165] converted the pollutant ($\text{Li}_2\text{CO}_3/\text{LiOH}$) to a fluorinated interface using NH_4F at a moderate temperature of 180 °C (Figure 13e). The modified interface has a higher electron shuttle energy barrier and lower surface diffusion energy barrier, promoting the uniform Li^+ flux distribution and effectively inhibiting the generation of dendrites. The wettability of LLZO and molten lithium is enhanced by the construction of a lithium salt layer with nanopore structure on the surface of garnet using H_3BO_3 aqueous solution and HF vapor. As a result, the SSBs with LiFePO_4 (LFP) or

$\text{LiNi}_{0.5}\text{Co}_{0.2}\text{Mn}_{0.3}\text{O}_2$ (NCM523) positive electrodes show excellent long-term cycling performance (Figure 13f,g).^[166]

4.1.4. Advanced Characterizations of $\text{Li}_2\text{CO}_3/\text{LiOH}$

The presence of Li_2CO_3 disrupts the lattice structure of LLZO, resulting in the formation of a heterogeneous surface layer with significantly reduced Li-ion conductivity. Due to the poor wettability of Li_2CO_3 toward the lithium metal, LLZO shows large interface resistance, uneven current distribution, and lithium deposition when in contact with lithium metal, resulting in a lower apparent critical current density. However, due to the lack of

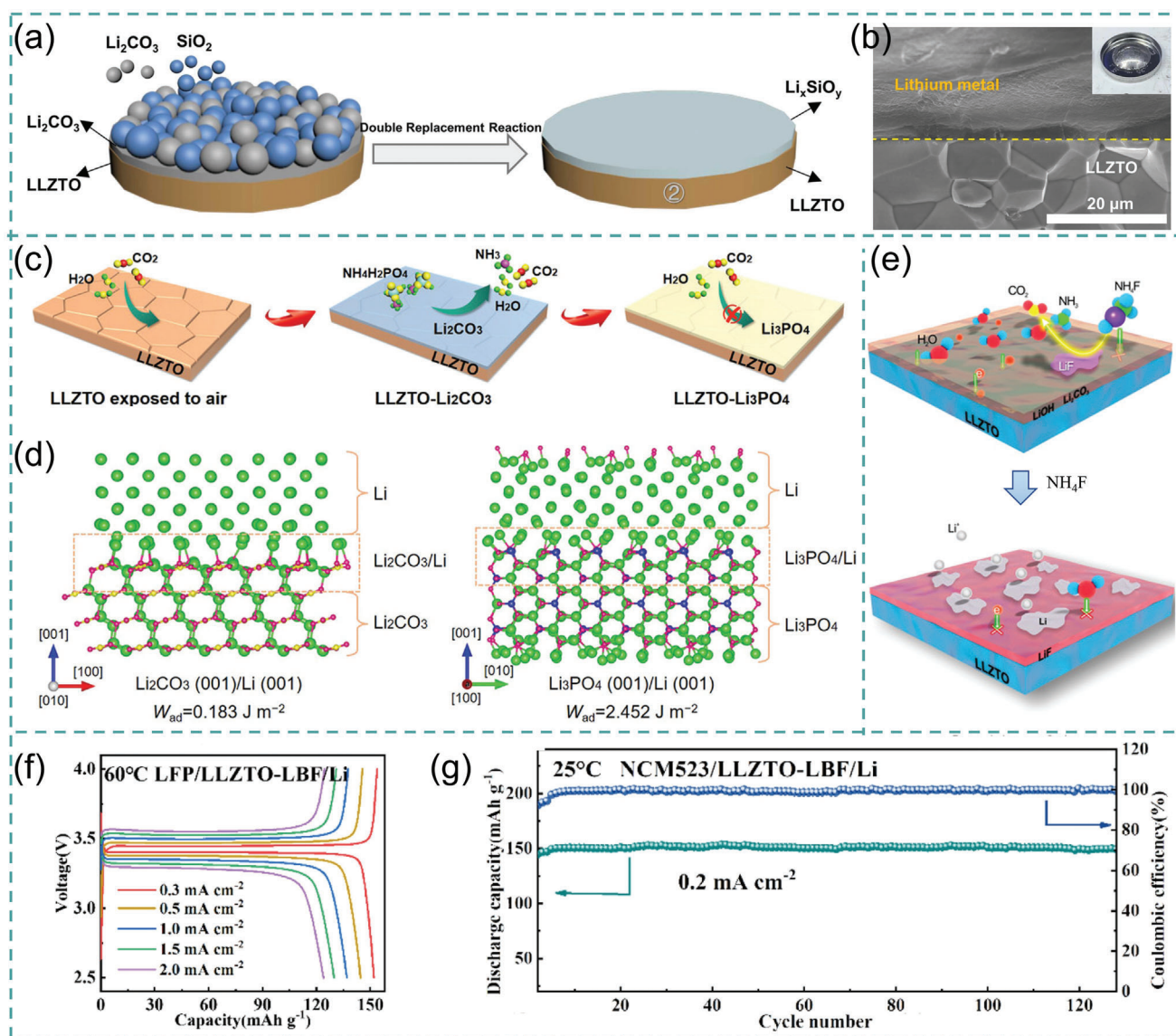


Figure 13. a) Schematic illustration of the preparation process of LLZTO pellet reacted with Li_2CO_3 and SiO_2 powders mixed in a mole ratio of 1:1; b) An SEM image showing the interface between Li metal and LLZTO pellet. Reproduced with permission.^[163] Copyright 2022, Elsevier. c) The formation process of LLZTO- Li_3PO_4 ; d) Atomic structures for fully-relaxed supercells of Li_2CO_3 (001)/Li (001) interface and Li_3PO_4 (001)/Li (001) interface. Reproduced with permission.^[164] Copyright 2022, Wiley. e) Schematic illustration of pellet interface treated by NH_4F . Reproduced with permission.^[165] Copyright 2020, Wiley. f) Voltage-capacity profiles and g) cycling performance of quasi-solid-state batteries with NCM523 at 25°C . Reproduced with permission.^[166] Copyright 2022, Elsevier.

advanced characterization methods, many studies have focused on using interface engineering methods to avoid the production of Li_2CO_3 /LiOH or remove the surface passivation layer to eliminate its effect on battery performance. Meanwhile, most of these studies are based on the existing presence of Li_2CO_3 /LiOH, resulting in unclear actual production mechanisms for Li_2CO_3 , an unclear minimum temperature for Li_2CO_3 removal, and unclear reasons for battery degradation. Therefore, it is necessary to combine advanced and sensitive in situ characterization techniques. Delluva et al.^[167] used operando electrochemical mass spectrometry to observe the real-time release of CO_2 and O_2 at a charging potential of 3.8 V. It has been confirmed that the gas overflow is

related to an increase in resistance at the cathode interface, providing direct evidence of Li_2CO_3 decomposition on the cathode side. Biao et al.^[168] discovered, through cryo-electron microscopy, that during lithium deposition, Li_2CO_3 at the grain boundaries of LLZO electrolyte undergoes a transformation into Li_xC with high electronic conductivity, thereby inducing infiltration of lithium dendrites. The introduction of Li_3AlF_6 as a sintering additive at the grain boundary, which regulates the ion and electron conduction properties at the grain boundary, can homogenize the Li^+ flux and reduce electron conductivity to inhibit the penetration of lithium dendrites along the grain boundaries. The assembled all-solid-state Li||LFP battery can be stably cycled for 5500 cycles

at a rate of 3 C, showing excellent stability. To gain a deeper understanding of the production and removal process of Li_2CO_3 and further promote the development of LLZO, Vema et al.^[169] studied the decomposition of surface impurity phases under different gas environments using two surface-sensitive techniques: near-ambient-pressure X-ray photoelectron spectroscopy and grazing incidence X-ray diffraction. The results revealed that the decomposition of $\text{Li}_2\text{CO}_3/\text{LiOH}$ on the surface of LLZO occurred at 500 °C regardless of the gas environment. Although the XPS results showed that the decomposition may not be complete, further increasing the temperature could lead to structural degradation of LLZO. Furthermore, annealing in a vacuum environment and under Ar gas conditions will result in the presence of residual graphitic carbon on the surface, which is detrimental to battery performance. However, any residual CO_2 or moisture will react with LLZO again and form a passivation layer after cooling down to ambient conditions. Therefore, annealing and cooling in an oxygen environment is the best solution to avoid contamination. However, Zhang et al.^[170] discovered that the decomposition temperature of Li_2CO_3 is ≈ 300 °C, significantly lower than the previously reported reaction temperature (ca., 500–620 °C). The reformation of Li_2CO_3 was also observed during the cooling process, indicating that the reaction between CO_2 and LLZO follows a thermodynamically favorable pathway. However, Zhou et al.^[171] pointed out that vacuum annealing can lead to the loss of Li and O, which subsequently leads to the structural degradation of LLZO. In contrast, argon annealing can remove pollutants while reducing the loss of Li and O. Since there is still much debate about the formation and removal of Li_2CO_3 , its complexity is demonstrated. Therefore, the development of more advanced characterization techniques is essential for carrying out research on LLZO-based solid-state batteries.

In summary, the study of Li_2CO_3 on the LLZO surface is limited to removal and conversion, which is insufficient for solving the problem of performance degradation in solid-state batteries. Even with advanced characterization techniques such as quasi in situ XPS, near-ambient-pressure X-ray photoelectron spectroscopy, grazing incidence X-ray diffraction, and cryo-electron microscopy, consistent conclusions regarding Li_2CO_3 could not be obtained. This indicates that further in-depth study of Li_2CO_3 is needed.

4.2. Compound Components in Positive Electrodes

LLZO exists in the composite positive electrode in three main forms: 1) as the coating layer for the active material of the positive electrode; 2) as the blending material with positive active material particles; 3) as the functional skeleton of positive active material (Figure 14a).

4.2.1. As a Coating Layer for Cathode Materials

The morphology, uniformity, and electrical conductivity of cathode materials greatly affect their electrochemical performance.^[172] In recent years, solid-state electrolyte-coated cathode materials have been found to improve the performance of conventional lithium-ion batteries.^[151,173] Solid-state electrolyte materials provide ionically conductive pathways between

adjacent active particles and act as a protective layer to suppress side reactions at the electrode/electrolyte interface.^[174]

Liu et al.^[175] used the garnet ceramic $\text{Li}_{6.5}\text{La}_3\text{Zr}_{1.5}\text{Ta}_{0.5}\text{O}_{12}$ as a functional nano-coating layer for NCM523 particles (Figure 14b,c), which improves the full cell cycling stability. Deng et al.^[176] coated spinel ($\text{LiMn}_{1.95}\text{Ni}_{0.05}\text{O}_{3.98}\text{F}_{0.02}$) cathode material with LLZO. The electrochemical performance shows that the LLZO-modified cathode material is better than that of the unmodified cathode material. After 100 cycles, the capacity decays by only 8.6% at 0.5 C and 55 °C, which confirms that the uniform LLZO coating (600 °C) can block the direct contact between the electrolyte and the spinel particles and effectively inhibit HF damage.^[177] Garnet electrolyte coatings have also been shown to reduce the electrode/electrolyte interface impedance and improve lithium-ion transport kinetics.^[178] Wei et al.^[179] proposed an electrochemical lithium supplement strategy utilizing $\text{Li}_{6.25}\text{La}_3\text{Zr}_2\text{Al}_{0.25}\text{O}_{12}$ (LLZAO) as a surface coating layer for a lithium-rich manganese-based cathode materials ($\text{Li}_{1.2}\text{Mn}_{0.54}\text{Ni}_{0.13}\text{Co}_{0.13}\text{O}_2$). In addition to providing 3D diffusion channels for Li^+ , the excess of Li^+ in LLZAO plays a crucial role in stabilizing the cathode structure through lithium layer insertion mitigating the spinel-like phase transformation. This method significantly improves the cycle and rate performance of the full cell. Notably, these solid-state electrolyte materials are poor electron conductors, therefore they are not conducive to providing electronic percolation pathways between the cathode material and the current collector. To this end, further studies have focused on the synergistic effect of carbon and garnet co-coating to improve the performance of cathode materials.^[180] Bai and co-workers^[181] co-coated the 0.4 mol% of LALZO ($\text{Li}_{7-3x}\text{Al}_x\text{La}_3\text{Zr}_2\text{O}_{12}$, denoted as LALZO-4) and carbon on the surface of LFP and confirmed that the spherical particles of LFP/C containing 5% of LALZO-4 were uniformly dispersed, improving the reversibility of the redox reactions (Figure 14d). The $\text{Li}_3\text{V}_2(\text{PO}_4)_3$ (LVP) cathode material co-coated with C and $\text{Li}_7\text{La}_3\text{Zr}_2\text{O}_{12}$ was proven to be ionic and electronically conductive, allowing Li^+ diffusion and electron transfer during charge/discharge processes.^[182] More importantly, the LLZO does not destroy the carbon layer of LVP (Figure 14e).

4.2.2. As a Blending Material for Positive Electrodes

The solid feature of both electrolytes and electrodes results in the inability of the electrolyte to infiltrate the cathode to construct lithium-ion transport channels.^[185] Therefore, many studies add solid-state electrolyte powders directly to cathode materials to increase Li-ion conductivity and reduce electrode polarization.^[186] For example, Heo et al.^[183] blended $(\text{Ni}_{0.8}\text{Co}_{0.1}\text{Mn}_{0.1})\text{OH}_2$ and $\text{La}_3\text{Zr}_2\text{Al}_{0.25}\text{OH}_x$ precursors to synthesize ionic conductor composites by co-precipitation and one-step sintering (Figure 14f). The modified cathode material exhibits excellent cycling and rate performance. Meanwhile, the all-solid-state battery assembled with 3D composite cathode materials ($\text{LiCoO}_2/\text{Li}_7\text{La}_3\text{Zr}_2\text{O}_{12}$) synthesized by self-assembled polystyrene-b-poly(4-vinylpyridine) block copolymer-template also shows excellent electrochemical performance and an active material utilization rate as high as 98%.^[187] Zhao et al.^[184] coated Li_3PO_4 on the surface of $\text{LiNi}_{0.8}\text{Co}_{0.1}\text{Mn}_{0.1}\text{O}_2$ (NCM811) cathode material, which was then mixed with $\text{Li}_{6.4}\text{La}_3\text{Zr}_{1.4}\text{Ta}_{0.6}\text{O}_{12}$ to

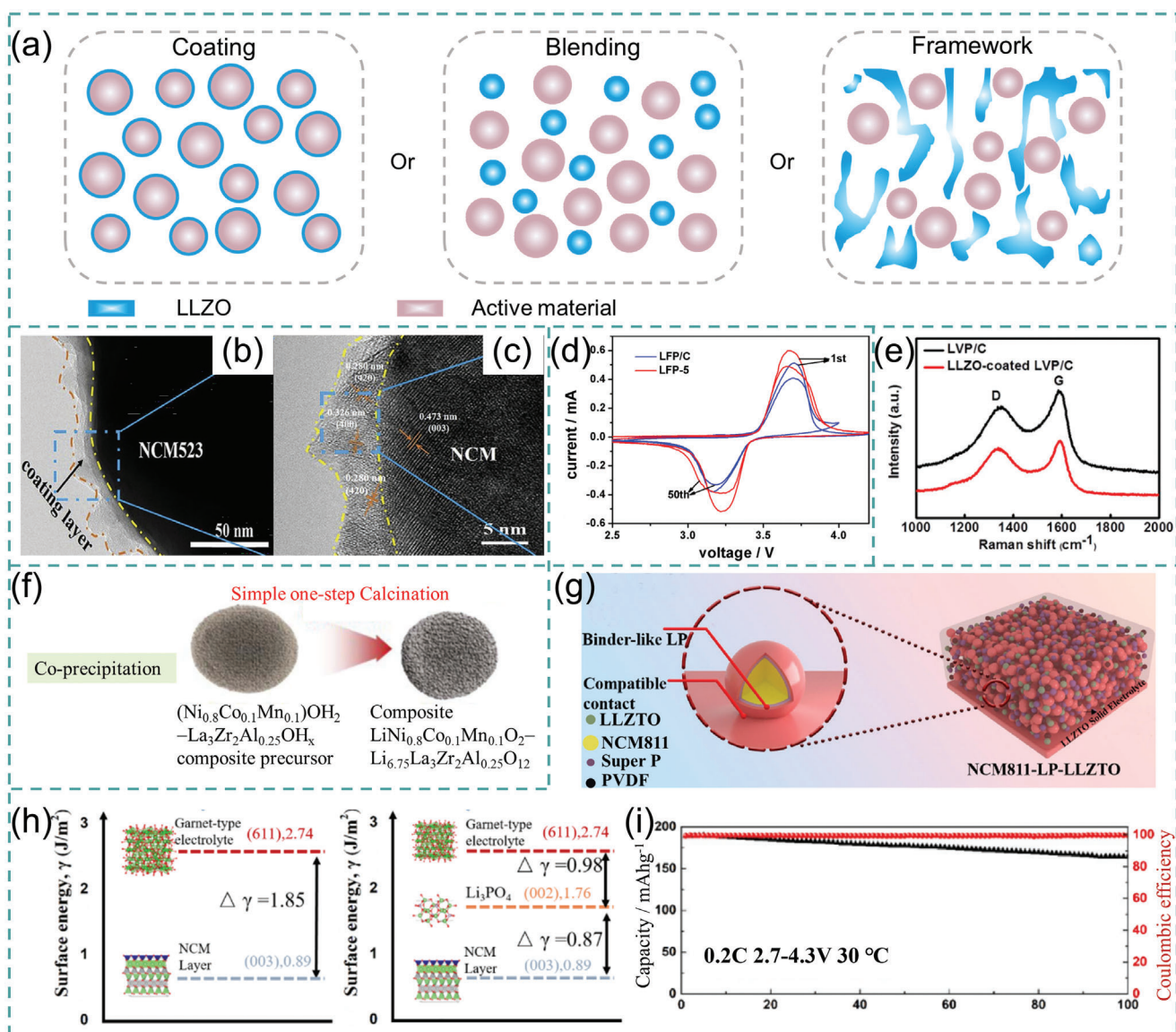


Figure 14. a) Schematic diagram of the three main existing forms of LLZO in composite electrodes. b) TEM and c) HRTEM image of LLZO coated NCM523. Reproduced with permission.^[175] Copyright 2020, Elsevier. d) Cyclic voltammetry of samples after 1 and 50 cycles. Reproduced with permission.^[181] Copyright 2020, Elsevier. e) Comparative Raman spectra of the LVP/C cathodes with and without LLZO coating. Reproduced with permission.^[182] Copyright 2017, The Electrochemical Society. f) The schematic diagram for the simple co-precipitation composite process. Reproduced with permission.^[183] Copyright 2018, The Electrochemical Society. g) Schematic diagrams of the introduced binder-like Li_3PO_4 . h) Schematic diagrams of the interface engineering for surface energy; i) Cycling performance at a rate of 0.2 C (30 °C). Reproduced with permission.^[184] Copyright 2020, Elsevier.

prepare cathode slurry (Figure 14g). Li_3PO_4 can effectively reduce the cathode/SSE interface impedance and space charge layer (Figure 14h). The solid-state battery exhibits excellent cycling performance, with an initial discharge capacity of 188.8 mAh g^{-1} and a capacity retention of 94% after 50 cycles at 0.2 C (30 °C) (Figure 14i). Similarly, SSBs assembled with LLZO electrolyte co-sintered with composite cathodes composed of $\text{LiNi}_{0.6}\text{Mn}_{0.2}\text{Co}_{0.2}\text{O}_2$ (NMC622), LLZO, and Li_3BO_3 also display excellent performance.^[188] LBO, exhibiting a melting point of 700 °C, functions as sintering additive to facilitate the binding of LCO and LLZO, and thereby establishing an efficient pathway

for lithium ion transport. Although this kind of method can establish an interface between LLZO and the active cathode, the capacity fading resulting from the loss of contact between the active cathode and LLZO during the electrochemical cycles remains significant, particularly under the condition of high active cathode mass loading.^[189] Although the current mass loading of the active cathode has been increased to $> 30 \text{ mg cm}^{-2}$, however, the cells barely last for 100 cycles. With the aid of transmission electron microscopy analysis, Hou et al.^[190] observed the interfacial delamination caused by repeated delithiation/lithiation of LCO, as well as oxygen vacancies and microcracks induced

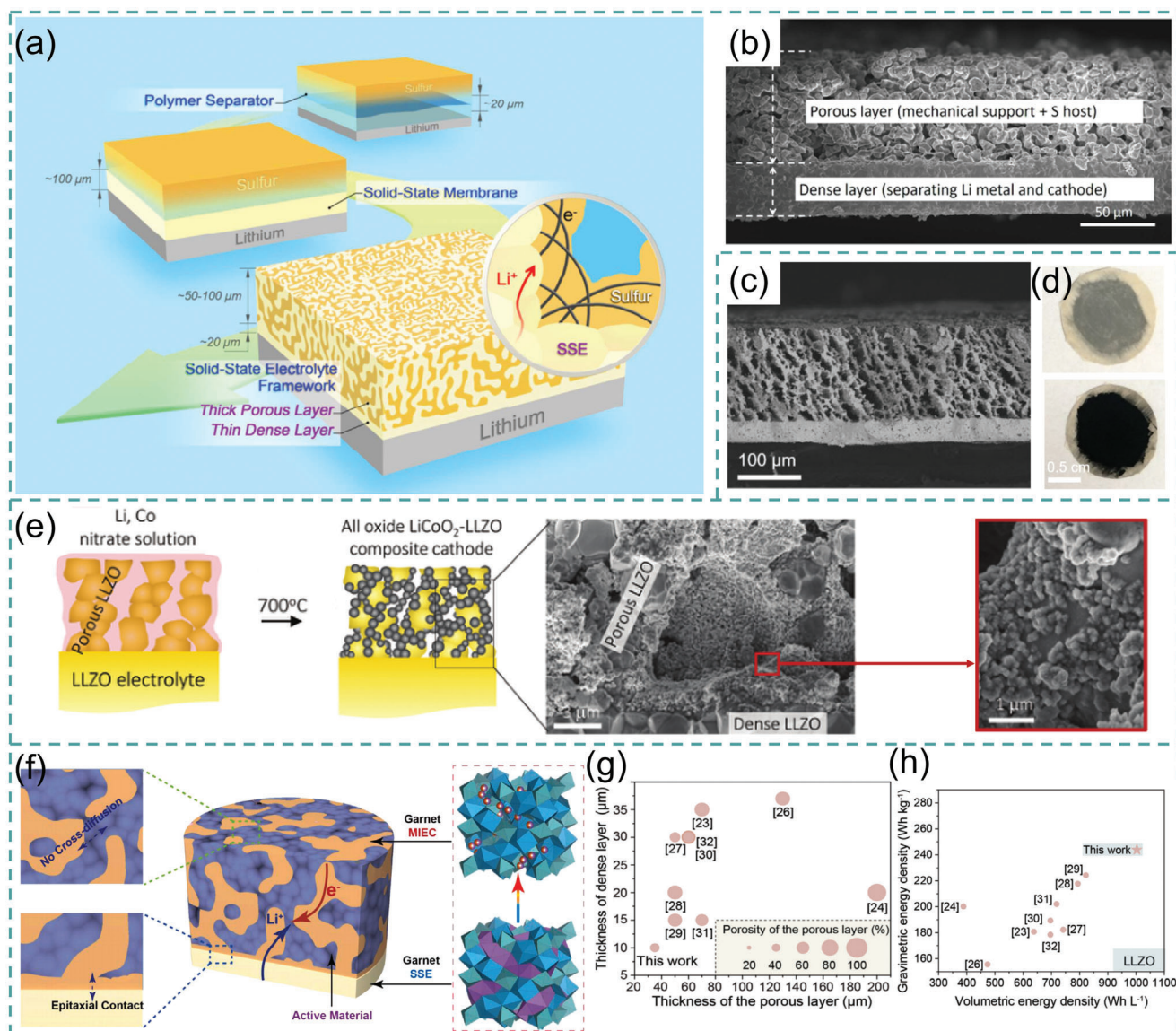


Figure 15. a) A scheme of the novel bilayer SSE framework in comparison with traditional soft polymer separators ($\approx 20 \mu\text{m}$) and rigid solid-state membrane architectures ($\approx 100 \mu\text{m}$); b) Cross-section of the bilayer garnet structure. Reproduced with permission.^[192] Copyright 2017, Royal Society of Chemistry. c) SEM fracture surface image of porous/dense (140/36 μm) bilayer; d) Optical image of cathode infiltrated LLZO bilayer. Reproduced with permission.^[193] Copyright 2020, American Chemical Society. e) Schematic illustration of the composite cathode. Reproduced with permission.^[194] Copyright 2020, The Royal Society of Chemistry. f) A scheme of garnet MIEC cathode framework with an enhanced charge transfer capability and excellent chemical compatibility to oxide cathode and garnet SSE. Reproduced with permission.^[195] Copyright 2023, Elsevier. g) Summary of thickness of previous and this work on dense/porous/dense films; (h) Comparison diagram of calculated gravimetric and volumetric densities of Li-garnet SSBs with LLZO/NCM811 cathode. Reproduced with permission.^[196] Copyright 2023, Wiley.

during the high-temperature sintering process, contributing to cyclic capacity decay and structural degradation. Therefore, achieving both a high active cathode mass loading and long cycle life remains critical yet challenging.

4.2.3. As a Framework for the Positive Electrodes

Constructing the LLZO porous structure to accommodate the cathode material within the framework, can facilitate the trans-

port of lithium ions at the interface.^[191] The porous structure is unable to support itself in a cell and is used in combination with a dense layer of solid-state electrolytes. Fu et al.^[192] prepared dense/porous bilayer solid-state electrolytes by a casting method (Figure 15a). The thick, porous framework offers continuous Li^+ /electron channels to carry the sulfur cathode, whereas the thin and dense layer acts as a barrier to prevent the shuttle of polysulfides and hinder the growth of lithium dendrites (Figure 15b). Therefore, lithium-sulfur cells (Li|SSE|S) exhibit a high initial Coulombic efficiency ($>99.8\%$). Yi et al.^[193] also constructed a

porous/dense bilayer LLZO solid-state electrolyte. The difference is that the porous layer consists of vertically aligned LLZO walls, which can effectively shorten the transport path of lithium ions (Figure 15c). The mixed slurry of the active material NMC622 and other components lithium bis((trifluoromethanesulfonyl)imide (LiTFSI) (4 mol%)/LiBOB (1 mol%)/succinonitrile (SN)) was subsequently infiltrated into the porous structure to form a composite cathode (Figure 15d). When combined with a lithium metal anode to assemble full batteries, the total RT impedance is $\approx 350 \Omega \text{ cm}^2$. Bilayer cells without the addition of SN showed sharply increased total impedance, that is $\approx 180 \text{ k}\Omega \text{ cm}^2$, demonstrating the crucial role of the mediator solid-state electrolyte. The direct synthesis of LCO cathodes from metal salts in porous LLZO scaffolds also shows promising results (Figure 15e), allowing good mechanical contact without adverse interfacial reactions at a low processing temperature ($700 \text{ }^\circ\text{C}$).^[194] A vertical array LLZO skeleton proposed by Shen et al. provides an idea for the construction of a composite cathode.^[150] Jin et al.^[195] developed a single-phase garnet-type mixed ion and electron conductor (MIEC) as a cathode skeleton and subsequently introduced transition metal cathodes into this skeleton (Figure 15f). The MIEC has the same crystal structure as the garnet solid-state electrolyte and transition metal elements similar to the oxide cathode materials, so they have good co-sintering stability with electrolyte and cathode, which provides a new strategy for solving the cathode interface problem of garnet-based SSBs. Notably, this double-layer structure is still at the early lab-scale stage and thus requires more effort to be adapted for large-scale production. The LLZO scaffold with a porous/dense/porous structure prepared by Zhang et al.^[196] has yielded remarkable outcomes in addressing the interface issues (both cathode/SSE and anode/SSE). Simultaneously, the 3D architecture also mitigates the problem of volume expansion during cycling. The thickness of its dense layer measures merely 8–10 μm (smaller than most reported literature), resulting in SSBs with gravimetric and volumetric energy densities of 279 Wh kg^{-1} and 1003 Wh L^{-1} , respectively (Figure 15g,h).

In summary, we conducted a comprehensive analysis of the merits and drawbacks associated with the utilization of 0D-3D LLZO in conjunction with active cathode materials for the formation of composite cathodes. It is evident that the utilization of a 3D LLZO skeleton structure in the composite cathode not only addresses the issue of cathode/electrolyte interface, but also enables high mass loading active cathodes to be fabricated. Therefore, this approach is widely recognized as a viable and effective strategy for achieving high-energy density solid-state batteries. However, the poor cycle life poses significant challenges to this approach, necessitating advanced characterization techniques for comprehending the underlying causes of performance degradation and facilitating its advancement.

4.3. Solid-State Electrolytes

Kravchik et al.^[197] demonstrated that the LLZO electrolyte can be used solely as the solid-state electrolyte for the battery. The early development efforts were mainly focused on how to improve the Li-ion conductivity of LLZO (target value: 10^{-4} – $10^{-3} \text{ S cm}^{-1}$). LLZO as a solid-state electrolyte has two forms: one is in

the form of a rigid ceramic pellet and the other is as a component of a composite solid electrolyte combining ceramic with flexible polymer.

4.3.1. Garnet-Type Pellets

The thickness of ISEs typically exceeds $400 \mu\text{m}$. According to the formula $t = L^2/D$ (where t , L , and D represent Li^+ diffusion time, SEs thickness, and Li^+ diffusion constant, respectively), a thin SE will reduce internal resistance. According to Kravchik,^[198] commercially desired battery energy densities (ca. 250 and 700 Wh kg^{-1}) can be achieved on condition that SSBs enable a cathode areal capacity beyond 3.5 mAh cm^{-2} and LLZO electrolyte thickness in the range of 20–50 μm . The current state of electrolyte development indicates that there is still a significant gap to bridge before achieving commercial viability. For example, Jonson et al.^[199] fabricated a thin film electrolyte of $\text{Li}_{6.25}\text{Al}_{0.25}\text{La}_3\text{Zr}_2\text{O}_{12}$ with a thickness of $\approx 100 \mu\text{m}$ using the solution casting method. However, the article does not provide relevant electrochemical performance data. The presence of Figure 16a,b, along with its relative density of $\approx 90\%$, suggests the prevalence of closed pores within the LLZO block. Therefore, despite the progress made in reducing electrolyte thickness in this article (Figure 16c), there are still existing defects that impede further verification of its electrochemical performance. Additionally, Wu et al.^[200] employed an atmospheric plasma spraying (APS) technology to synthesize LLZO films with thicknesses ranging from 30 to $300 \mu\text{m}$ (Figure 16d). However, the electrochemical performance test exclusively employed a self-supporting LLZO film of $300 \mu\text{m}$. This evidence further supports the aforementioned perspective. Yan et al.^[201] used high-energy ball milling to prepare nanoscale LLZO slurries and then coated directly on cathode electrodes obtaining ultra-thin solid-state electrolytes (≈ 2 – $3 \mu\text{m}$) (Figure 16e). The Li||LFP all-solid-state battery shows excellent electrochemical performance. This study successfully developed a simple and low-cost process for fabricating micron-scale thin solid-state electrolyte layers. To further reduce the thickness, Sastre et al.^[202] prepared submicron (Al, Ga) doped LLZO thin films without impurity phases by co-sputtering the co-doped LLZO and Li_2O targets (Figure 16f,g). It is worth noting that the Li-ion conductivity ($1.9 \times 10^{-4} \text{ S cm}^{-1}$) of the prepared LLZO thin film is comparable to the previously reported thick LLZO, but the thickness is three orders of magnitude lower (500 nm). Moreover, the thin film can be prepared at a temperature as low as $400 \text{ }^\circ\text{C}$, which is conducive to energy-dense packaging and energy saving. Saccoccio et al.^[203] adopted the pulsed laser deposition (PLD) technology to prepare $\text{Li}_{6.4}\text{La}_3\text{Zr}_{1.4}\text{Ta}_{0.6}\text{O}_{12}$ films with a thickness of ≈ 30 – 50 nm (Figure 16h). The effectiveness of PLD, magnetron sputtering, and APS techniques in controlling electrolyte thickness has been demonstrated.^[204] However, thin inorganic solid electrolytes are fragile, and brittle and are difficult to remain intact during the cycling of batteries. Furthermore, these costly and time-consuming technologies are not easily scalable to mass production and large-scale processing.

Another critical issue of LLZO lies in the interfacial problems between the inorganic solid electrolyte and the electrode, which are attributed to 1) the point-to-point solid contact leading to poor interfacial contact^[205]; 2) the generation of byproducts as a result

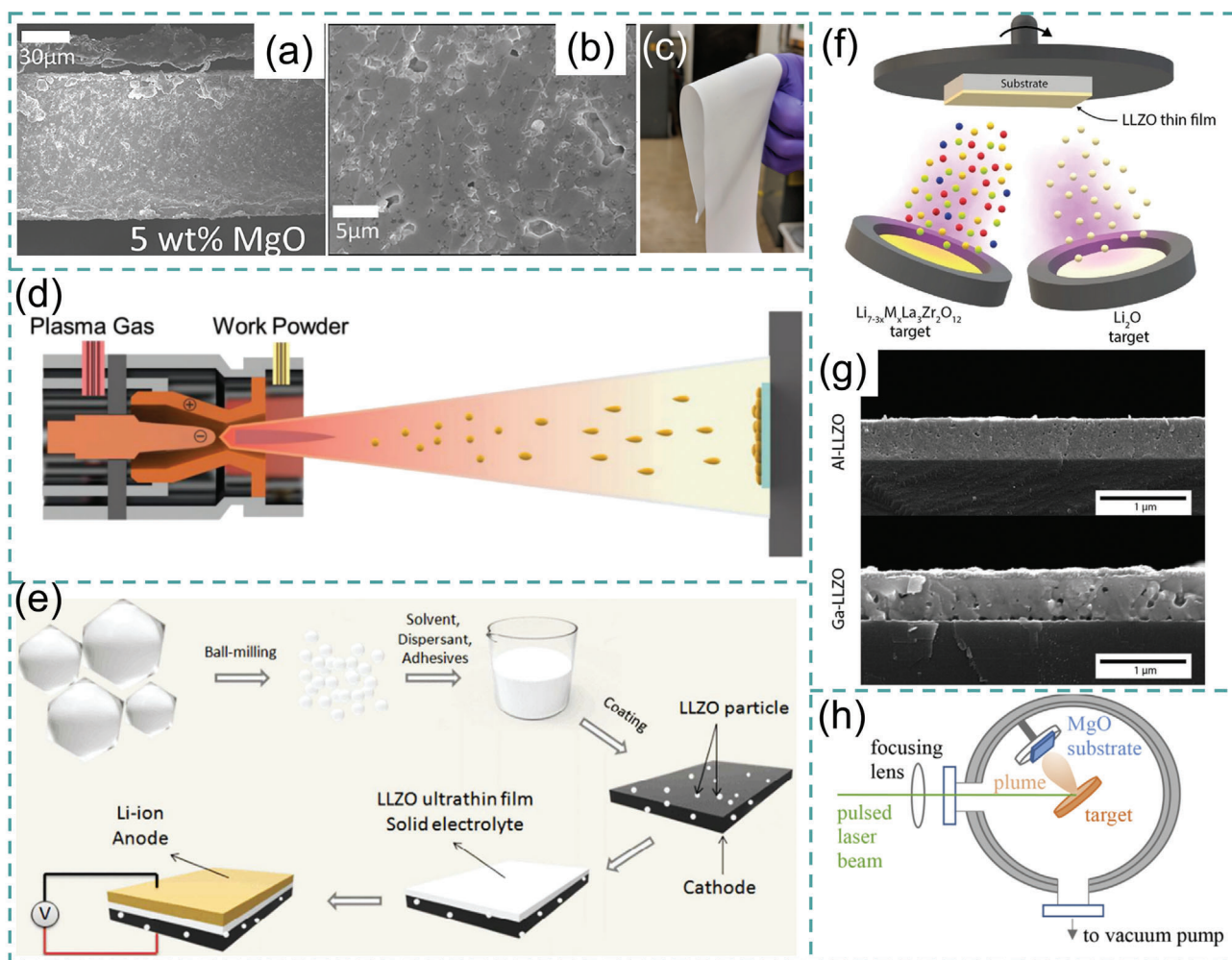


Figure 16. a,b) Cross-sectional SEM images of $\text{Li}_{6.25}\text{Al}_{0.25}\text{La}_3\text{Zr}_2\text{O}_{12}$ sheets; c) Photographs of green $\text{Li}_{6.25}\text{Al}_{0.25}\text{La}_3\text{Zr}_2\text{O}_{12}$ tapes. Reproduced with permission.^[199] Copyright 2021, American Chemical Society. d) Schematic illustration of the spray torch. Reproduced with permission.^[200] Copyright 2023, Wiley. e) Schematic illustration of the synthesis procedure. Reproduced with permission.^[201] Copyright 2017, American Chemical Society. f) Scheme of co-sputtering deposition process employed to deposit over-lithiated LLZO thin films; g) SEM images of an Al-doped LLZO and a Ga-doped LLZO film. Reproduced with permission.^[202] Copyright 2020, Wiley. h) Schematic illustration of the deposition principle. Reproduced with permission.^[203] Copyright 2017, Elsevier.

of the mismatch between LLZO and cathode material, hindering the electrode reaction and consuming the cathode material to deteriorate the battery performance. Hence, research has focused on the interface studies of ISEs in terms of interface modification including both the cathode/electrolyte interface and the anode/electrolyte interface.

Interface Between LLZO and Cathode: An earlier solution addressing the cathode/electrolyte interface contact issue is to in situ or ex situ coat LLZO pellet with cathode materials and annealing at high temperature.^[206] However, this method suffers from poor physical bonding and cross-reactions between the cathode material and the electrolyte.^[207] The study conducted by Demuth et al.^[208] demonstrated a reactive phase transformation from layered phase to NiO (rock salt)-like structure at temperatures as low as 500–600 °C. This transformation directly contributes to the degradation of the electrochemical properties. Constructing a buffer layer (i.e., liquid electrolytes, ionic liquids,

and flexible polymers) between the cathode and electrolyte is the most commonly used method (Figure 17a). Among the options, the direct addition of liquid electrolyte and ionic liquid seems to be the simplest method, whereas, the polymer-based interfacial buffer layer enables better contact and maintains higher safety features.^[209] Sarkar et al.^[210] employed an interface modification layer consisting of LiPF_6 -based liquid electrolyte with AlCl_3 Lewis acid and fluoroethylene carbonate to alleviate the interface impedance between $\text{Li}_7\text{La}_{2.75}\text{Ba}_{0.25}\text{Zr}_{1.75}\text{Ta}_{0.25}\text{O}_{12}$ and the electrode. The lithium symmetric battery exhibits stable cycling for over 3000 h at a current density of 0.5 mA cm^{-2} (Figure 17b). Flexible PEO polymers are often used as electrode/electrolyte interface buffer layers.^[5ac] For example, Chi et al.^[211] successfully synthesized the multilayer solid-state electrolyte by placing a polymer electrolyte (PEO + LiTFSI; $\approx 8 \mu\text{m}$) on both sides of a LLZTO pellet ($\approx 400 \mu\text{m}$) (Figure 17c) The solid-state full cell at 90 °C shows a stable cycling capability, maintaining a capacity

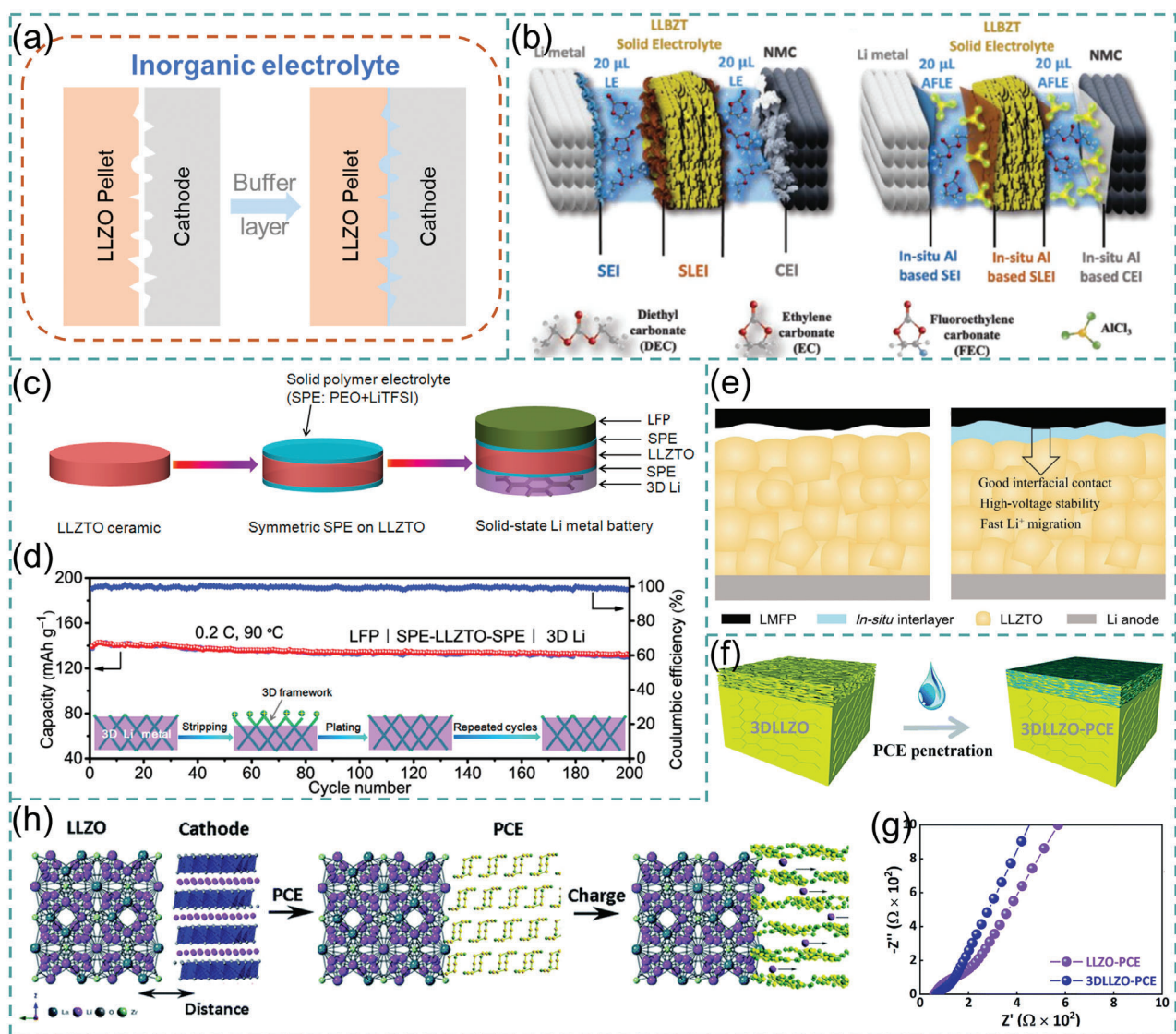


Figure 17. a) Comparative scheme demonstrating the effect of cathode/electrolyte interface modification. b) Schematic illustration of interphase formation in a hybrid cell. Reproduced with permission.^[210] Copyright 2023, Wiley. c) Schematic illustration of the fabrication process and d) cycling stability of SSBs (0.2 C, 90 °C; 1 C = 170 mA g⁻¹). Reproduced with permission.^[211] Copyright 2018, Elsevier. e) Schematic illustration of the impact of in situ interlayer for high-voltage SSBs. Reproduced with permission.^[212] Copyright 2024, Springer. f) Schematic illustration of 3D electrolyte; g) Impedance plots of samples; h) Microscopic view of the Li⁺ transfer path in electrode/electrolyte interfaces via molecular reorganization. Reproduced with permission.^[213] Copyright, 2021, Royal Society of Chemistry.

of 135 mAh·g⁻¹ with a high Coulombic efficiency of ≈99.6% after 200 cycles (Figure 17d). The in situ polymerization reaction is considered a promising approach to address the interface issues. The modification layer demonstrates properties that bridge those of liquid electrolytes and solid-state electrolytes, thus being termed as quasi-solid-state electrolytes. A precursor solution containing poly(ethylene glycol) diacrylate (PEGDA), SN, LiTFSI, and an initiator was utilized at the LLZTO/cathode interface. Through employing a self-polymerization reaction of PEGDA at 70 °C, the impedance at the cathode/electrolyte interface was effectively reduced to approximately the level of liquid batteries (Figure 17e).^[212] However, the high voltage instability and low room temperature ionic conductivity of most polymer elec-

trolytes prevent them from matching the high energy density cathode with high potential. Therefore, this poses challenges to the advancement of high energy-density solid-state batteries. A 3D LLZO framework generated by acid treatment was selected as the rigid scaffold for plastic crystal electrolytes (SN + LiTFSI) (Figure 17f).^[213] The rapid molecular redirection of SN enables a fast response to structural changes occurring at the interface and creates channels for efficient diffusion of Li⁺. Molecular recombination through Li⁺ diffusion significantly reduces interfacial and total resistance (Figure 17g,h). This eventually results in the Li-ion conductivity of up to 3.88 × 10⁻⁴ S cm⁻¹, an electrochemical window of ≈4.7 V, and a Li-ion transference number (t_{Li+}) of 0.65.

Interface Between LLZO and Anode: The wettability of lithium metal to LLZO is poor causing large interfacial resistance and the uneven deposition of lithium metal leads to the generation of lithium dendrites, triggering severe safety hazards of the battery.^[214] Therefore, increasing the Li wettability on the surface of LLZO, increasing the effective contact of electrolyte/electrode interface, reducing the interfacial resistance, improving the interface stability, and inhibiting the generation of lithium dendrites are the prominent research areas for the Li/LLZO interface.

Various strategies have been applied to improve the interface resistance of LLZO/Li. First of all, to ensure the conformal interfacial contact between Li and LLZO, similarly, liquid electrolytes, ionic liquids, and solid polymer buffer layers are also employed to modify the anode interfaces. Nevertheless, the properties of these buffer layers are quite different when compared to those adopted for the cathode/SSE interfaces. It is a prerequisite that the negative electrode/electrolyte interface modification layer should acquire good cathodic stability to avoid being reduced by the highly reactive lithium metal.^[215] For example, Deng et al.^[216] prepared the gel polymer electrolytes composed of LLZTO and PEGDA via an ultraviolet (UV) curing polymerization method. The distribution of LLZTO within the polymer matrix constitutes a concentration gradient. Such a design allows the side with a high LLZTO content to keep in contact with the cathode to facilitate high oxidation resistance and robust mechanical strength, on the other side, the flexible LLZTO-free is in close contact with the Li metal. Similarly, Zhou et al.^[217] reported a double-layer polymer solid-state electrolyte in which the poly(*N*-methyl-malonic amide)-LiTFSI layer is only in contact with the cathode to ensure compatibility with the high-voltage cathode, and the PEO-LiTFSI layer is only in contact with the anode to provide the interfacial stability of the electrolyte/Li.

Second, it is known that one of the major reasons for the high interfacial resistance between LLZO and Li lies in the surface contamination of Li_2CO_3 . In this regard, the Li_2CO_3 transformation method mentioned in Section 4.1.2 represents a widely adopted approach to effectively mitigate the interface impedance of Li/LLZO. For instance, the introduction of LiPO_2F_2 to chemically react with $\text{Li}_2\text{CO}_3/\text{LiOH}$ results in the formation of a $\text{LiF-Li}_2\text{PO}_3\text{F}$ interface layer. The Li||Li symmetric cell demonstrates a significantly reduced interface impedance of $5.1 \Omega \text{ cm}^2$.^[218] The $\text{Li}_{6.5}\text{La}_3\text{Zr}_{1.5}\text{Ta}_{0.5}\text{O}_{12}$ was subjected to nitrogen plasma gradient doping (denoted as LLZTON-3; power: 400 W; sputtering time: 30 s), resulting in the formation of a Li_3N -modified layer on the surface of Li/LLZO through an in situ reaction that effectively eliminates the presence of Li_2CO_3 impurity on LLZO surface (Figure 18a,b).^[219] Consequently, the interface impedance of the Li||Li symmetrical battery is reduced to $<3.5 \Omega \text{ cm}^2$. Sharafi et al.^[220] pointed out that wet polishing is more effective than dry polishing in terms of lowering surface carbonate content. When combined with the heat treatment process (up to 500°C) the $\text{Li}_2\text{CO}_3/\text{LiOH}$ can also be effectively removed, thereby significantly reducing the interface resistance of LLZO/Li ($2 \Omega \text{ cm}^2$). Similarly, treating the impure phase on the LLZTO surface with CH_3COOH can reduce the interfacial impedance of Li/LLZTO from 5542 to $5 \Omega \text{ cm}^2$.^[221]

Third, adopting inorganic interfacial modification layers to improve the compatibility between LLZO and Li is also verified to

be effective. To date, various materials including Al, Cu, Si, Mg, Al_2O_3 , Li_3N , Cu_3N , SnF_2 , and graphite have been used to reduce the interface resistance between Li metal and LLZO.^[222] Utilizing alloying reactions has been widely adopted to reduce the interfacial impedance. A Cu-doped Li_3Zn bifunctional layer designed by magnetron sputtering technology and in situ alloying reaction can induce uniform deposition of Li, retaining good interfacial contact, even after 100 h of cycling (Figure 18c).^[15q] Adopting the same technique, a 3D porous Zn layer is incorporated into the Li/LLZTO interface, resulting in the formation of a 3D Li-Zn alloy layer through the reaction between Zn and molten Li (Figure 18d).^[223] Consequently, the impedance at the interface is significantly reduced from 319.8 to $1.9 \Omega \text{ cm}^2$. Stockham and co-workers^[224] achieved an interfacial alloying layer by enhancing dopant exsolution, especially with $\text{Li}_{6.4}\text{Ga}_{0.2}\text{Nd}_3\text{Zr}_2\text{O}_{12}$ in the form of Ga-Li eutectic, enabling a very low electrode/electrolyte interfacial area specific resistance of $67 \Omega \text{ cm}^2$. On the other hand, composite anodes such as Li-C, Li-Mo, Li-Na, Li- $\text{Li}_4\text{Ti}_5\text{O}_{12}$ (LTO), and Li- TiO_2 have also been shown to be beneficial.^[225] For instance, the replacement of a Li metal anode with a composite anode consisting of Li-LTO can significantly decrease the interface impedance of Al-doped LLZO/electrode from 249 to $27 \Omega \text{ cm}^2$ (Figure 18e,f). The main contributions of LTO include the mitigation of electrode volume expansion during cycling, and the enhanced electronic conductivity of the anode resulting from the reduction of Ti^{4+} by lithium metal.^[226] Notably, the in situ introduction of mixed electron-ion interface phases is revealed to be effective in reducing the areal interfacial resistance between the electrolyte and lithium metal. Composites containing Ti^{4+} and Ge^{4+} that can be reduced by lithium metal to produce electron-ion mixed conductors are commonly selected.^[227] Targeting resolving the issues of some modification methods (i.e., poor repeatability, low yield, and expensive cost), Gao et al.^[228] employed a simple ultrasonic spraying technique to apply a composite modification layer of In_2O_3 and SnO_2 on the $\text{Li}_{6.25}\text{Ga}_{0.25}\text{La}_3\text{Zr}_2\text{O}_{12}$ pellets (Figure 18g). Through activation, the composite layer transforms into multifunctional interlayers comprised of $\text{Li}_{13}\text{In}_3$, Li_2O , and LiInSn . Specifically, the LiInSn acts as a binder between Li and SSE, while $\text{Li}_{13}\text{In}_3$ plays a crucial role in adjusting the distribution of the electric field, thereby achieving uniform deposition of Li. Additionally, the unique electronic insulation properties of Li_2O prevent the reduction of Li^+ . By constructing this multifunctional layer, surprisingly, the interfacial compatibility is substantially enhanced, achieving a CCD as high as 12.05 mA cm^{-2} . Furthermore, stable cycling for over 2000 h can be achieved at 2 mA cm^{-2} . The breakthrough improvement of CCD paves the way for further advancements in all-solid-state batteries.

To sum up, the application based on garnet pellet faces great challenges, such as, 1) the presence of an impurity phase of Li_2CO_3 on the surface hinders lithium infiltration and promotes the growth of lithium dendrites; 2) insufficient contact between the electrode and electrolyte interface, as well as increased impedance at the interface due to solid–solid contact remain unsolved; and 3) the rigidity and brittleness of ceramic pellet limit their thinning and large size preparation, thereby restricting the energy and power density of solid-state batteries. Meanwhile, the challenging preparation conditions and high costs also hinder its commercial application, thus making

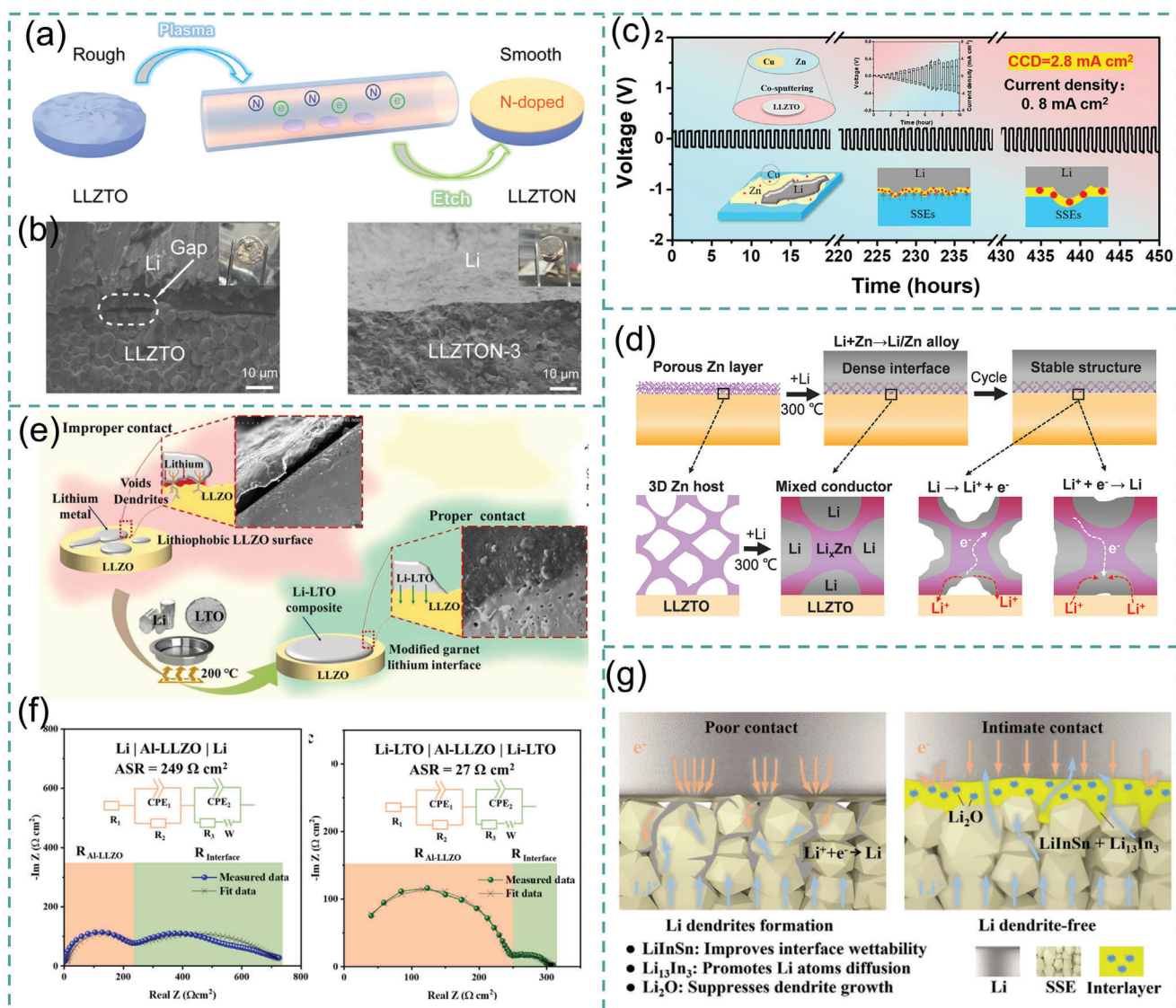


Figure 18. a) Schematic diagram illustrating the preparation of LLZTON-3 via N_2 plasma treatment; b) Cross-sectional SEM images of LLZTO/Li and LLZTON-3/Li. Reproduced with permission.^[219] Copyright 2023, American Chemical Society. c) Cycling stability under a current density of 0.8 mA cm^{-2} . Reproduced with permission.^[15q] Copyright 2021, American Chemical Society. d) Schemes of the interfaces, and the enhanced kinetics and stable structure of LLZTO/Li interface during cycling. Reproduced with permission.^[223] Copyright 2021, Elsevier. e) Mechanism diagram of Li-LTO composite anode improving electrode/electrolyte interface impedance; f) EIS result of symmetric cells made with pristine lithium and Li-LTO composite anode. Reproduced with permission.^[226] Copyright 2023, Elsevier. g) Schematic diagram illustrating the interface between Li metal and SSE (with and without the modification interlayer). Reproduced with permission.^[228] Copyright 2023, Wiley.

research on organic/inorganic composite solid-state electrolytes more promising for practical applications.

4.3.2. Garnet-Type Composite Membranes

Although the shear modulus of ISEs is much larger than that of lithium metal,^[229] lithium dendrites growing along the grain boundaries of rigid SSEs toward the cathode have been observed causing short-circuiting of the battery.^[230] Solid polymer electrolytes possess salient advantages such as shape versatility and flexibility, however, they are mostly impeded by their low RT Li-

ion conductivity (10^{-5} – $10^{-7} \text{ S cm}^{-1}$).^[231] Organic-inorganic composite solid electrolytes combining the high Li-ion conductivity of inorganic solid electrolytes with the high flexibility of polymer electrolytes are currently one of the most popular strategies. Garnet LLZO mainly exists in two forms within composite solid electrolytes: 1) as an active filler and 2) as a 3D framework for CSEs.

0D and 1D LLZO Filler: Usually, LLZO-based CSEs are composed of LLZO, lithium salts (e.g. LiTFSI, LiClO_4 , lithium tetrafluoroborate), and polymers (such as PEO, polyethylene glycol, polypropylene chloride, polyvinylidene fluoride (PVDF), poly(vinylidene fluoride-hexafluoro propylene)

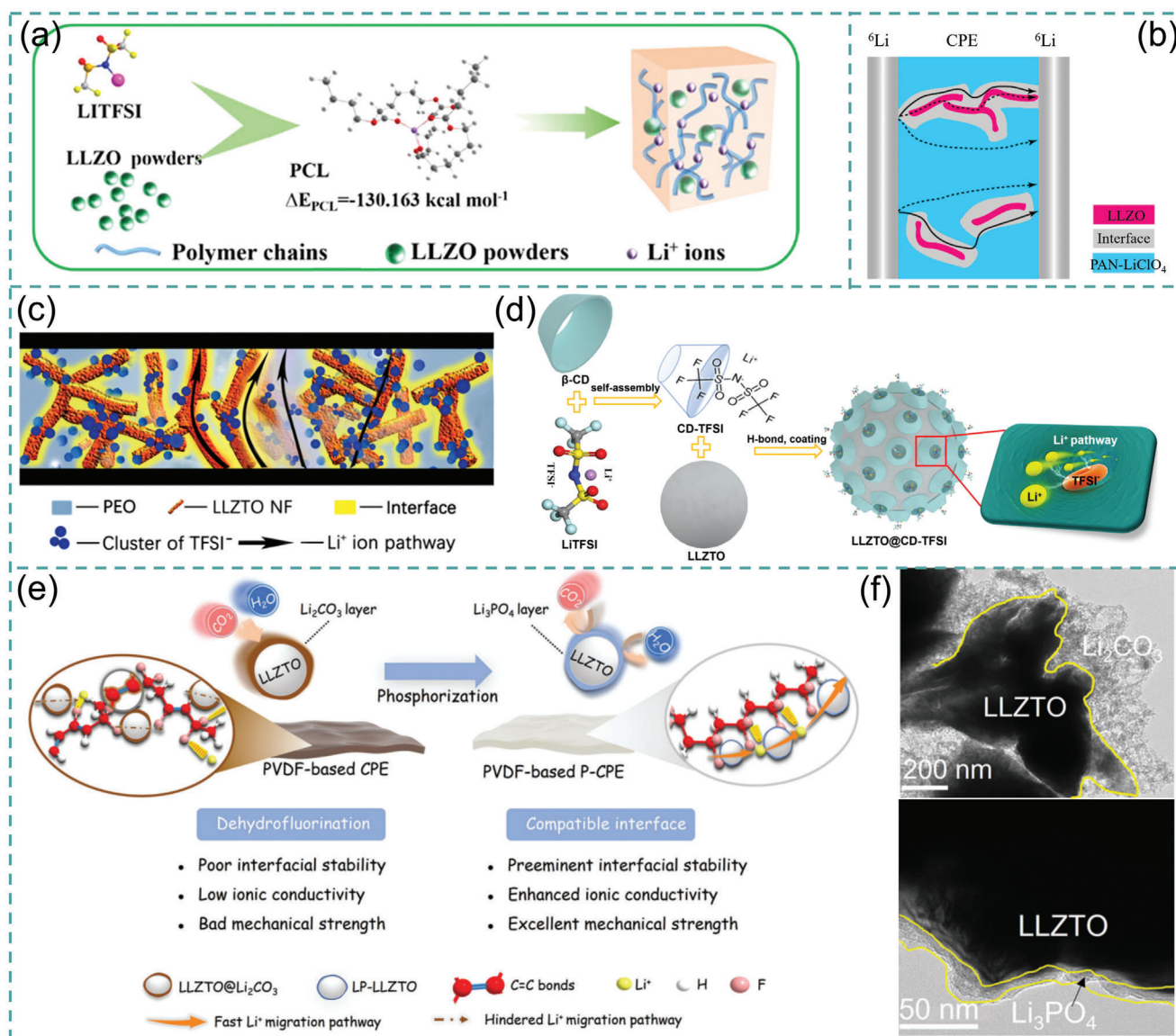


Figure 19. a) Schematic diagram illustrating the preparation of CSEs with LLZO particles. Reproduced with permission.^[234] Copyright 2023, American Chemical Society. b) A scheme showing possible Li^+ transport pathways in the film. Reproduced with permission.^[15k] Copyright 2017, American Chemical Society. c) Ionic conducting mechanism of the nanofiber reinforced polymer-in-salt PEO-based CSE. Reproduced with permission.^[238] Copyright 2020, American Chemical Society. d) Modified process for $\text{Li}_{6.75}\text{La}_3\text{Zr}_{1.75}\text{Ta}_{0.25}\text{O}_{12}$ combining active β -cyclodextrin and LiTFSI salt. Reproduced with permission.^[244] Copyright 2024, Wiley. e) Schematic diagram illustrating the inhibition of PVDF chain dehydrofluorination by surface phosphorization of LLZTO; f) TEM images of LLZTO particles. Reproduced with permission.^[245] Copyright 2023, Wiley.

(PVDF-HFP), polyacrylonitrile (PAN), poly(ϵ -caprolactone) (PCL), 1,3-dioxolane (DOL), and PEGDA, and so on).^[13,232] Generally, CSEs have better thermal stability, high Li-ion conductivity, and stable electrochemical performance.^[233] For example, the composite solid electrolyte, consisting of PCL as the polymer matrix, LiTFSI as the lithium salt, and LLZO powder as the ceramic filler (Figure 19a), exhibits a high Li^+ transference number (≈ 0.71). The assembled Li||LFP full battery demonstrates stable cycling performance up to 600 cycles at 2 C, with a superior capacity retention rate of 85%.^[234]

Compared with nano-particles, 1D, or quasi-1D fillers such as nanowires, nanorods, and nanofibers can provide more con-

tinuous ion transport channels for Li^+ .^[235] The CSE composed of PEO, LiTFSI, and LLZO nanowires has also been proven to have a Li-ion conductivity up to $2.39 \times 10^{-4} \text{ S cm}^{-1}$ at 25 °C,^[236] higher than other similar CSEs filled with LLZO particles ($1.17 \times 10^{-4} \text{ S cm}^{-1}$).^[237] Incorporating only 5% of c-LLZO nanowires into the PAN-LiClO₄,^[15k] the as-obtained CSE increases the RT Li-ion conductivity by three orders of magnitude (from $\approx 10^{-7} \text{ S cm}^{-1}$ to $1.31 \times 10^{-4} \text{ S cm}^{-1}$) (Figure 19b). Fan et al.^[238] also confirmed that the addition of $\text{Li}_{6.75}\text{La}_3\text{Zr}_{1.75}\text{Ta}_{0.25}\text{O}_{12}$ nanofibers (Figure 19c) into PEO-based solid electrolytes achieves a high RT Li^+ transference number (0.57), a high Li-ion conductivity ($2.13 \times 10^{-4} \text{ S cm}^{-1}$), and good cycling stability. The Li||LFP exhibits a

capacity retention rate of 83.1% after 200 cycles at a temperature of 40 °C and a discharge rate of 0.2 C.

However, nanofillers can easily aggregate in the polymer substrate due to their high surface energy, which affects the transport of lithium ions. Agglomeration leads to discontinuity of the interface phase, and the contact area between the polymer matrix and the ceramic filler decreases, thus increasing the overall impedance of batteries. To solve this problem, the interfacial energy barrier between the polymer substrate and the ceramic powder is effectively reduced by introducing modification layers such as polydopamine,^[239] 1-propyl-3-methylimidazolium bis (trifluoromethanesulfonyl)imide,^[240] sodium itaconate,^[241] stearic acid,^[242] and maleic acid.^[243] The results demonstrate that these interfacial modification layers effectively enhance the Li⁺ ion transport at the interface. However, direct Li⁺ transport between the polymer phase and LLZO is hindered by the high interfacial impedance. Therefore, Lu et al.^[244] opted to modify the Li_{6.75}La₃Zr_{1.75}Ta_{0.25}O₁₂ by incorporating a functional supramolecular interface modification layer assembled using active β-cyclodextrin and LiTFSI salt (Figure 19d). The presence of numerous hydrogen bonds formed among β-cyclodextrin, PEO matrix, and Li_{6.75}La₃Zr_{1.75}Ta_{0.25}O₁₂ enables the achievement of uniformly dispersed LLZO particles and a tightly integrated polymer/ceramic interface. Additionally, ⁶Li NMR spectra confirmed the successful transfer of Li⁺ ions from the PEO polymer matrix to the LLZO ceramics, thereby providing a novel pathway for lithium-ion transport. Furthermore, the utilization of phosphoric acid with citric acid as a chelating agent has yielded promising outcomes in converting Li₂CO₃ on the LLZO surface to Li₃PO₄ (Figure 19e,f). The Li-ion conductivity of the CSE was enhanced from 1.88 × 10⁻⁵ to 1.9 × 10⁻⁴ S cm⁻¹. This approach not only resolves the issue of interfacial incompatibility between PVDF-HFP polymer and LLZO particles but also, offers a novel strategy for inhibiting dehydrofluorination of PVDF-HFP.^[245] In conclusion, surface modification of LLZO is a feasible way to improve the dispersion of nano-particles, which is also applicable to the modification of nanowires and nanorods.^[246]

3D LLZO Network: Electrospinning technology is a common method for synthesizing 3D continuous structures.^[15r,247] Gao et al.^[248] synthesized a 3D Li_{6.4}La₃Zr_{1.4}Ta_{0.6}O₁₂/PVDF fiber mat of discontinuous LLZO ceramic particle (Figure 20a), and cast a mixed solution of PEO and lithium salt onto the fiber to form a CSE. Although this structure can reduce the crystallinity of PEO and enhance the Li-ion conductivity of CSE, it should be noted that discontinuous LLZO particles do not offer continuous pathways for Li-ion transport. Therefore, Zhang et al.^[249] fabricated a 3D framework by integrating interconnected LLZO particles with polymers (Figure 20b,c). The cross-connection points between the fibers can ensure the continuity of Li-ion transport, thus exhibiting a high σ_{Li^+} of 1.05 × 10⁻⁴ S cm⁻¹ (50 °C), an order of magnitude higher than that of the polymer nanofiber-based composite electrolyte (2.53 × 10⁻⁵ S cm⁻¹). This work not only solved the particle agglomeration issue, but also enhanced the mechanical properties (Figure 20d), Li-ion conductivity, and Li⁺ transference number (from 0.16 to 0.45) of the electrolyte, providing a new idea for the study of organic/inorganic composite solid electrolyte. The framework employs polymer as a binder, while an interfacial phase exists between the ceramic particles, thereby impeding the transmission of lithium ions. Further, Wu and co-workers^[250]

prepared a 3D coral structure Al-doped LLZO, which was subsequently filled with PVDF-LiClO₄ electrolyte (Figure 20e). The construction of the CSE with 3D structure increases the σ_{Li^+} up to 1.51 × 10⁻⁴ S cm⁻¹, higher than that of the LLZO-free electrolyte (3.6 × 10⁻⁵ S cm⁻¹) and the CSE incorporated with the same percentage of nano-particles (7.5 × 10⁻⁵ S cm⁻¹). The solid-state Li||LFP battery exhibits a high capacity retention rate of 95.2% after 200 cycles (1 C; RT). The 3D framework structure based on electrospinning technology also exhibits ceramic/ceramic discontinuity upon removal of the polymer template, thereby resulting in a disruption in the transmission of Li⁺. It is imperative to investigate novel methodologies for the synthesis of 3D continuous LLZO.

3D printing and removing templates (in Section 2 for details) can yield a 3D skeleton with a continuous structure. Polymers (starch, polyvinyl alcohol, poly(methyl methacrylate), etc.), cellulose, porous sponges, silk, and graphite that can be completely removed at low temperatures are selected as common template materials.^[47,251] For instance, silk serves as a template for the fabrication of 3D LLZO with improved continuity (Figure 20f).^[252] The flexible CSE with a sandwich structure of PEO+LiTFSI/3D LLZO/PEO+LiTFSI achieves both a wide electrochemical window of 5.1 V and excellent cycling stability (≈71.5% after 500 cycles at 1 C) (Figure 20g,h). As outlined in Section 4.3.1, precise control of the electrolyte thickness within the range of 20–50 μm is crucial for achieving high energy density SSBs. However, the mechanical strength of the thin and brittle LLZO skeleton is exceedingly poor. The conventional approach of employing a polymer backfill 3D ceramic skeleton for constructing the CSE often results in fractures upon removing the CSE from the mold. In contrast, in situ curing offers an effective solution to tackle this issue. Utilizing polyvinyl butyral (PVB) as the polymer template, Chen et al.^[253] fabricated a 3D continuous nanocrystalline structure of Li_{6.5}La₃Zr_{1.5}Ta_{0.5}O₁₂ with a thickness of ≈50 μm by employing tape-casting and ultra-fast high-temperature sintering (Figure 20i–k). The precursor solution chosen for in situ curing was either DOL with a ring structure or PEGDA with a C=C double bond. This enabled the synthesis of a series of copolymers through ring-opening or double-bond cleavage of polymer monomers facilitated by catalysts/initiators. The resulting CSE exhibited exceptional flexibility and ductility, effectively reducing the electrode/electrolyte interface resistance. Bao et al.^[15u] fabricated a flexible and self-supporting Li_{6.5}La₃Zr_{1.5}Ta_{0.5}O₁₂ ceramic skeleton with an ultra-thin thickness of 12 μm by tape-casting method and subsequent removal of the PVB polymer template. The ethoxylated trimethylolpropane triacrylate polymer was incorporated into the LLZO skeleton by UV curing to enhance its mechanical strength and reduce interface impedance. Ultimately, the ultra-thin flexible CSE with a high ceramic content demonstrates a t_{Li^+} up to 0.83 and a high σ_{Li^+} of 1.19 × 10⁻³ S cm⁻¹ (Figure 20l,m). However, a remaining issue of these strategies is the highly distorted and closed porous structure, which can limit the polymer permeability and thus the ion-conducting behavior.

Therefore, the vertical array structure that is perpendicular to the electrode interface has gained much attention in the research community.^[254] Shen and co-workers prepared a 3D vertically aligned LLZO skeleton using freeze tape casting (Figure 20n).^[255] At RT, the Li-ion conductivities of pure polymer electrolyte,

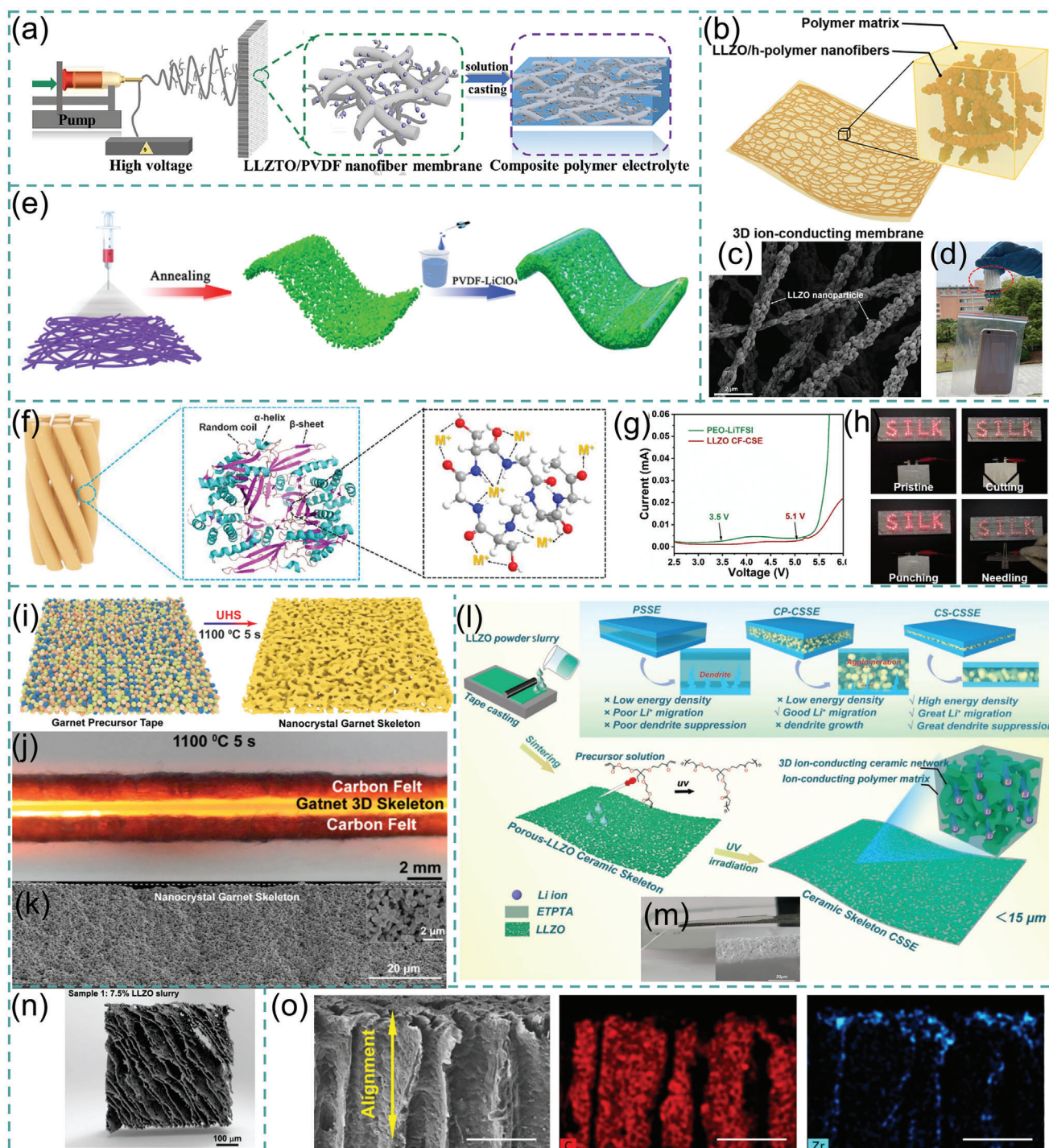


Figure 20. a) Schematic illustration for the preparation of the CSE. Reproduced with permission.^[248] Copyright 2020, Elsevier. b) 3D ion-conducting membrane; c) High magnification SEM image; d) Digital photos of composite electrolyte. Reproduced with permission.^[249] Copyright 2021, American Chemical Society. e) Schematic illustration for the preparation procedures of electrolyte. Reproduced with permission.^[250] Copyright 2020, American Chemical Society. f) Adsorption mechanism of metal ions on the silk fabric template; g) Linear sweep voltammetry curve; h) Safety tests under extreme conditions of flexible pouch-cell batteries. Reproduced with permission.^[252] Copyright 2022, Elsevier. i) Schematic illustration of the preparation of 3D porous LLZO skeletons by ultra-fast high-temperature sintering; j) A digital photograph of the LLZO skeleton membrane captured during the sintering process; k) Cross-sectional SEM images of the 3D nanocrystal LLZTO framework. Reproduced with permission.^[253] Copyright 2024, Elsevier. l) Schematic illustration for three different electrolyte structures and schematic diagram of symmetrical battery; m) Flexibility test of the LLZO ceramic skeleton. Reproduced with permission.^[255] Copyright 2019, American Chemical Society. n) Morphology of the pores fabricated using LLZO slurries. Reproduced with permission.^[255] Copyright 2019, American Chemical Society. o) SEM image and its corresponding energy-dispersive X-ray spectroscopy images of the sample. Reproduced with permission.^[256] Copyright 2019, American Chemical Society.

LLZO powder/polymer composite electrolyte, and LLZO skeleton/polymer composite electrolyte are 3.6×10^{-6} , 5.3×10^{-6} , and $2.0 \times 10^{-5} \text{ S cm}^{-1}$, respectively. The contribution of the vertical array structure to Li-ion conductivity has been confirmed. Dai et al.^[256] fabricated vertical LLZO arrays with low bending and high surface area using expandable compressed wood as the template (Figure 20o). PEO-based polymer electrolyte was then well permeated into the vertical channels of the garnet skeleton, forming the CSE membrane that exhibits good flexibility.

The organic/inorganic composite solid electrolyte exhibits the flexibility and processability of polymer electrolytes, along with the high Li-ion conductivity of ceramic electrolytes. This combination makes it a promising candidate for large-scale applications in the field of solid-state electrolytes. However, CSEs with low ceramic content typically have lower Li-ion conductivity and Li-ion transference numbers. The organic-inorganic composite solid electrolyte, characterized by a 3D skeleton structure as the main body, has witnessed notable advancements in recent years. Notably, the thickness of this electrolyte can be reduced to $<20 \mu\text{m}$ while retaining a certain degree of flexibility, thereby paving the way for potential industrial applications. However, due to the intricate composition of the organic-inorganic CSE, it is still imperative to make further advancements in highly sensitive technical approaches for exploring the underlying mechanism of Li-ion transport.

5. Conclusions and Future Perspectives

LLZO, a garnet inorganic solid electrolyte, is a promising candidate material poised to replace liquid electrolytes. This is due to its impressive attributes, including the high Li-ion conductivity at RT, excellent chemical stability to Li anodes, robust mechanical strength, superior thermal stability, and wide electrochemical window. Extensive investigations have been conducted to unveil the underlying mechanisms governing Li-ion transport and enhance Li-ion conductivity through techniques such as element doping, surface modification, interface engineering as well as constructing composite structures. Researchers have also endeavored to reduce costs through refining preparation methods or lowering the sintering temperature, while simultaneously shortening synthesis time. Nevertheless, garnet electrolytes still present numerous unresolved challenges and unanswered questions. Therefore, we outline a future perspective that aims to bridge the gap toward practical applications in high-energy-density and high-power-density lithium metal batteries (Figure 21).

1) Obstruction of ion transportation: Li_2CO_3 . At present, a series of effective methods have been developed for the surface treatment of LLZO after contamination in moist air. However, most of the methods can only temporarily remove the Li_2CO_3 . Further, it is noted that the removal of surface Li_2CO_3 without eliminating changes in lattice parameters cannot restore the Li-ion conductivity of LLZO to its original levels. Another way is to provide dry storage conditions. For example, drying rooms represent a feasible solution for large-scale LLZO storage at present, but the high operational costs rendering them less accessible for certain universities or institutes. Therefore, the challenge is how to improve the chemical stability of the

LLZO solid-state electrolyte in the atmospheric environment to eradicate the production of Li_2CO_3 . Future research endeavors must prioritize the pursuit of comprehensive solutions capable of eliminating all adverse effects associated with LLZO solid-state electrolytes.

2) Interface issues: The enhancement of Li-ion conductivity has encountered limitations, making further progress challenging via methods such as element doping and structural control. Therefore, future research efforts focus on alternative avenues to resolve interface compatibility with both the anode and cathode, as well as developing low-temperature and/or short-time sintering technology. Notably, interface-related challenges have long plagued the development of all-solid-state batteries, often compounded by difficulties in observing interface behavior that has perplexed researchers.

Efforts to optimize the interface of solid-state electrolytes and establish robust interface contact between solid-state electrolytes and electrodes can reduce interfacial resistance. Furthermore, this optimization can mitigate issues such as interface polarization, structural deterioration of electrode material, and the formation of anode dendrites. At present, the mechanisms governing charge transfer at these interfaces remain a subject of debate. One of the biggest challenges lies in the difficulty of viewing the interface dynamics in real-time. To resolve this limitation, advanced in situ interface characterization techniques offering high temporal and spatial resolution such as in situ microscopy, in situ X-ray, in situ neutron, and in situ spectroscopy are employed in conjunction with high-throughput theoretical calculations. These approaches aim to elucidate the chemical reaction kinetics occurring at the interface. To ensure the integrity of the measurement and prevent contamination of solid-state electrolyte and electrode materials caused due to external environmental factors, enhancing testing accuracy and reproducibility is a critical research objective moving forward.

3) Composite cathode: The construction of composite cathode holds significant promise in reducing interface impedance between the electrode and electrolyte while concurrently mitigating the degradation of solid-state electrolyte and electrode materials. This approach has gained increasing popularity and will be a central focus of future research efforts. However, the investigation of the cathode side requires further understanding of the intricate ion transport mechanism and the influence of active material and solid-state electrolyte particle size on composite cathode performance. Simultaneously, there exists an inaccuracy in the method of cathode material selection for SSBs. For instance, many wide voltage windows observed experimentally result from dynamic factors, obscuring the true electrochemical behavior. Additionally, the kinetics of decomposition reactions at the cathode can be sluggish, leading to varying degrees of impact on electrochemical stability. This phenomenon can result in an overestimation of experimental measurements and can misguide cathode selection.

Therefore, it is anticipated that future research directions will involve the integration of first-principles calculations, molecular dynamics, finite-element analysis, and/or machine-learning

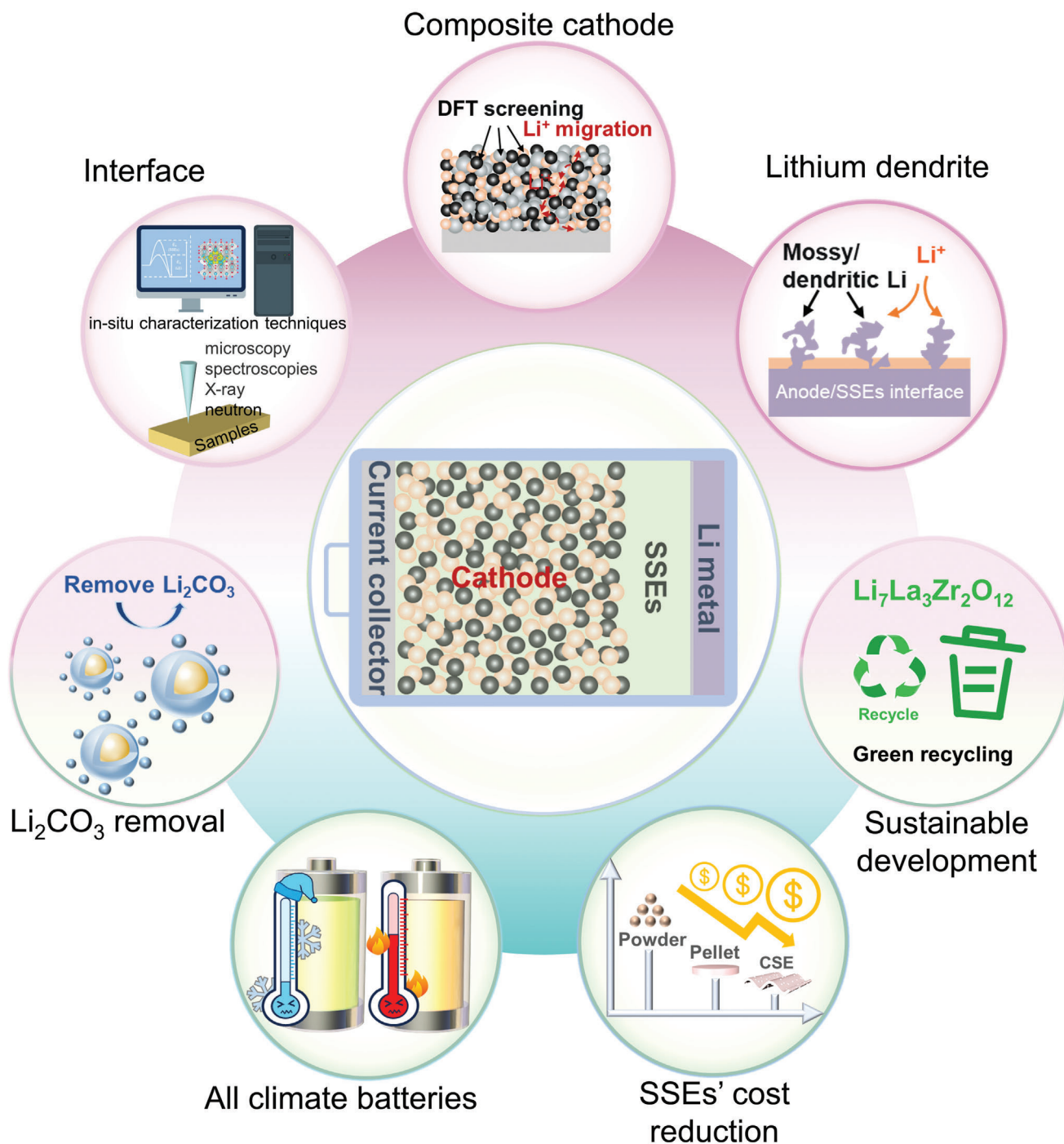


Figure 21. Key research areas for garnet LLZO-based electrolytes prior to practical integration in solid-state batteries.

techniques to further enhance our understanding of reaction mechanisms at the atomic level and facilitate the design of target materials. This interdisciplinary approach holds great potential for advancing the field and unlocking new possibilities in SSEs.

4) Lithium dendrites growth: Currently, the problem of short circuits caused by lithium dendrites penetrating LLZO re-

mains unresolved, despite the high mechanical strength and density of LLZO electrolytes. Efforts to inhibit the generation of lithium dendrites involve strategies such as increasing the density of solid-state electrolytes through coating primary powder or adding sintering additives. Additionally, reducing the electronic conductivity and promoting monocrystalline crystallization of solid-state electrolytes can also help deter dendrite formation. However, these studies

are riddled with challenges, mainly due to the complexity of dendrite generation in solid-state electrolytes. Consequently, a more holistic approach to inhibiting lithium dendrites is warranted.

To experimentally study the growth of lithium dendrites in solid-state electrolytes, the observation techniques must possess high spatial resolution, the ability to observe in operando, the ability to thoroughly analyze the crystal structure, band structure and other properties of the material. Characterization of materials in these situations is challenging and often requires in situ characterization techniques (i.e., in situ scanning electron microscopy, in situ X-ray photoelectron spectroscopy, in situ nuclear magnetic resonance, time-resolved electrostatic force microscopy and Kelvin probe force microscopy, etc.) and combined with theoretical methods namely DFT and finite-element analysis.

5) Sustainable development: Sustainability is a pressing concern within the context of LLZO production. Currently, industrial LLZO production relies primarily on the SSR combined with the high-energy ball milling method. However, this approach raises significant environmental pollution and safety issues due to the substantial generation of organic gases during mass production. A possible solution is to combine the high-energy ball mill with a water-cooled machine to minimize the volatilization of organic solvents.

Moreover, there is a notable absence of proper recycling mechanisms. Due to the lack of proper recycling, the short-circuited LLZO pellets that have undergone complex synthesis steps are usually discarded, resulting in the waste of resources and energy. Thus, the realm of LLZO recycling remains largely uncharted territory. Considering the core role of solid-state electrolyte reuse in the sustainable development of SSBs, it is imperative to develop recycling strategies for LLZO, aiming to maximize the longevity and efficiency of LLZO materials while minimizing waste and environmental impact.

6) Reducing cost: Minimize expenses of solid-state batteries is a paramount goal in the current landscape. Some enterprises and research institutes such as Zhejiang Fengli New Energy Technology Co., LTD., Qingtao Energy and Qingdao University, have made significant strides in achieving large-scale production of tonnage LLZO. Unfortunately, the cost associated with processing solid-state electrolytes remains a considerable challenge, accounting for $\approx 70\%$ of the overall manufacturing expenses for SSBs. For instance, the current cost of one kilogram of LLZO stands at \$2000. This high cost can be attributed to several factors, including heavy reliance on imported raw materials in LLZO production, lengthy sintering time, high sintering temperature, the substantial use of “master powder” used during sintering, and the introduction of imported equipment. While full batteries based on LLZO electrolytes are expected to deliver high energy density and excellent cycle stability, the poor processability and fragile defects of garnet LLZO have posed challenges during battery assembly.

To address these issues, the development of composite solid electrolytes comprising garnet LLZO and polymer solid-state electrolytes has emerged as a promising commercial prospect. Effective composite electrolytes must be designed to be thin (with a thickness of $< 30 \mu\text{m}$) and exhibit rapid Li^+ migration capability to compete with commercially available liquid electrolytes. In terms of cost reduction, solvent-free technology is a promising strategy as it circumvents the use of harmful organic solvents. Leveraging existing equipment and techniques, it becomes feasible to produce composite solid electrolytes at a lower cost. Regarding battery pack configuration, the adoption of a bipolar stacking strategy has shown potential allowing for reduced usage of accessory components. This configuration can lead to higher energy density, higher voltage output, and, consequently, a reduction in cell assembly costs.

7) Operating temperature range: To meet the operational demands of electric vehicles across diverse weather conditions, it is necessary for solid-state batteries to achieve robust performance in all-climate condition. Nevertheless, the low temperature performance of LLZO-based electrolytes is still challenging mainly because the transport of lithium ions within the solid-state electrolyte and across the solid–solid interfaces is severely hindered due to the significantly decreased ionic transportation kinetics. Additionally, the influence of electronic conductivity on low-temperature solid-state batteries remains unclear. Thus, in order to accelerate the development and application of solid-state batteries, it is pivotal to delve into the mechanisms governing the behavior at low temperatures. The intricacies of low-temperature solid-state batteries is a crucial step in advancing their technology and ensuring their viability in a wide range of environmental conditions.

Acknowledgements

This work was supported by National Natural Science Foundation of China (Grant no. 52277215, Grant no. 52377206, Grant no. 52122702), and China Postdoctoral Science Foundation (No. 2023M730884).

Open access funding enabled and organized by Projekt DEAL.

Conflict of Interest

The authors declare no conflict of interest.

Keywords

garnet solid-state electrolytes, interfaces, Li-ion conductivity, material and structure design, solid-state batteries

Received: April 9, 2024

Revised: April 9, 2024

Published online:

[1] Y. Zhu, Y. Han, Q. Guo, H. Wang, H. Jiang, H. Jiang, W. Sun, C. Zheng, K. Xie, *Electrochim. Acta* **2021**, *394*, 139123.

[2] a) Y. X. Wu, Y. Li, Y. Wang, Q. Liu, Q. G. Chen, M. H. Chen, *J. Energy Chem.* **2022**, *64*, 62; b) M. He, Z. Cui, C. Chen, Y. Li, X. Guo, *J. Mater. Chem. A* **2018**, *6*, 11463.

- [3] a) M. J. Wang, E. Carmona, A. Gupta, P. Albertus, J. Sakamoto, *Nat. Commun.* **2020**, *11*, 5201; b) C. Yang, K. Fu, Y. Zhang, E. Hitz, L. Hu, *Adv. Mater.* **2017**, *29*, 1701169.
- [4] a) Y. Xiao, Y. Wang, S.-H. Bo, J. C. Kim, L. J. Miara, G. Ceder, *Nat. Rev. Mater.* **2019**, *5*, 105; b) C. Wang, K. Fu, S. P. Kammampata, D. W. McOwen, A. J. Samson, L. Zhang, G. T. Hitz, A. M. Nolan, E. D. Wachsman, Y. Mo, V. Thangadurai, L. Hu, *Chem. Rev.* **2020**, *120*, 4257.
- [5] a) R. Murugan, V. Thangadurai, W. Weppner, *Angew. Chem., Int. Ed.* **2007**, *46*, 7778; b) J. Awaka, N. Kijima, H. Hayakawa, J. Akimoto, *J. Solid State Chem.* **2009**, *182*, 2046; c) Y. Jin, P. J. McGinn, *J. Power Sources* **2011**, *196*, 8683; d) I. Kokal, M. Somer, P. H. L. Notten, H. T. Hintzen, *Solid State Ion.* **2011**, *185*, 42; e) J. Wolfenstine, E. Rangasamy, J. L. Allen, J. Sakamoto, *J. Power Sources* **2012**, *208*, 193; f) J. Wolfenstine, J. B. Ratchford, E. Rangasamy, J. S. Sakamoto, J. L. Allen, *Mater. Chem. Phys.* **2012**, *134*, 571; g) L. Dhivya, N. Janani, B. Palanivel, R. Murugan, *AIP Adv.* **2013**, *3*, 082155; h) S. Ramakumar, L. Satyanarayana, S. V. Manorama, R. Murugan, *Phys. Chem. Chem. Phys.* **2013**, *15*, 11327; i) C. Bernuy-Lopez, W. Manalastas Jr., J. M. Lopez del Amo, A. Aguadero, F. Aguesse, J. A. Kilner, *Chem. Mat.* **2014**, *26*, 3610; j) Y. Zhang, F. Chen, R. Tu, Q. Shen, L. Zhang, *J. Power Sources* **2014**, *268*, 960; k) M. Kotobuki, M. Koishi, *Ceram. Int.* **2014**, *40*, 5043; l) S.-W. Baek, J.-M. Lee, T. Y. Kim, M.-S. Song, Y. Park, *J. Power Sources* **2014**, *249*, 197; m) Y. Zhang, J. Cai, F. Chen, R. Tu, Q. Shen, X. Zhang, L. Zhang, *J. Alloy. Compd.* **2015**, *644*, 793; n) K. Tadanaga, H. Egawa, A. Hayashi, M. Tatsumisago, J. Mosa, M. Aparicio, A. Duran, *J. Power Sources* **2015**, *273*, 844; o) Y. Li, Z. Wang, Y. Cao, F. Du, C. Chen, Z. Cui, X. Guo, *Electrochim. Acta* **2015**, *180*, 37; p) Y. Zhang, F. Chen, R. Tu, Q. Shen, X. Zhang, L. Zhang, *Solid State Ion.* **2016**, *284*, 53; q) M. Rawlence, I. Garbayo, S. Buecheler, J. L. M. Rupp, *Nanoscale* **2016**, *8*, 14746; r) C. Shao, Z. Yu, H. Liu, Z. Zheng, N. Sun, C. Diaio, *Electrochim. Acta* **2017**, *225*, 345; s) J.-F. Wu, W. K. Pang, V. K. Peterson, L. Wei, X. Guo, *ACS Appl. Mater. Interfaces* **2017**, *9*, 12461; t) X. Chen, T. Wang, W. Lu, T. Cao, M. Xue, B. Li, C. Zhang, *J. Alloy. Compd.* **2018**, *744*, 386; u) L. Bai, W. Xue, Y. Xue, H. Qin, Y. Li, Y. Li, J. Sun, *ChemElectroChem* **2018**, *5*, 3918; v) J. M. Weller, J. A. Whetten, C. K. Chan, *ACS Appl. Energy Mater.* **2018**, *1*, 552; w) S. Song, B. Chen, Y. Ruan, J. Sun, L. Yu, Y. Wang, J. Thokchom, *Electrochim. Acta* **2018**, *270*, 501; x) Y. Luo, X. Li, Y. Zhang, L. Ge, H. Chen, L. Guo, *Electrochim. Acta* **2019**, *294*, 217; y) X. Xiang, F. Chen, Q. Shen, L. Zhang, C. Chen, *Mater. Res. Express* **2019**, *6*, 085546; z) Y. Zhao, J. Yan, W. Cai, Y. Lai, J. Song, J. Yu, B. Ding, *Energy Storage Mater.* **2019**, *23*, 306; aa) X. Huang, Y. Lu, Z. Song, K. Rui, Q. Wang, T. Xiu, M. E. Badding, Z. Wen, *Energy Storage Mater.* **2019**, *22*, 207; ab) L. Yang, Q. Dai, L. Liu, D. Shao, K. Luo, S. Jamil, H. Liu, Z. Luo, B. Chang, X. Wang, *Ceram. Int.* **2020**, *46*, 10917; ac) X. Ma, Y. Xu, B. Zhang, X. Xue, C. Wang, S. He, J. Lin, L. Yang, *J. Power Sources* **2020**, *453*, 227881; ad) F. Shen, W. Guo, D. Zeng, Z. Sun, J. Gao, J. Li, B. Zhao, B. He, X. Han, *ACS Appl. Mater. Interfaces* **2020**, *12*, 30313; ae) J. M. Weller, J. A. Whetten, C. K. Chan, *ACS Appl. Mater. Interfaces* **2020**, *12*, 953; af) L. Ni, Z. Wu, C. Zhang, *Materials* **2021**, *14*, 1671; ag) L. Zhuang, X. Huang, Y. Lu, J. Tang, Y. Zhou, X. Ao, Y. Yang, B. Tian, *Ceram. Int.* **2021**, *47*, 22768; ah) E. A. Il'ina, E. D. Lylin, A. A. Kabanov, *J. Phys.: Conf. Ser.* **2021**, *1967*, 012011; ai) J. Li, J. Zhang, H. Zhai, X. Tang, G. Tan, *J. Eur. Ceram. Soc.* **2022**, *42*, 1568; aj) E. Ilina, E. Lyalin, M. Vlasov, A. Kabanov, K. Okhotnikov, E. Sherstobitova, M. Zobel, *ACS Appl. Energy Mater.* **2022**, *5*, 2959; ak) Y. Zhou, X. Li, Y. Yang, X. Huang, B. Tian, *ACS Appl. Energy Mater.* **2022**, *5*, 13817; al) O. Sharifi, M. Golmohammad, M. Soozandeh, A. S. Mehranjani, *J. Solid State Electrochem.* **2023**, *27*, 2433; am) X. Tao, L. Yang, J. Liu, Z. Zang, P. Zeng, C. Zou, L. Yi, X. Chen, X. Liu, X. Wang, *J. Alloy. Compd.* **2023**, *937*, 168380; an) N. Hoinkis, J. Schuhmacher, T. Fuchs, S. Leukel, C. Loho, A. Roters, F. H. Richter, J. Janek, *ACS Appl. Mater. Interfaces* **2023**, *15*, 28692; ao) Z. Xu, X. Hu, B. Fu, K. Khan, J. Wu, T. Li, H. Zhou, Z. Fang, M. Wu, *J. Mater.omics* **2023**, *9*, 651; ap) K. Ma, B. Chen, C.-X. Li, V. Thangadurai, *J. Mater. Chem. A* **2024**, *12*, 3601.
- [6] N. Kamaya, K. Homma, Y. Yamakawa, M. Hirayama, R. Kanno, M. Yonemura, T. Kamiyama, Y. Kato, S. Hama, K. Kawamoto, A. Mitsui, *Nat. Mater.* **2011**, *10*, 682.
- [7] Y. Kato, S. Hori, T. Saito, K. Suzuki, M. Hirayama, A. Mitsui, M. Yonemura, H. Iba, R. Kanno, *Nat. Energy* **2016**, *1*, 16030.
- [8] S. Kundu, A. Kraysberg, Y. Ein-Eli, *J. Solid State Electrochem.* **2022**, *26*, 1809.
- [9] M. A. K. L. Dissanayake, R. P. Gunawardane, H. H. Sumathipala, A. R. West, *Solid State Ion.* **1995**, *76*, 215.
- [10] a) R. Chen, A. M. Nolan, J. Lu, J. Wang, X. Yu, Y. Mo, L. Chen, X. Huang, H. Li, *Joule* **2020**, *4*, 812; b) M. Chen, Z. Yue, Y. Wu, Y. Wang, Y. Li, Z. Chen, *Sustainable Mater. Technol.* **2023**, *36*, e00587.
- [11] a) Y. Zhao, Y. Ding, Y. Li, L. Peng, H. R. Byon, J. B. Goodenough, G. Yu, *Chem. Soc. Rev.* **2015**, *44*, 7968; b) J. Schnell, F. Tietz, C. Singer, A. Hofer, N. Billot, G. Reinhart, *Energy Environ. Sci.* **2019**, *12*, 1818.
- [12] V. Thangadurai, H. Kaack, W. J. F. Weppner, *J. Am. Ceram. Soc.* **2003**, *86*, 437.
- [13] J.-H. Choi, C.-H. Lee, J.-H. Yu, C.-H. Doh, S.-M. Lee, *J. Power Sources* **2015**, *274*, 458.
- [14] J. Su, X. Huang, Z. Song, T. Xiu, M. E. Badding, J. Jin, Z. Wen, *Ceram. Int.* **2019**, *45*, 14991.
- [15] a) V. Thangadurai, W. Weppner, *Adv. Funct. Mater.* **2005**, *15*, 107; b) V. Thangadurai, W. Weppner, *J. Am. Ceram. Soc.* **2005**, *88*, 411; c) V. Thangadurai, W. Weppner, *J. Power Sources* **2005**, *142*, 339; d) V. Thangadurai, W. Weppner, *J. Solid State Chem.* **2006**, *179*, 974; e) R. Murugan, W. Weppner, P. Schmid-Beurmann, V. Thangadurai, *Mater. Sci. Eng. B* **2007**, *143*, 14; f) R. Murugan, V. Thangadurai, W. Weppner, *Appl. Phys. A* **2008**, *91*, 615; g) J. Awaka, A. Takashima, K. Kataoka, N. Kijima, Y. Idemoto, J. Akimoto, *Chem. Lett.* **2011**, *40*, 60; h) J. Wolfenstine, J. Ratchford, E. Rangasamy, J. Sakamoto, J. L. Allen, *Mater. Chem. Phys.* **2012**, *134*, 571; i) T. Thompson, J. Wolfenstine, J. L. Allen, M. Johannes, A. Huq, I. N. David, J. Sakamoto, *J. Mater. Chem. A* **2014**, *2*, 13431; j) M. Kubicek, A. Wächter-Welzl, D. Rettenwander, R. Wagner, S. Berendts, R. Uecker, G. Amthauer, H. Hutter, J. Fleig, *Chem. Mater.* **2017**, *29*, 7189; k) T. Yang, J. Zheng, Q. Cheng, Y.-Y. Hu, C. K. Chan, *ACS Appl. Mater. Interfaces* **2017**, *9*, 21773; l) X. Tao, Y. Liu, W. Liu, G. Zhou, J. Zhao, D. Lin, C. Zu, O. Sheng, W. Zhang, H. W. Lee, Y. Cui, *Nano Lett.* **2017**, *17*, 2967; m) W. Zhang, J. Nie, F. Li, Z. L. Wang, C. Sun, *Nano Energy* **2018**, *45*, 413; n) J. Zheng, Y.-Y. Hu, *ACS Appl. Mater. Interfaces* **2018**, *10*, 4113; o) H. Shen, E. Yi, M. Amores, L. Cheng, N. Tamura, D. Y. Parkinson, G. Chen, K. Chen, M. Doeff, *J. Mater. Chem. A* **2019**, *7*, 20861; p) J. Li, K. Zhu, Z. Yao, G. Qian, J. Zhang, K. Yan, J. Wang, *Ionics* **2019**, *26*, 1101; q) X. He, F. Yan, M. Gao, Y. Shi, G. Ge, B. Shen, J. Zhai, *ACS Appl. Mater. Interfaces* **2021**, *13*, 42212; r) K. K. Fu, Y. Gong, J. Dai, A. Gong, X. Han, Y. Yao, C. Wang, Y. Wang, Y. Chen, C. Yan, Y. Li, E. D. Wachsman, L. Hu, *Proc. Natl. Acad. Sci. U. S. A.* **2016**, *113*, 7094; s) F. Han, J. Yue, C. Chen, N. Zhao, X. Fan, Z. Ma, T. Gao, F. Wang, X. Guo, C. Wang, *Joule* **2018**, *2*, 497; t) F. Sun, Y. Yang, S. Zhao, Y. Wang, M. Tang, Q. Huang, Y. Ren, H. Su, B. Wang, N. Zhao, X. Guo, H. Yu, *ACS Energy Lett.* **2022**, *7*, 2835; u) C. Bao, C. Zheng, M. Wu, Y. Zhang, J. Jin, H. Chen, Z. Wen, *Adv. Energy Mater.* **2023**, *13*, 2204028; v) L. Cheng, E. J. Crumlin, W. Chen, R. Qiao, H. Hou, S. F. Lux, V. Zorba, R. Russo, R. Kostecki, Z. Liu, K. Persson, W. Yang, J. Cabana, T. Richardson, G. Chen, M. Doeff, *Phys. Chem. Chem. Phys.* **2014**, *16*, 18294; w) B. Liu, L. Zhang, S. Xu, D. W. McOwen, Y. Gong, C. Yang, G. R. Pastel, H. Xie, K. Fu, J. Dai, C. Chen, E. D. Wachsman, L. Hu, *Energy Storage Mater.* **2018**, *14*, 376.
- [16] X. Huang, J. Su, Z. Song, T. Xiu, J. Jin, M. E. Badding, Z. Wen, *Ceram. Int.* **2021**, *47*, 2123.

- [17] a) C. Liu, K. Rui, C. Shen, M. E. Badding, G. Zhang, Z. Wen, *J. Power Sources* **2015**, 282, 286; b) Y. Wang, W. Lai, *J. Power Sources* **2015**, 275, 612.
- [18] X. Huang, Y. Lu, J. Jin, S. Gu, T. Xiu, Z. Song, M. E. Badding, Z. Wen, *ACS Appl. Mater. Interfaces* **2018**, 10, 17147.
- [19] C. Li, Y. Liu, J. He, K. S. Brinkman, *J. Alloy. Compd.* **2017**, 695, 3744.
- [20] Y. Tian, Y. Zhou, Y. Liu, C. Zhao, W. Wang, Y. Zhou, *Solid State Ion.* **2020**, 354, 115407.
- [21] a) G. Özsin, K. B. Dermenci, S. Turan, *J. Therm. Anal. Calorim.* **2021**, 146, 1405; b) Z. Li, H.-M. Huang, J.-K. Zhu, J.-F. Wu, H. Yang, L. Wei, X. Guo, *ACS Appl. Mater. Interfaces* **2019**, 11, 784; c) Z. Cao, W. Wu, Y. Li, J. Zhao, W. He, J. Liu, H. Zhang, G. Li, *Ionics* **2020**, 26, 4247.
- [22] a) C. K. Chan, T. Yang, J. M. Weller, *Electrochim. Acta* **2017**, 253, 268; b) Y. X. Song, Y. Shi, J. Wan, S. Y. Lang, X. C. Hu, H. J. Yan, B. Liu, Y. G. Guo, R. Wen, L. J. Wan, *Energy Environ. Sci.* **2019**, 12, 2496.
- [23] L. Cheng, C. H. Wu, A. Jarry, W. Chen, Y. F. Ye, J. F. Zhu, R. Kostecki, K. Persson, J. H. Guo, M. Salmeron, G. Y. Chen, M. Doeff, *ACS Appl. Energy Mater.* **2015**, 7, 17649.
- [24] L. Cheng, W. Chen, M. Kunz, K. Persson, N. Tamura, G. Chen, M. Doeff, *ACS Appl. Mater. Interfaces* **2015**, 7, 2073.
- [25] J. Sakamoto, E. Rangasamy, H. Kim, Y. Kim, J. Wolfenstine, *Nanotechnology* **2013**, 24, 424005.
- [26] L. Lu, C. Sun, J. Hao, Z. Wang, S. F. Mayer, M. T. Fernández-Díaz, J. A. Alonso, B. Zou, *Energy Environ. Sci.* **2023**, 6, e12364.
- [27] A. Mali, A. Ataie, *Ceram. Int.* **2004**, 30, 1979.
- [28] W. Wen, J.-M. Wu, *RSC Adv.* **2014**, 4, 58090.
- [29] a) K.-w. Kim, S.-H. Yang, M. Y. Kim, M. S. Lee, J. Lim, D. R. Chang, H.-S. Kim, *J. Ind. Eng. Chem* **2016**, 36, 279; b) T. Wang, X. Zhang, Z. Yao, J. Li, K. Zhu, J. Wang, K. Yan, *J. Electron. Mater.* **2020**, 49, 4910.
- [30] A. Rajaeiyan, M. M. Bagheri-Mohagheghi, *Adv. Manuf.* **2013**, 1, 176.
- [31] a) X. Zhang, T.-S. Oh, J. W. Fergus, *J. Electrochem. Soc.* **2019**, 166, A3753; b) C. Shao, H. Liu, Z. Yu, Z. Zheng, N. Sun, C. Diao, *Solid State Ion.* **2016**, 287, 13.
- [32] X. Liu, N. Fechler, M. Antonietti, *Chem. Soc. Rev.* **2013**, 42, 8237.
- [33] J. M. Weller, C. K. Chan, *ACS Appl. Energy Mater.* **2020**, 3, 6466.
- [34] Y. Zhang, Y. Deng, X. Gao, C. Lv, D. Luo, X. Xiang, *J. Alloys Compd.* **2021**, 881, 160620.
- [35] Y. Zhang, A. Liu, Z. Shi, S. Ge, J. Zhang, *Int. J. Appl. Ceram. Technol.* **2022**, 19, 320.
- [36] a) G. L. Messing, S. C. Zhang, G. V. Jayanthi, *J. Am. Ceram. Soc.* **1993**, 76, 2707; b) M. Botros, R. Djenadic, O. Clemens, M. Möller, H. Hahn, *J. Power Sources* **2016**, 309, 108.
- [37] R. Djenadic, M. Botros, C. Benel, O. Clemens, S. Indris, A. Choudhary, T. Bergfeldt, H. Hahn, *Solid State Ion.* **2014**, 263, 49.
- [38] A. La Monaca, A. Paoletta, A. Guerfi, F. Rosei, K. Zaghbi, *Electrochim. Commun.* **2019**, 104, 106483.
- [39] T. Yang, Z. D. Gordon, Y. Li, C. K. Chan, *J. Phys. Chem. C* **2015**, 119, 14947.
- [40] T. Rosenthal, J. M. Weller, C. K. Chan, *Ind. Eng. Chem. Res.* **2019**, 58, 17399.
- [41] Y. Gong, K. Fu, S. Xu, J. Dai, T. R. Hamann, L. Zhang, G. T. Hitz, Z. Fu, Z. Ma, D. W. McOwen, X. Han, L. Hu, E. D. Wachsman, *Mater. Today* **2018**, 21, 594.
- [42] X. Yang, X. Han, Z. Chen, L. Zhou, B. Zhao, H. Su, W. Jiao, *Mater. Lett.* **2018**, 217, 271.
- [43] A. A. AbdelHamid, J. L. Cheong, J. Y. Ying, *Nano Energy* **2020**, 71, 104633.
- [44] S. Song, Y. Wu, W. Tang, F. Deng, J. Yao, Z. Liu, R. Hu, Alamus, Z. W, L. Lu, N. Hu, *ACS Sustain. Chem. Eng.* **2019**, 7, 7163.
- [45] H. Xie, C. Yang, K. K. Fu, Y. Yao, F. Jiang, E. Hitz, B. Liu, S. Wang, L. Hu, *Adv. Energy Mater.* **2018**, 8, 1703474.
- [46] D. Cai, D. Wang, Y. Chen, S. Zhang, X. Wang, X. Xia, J. Tu, *Chem. Eng. J.* **2020**, 394, 124993.
- [47] R. Li, S. Guo, L. Yu, L. Wang, D. Wu, Y. Li, X. Hu, *Adv. Mater. Interfaces* **2019**, 6, 1900200.
- [48] S. Deville, *Adv. Eng. Mater.* **2008**, 10, 155.
- [49] G. Shao, D. A. H. Hanaor, X. Shen, A. Gurlo, *Adv. Mater.* **2020**, 32, 1907176.
- [50] R.-J. Pei, Y.-F. Li, T. Song, N. Chen, R. Yang, *J. Alloys Compd.* **2023**, 933, 167639.
- [51] M. Bitzer, T. Van Gestel, S. Uhlenbruck, B. H. Peter, *Thin Solid Films* **2016**, 615, 128.
- [52] a) C. Deviannapoorani, L. Dhivya, S. Ramakumar, R. Murugan, *J. Power Sources* **2013**, 240, 18; b) X. Ma, Y. Xu, *Electrochim. Acta* **2022**, 409, 139986.
- [53] M. P. O'Callaghan, A. S. Powell, J. J. Titman, G. Z. Chen, E. J. Cussen, *Chem. Mat.* **2008**, 20, 2360.
- [54] F. Chen, J. Li, Z. Huang, Y. Yang, Q. Shen, L. Zhang, *J. Phys. Chem. C* **2018**, 122, 1963.
- [55] V. K. Jayaraman, D. G. Porob, A. S. Prakash, *ACS Appl. Energy Mater.* **2023**, 6, 11442.
- [56] M. Xu, M. Park, J.-M. Lee, T. Kim, Y. Park, E. Ma, *Phys. Rev. B* **2012**, 85, 052301.
- [57] K. Meier, T. Laino, A. Curioni, *J. Phys. Chem. C* **2014**, 118, 6668.
- [58] J. Han, J. Zhu, Y. Li, X. Yu, S. Wang, G. Wu, H. Xie, S. C. Vogel, F. Izumi, K. Momma, *Chem. Commun.* **2012**, 48, 9840.
- [59] a) W. Xia, B. Xu, H. Duan, Y. Guo, H. Kang, H. Li, H. Liu, *ACS Appl. Mater. Interfaces* **2016**, 8, 5335; b) V. Thangadurai, S. Narayanan, D. Pinzaru, *Chem. Soc. Rev.* **2014**, 43, 4714; c) P. Posch, S. Lunghammer, S. Berendts, S. Ganschow, G. J. Redhammer, A. Wilkening, M. Lerch, B. Gadermaier, D. Rettenwander, H. M. R. Wilkening, *Energy Storage Mater.* **2020**, 24, 220.
- [60] I. N. David, T. Thompson, J. Wolfenstine, J. L. Allen, J. Sakamoto, *J. Am. Ceram. Soc.* **2015**, 98, 1209.
- [61] a) M. Sato, R. Garcia-Mendez, J. Sakamoto, *J. Asian Ceram. Soc.* **2020**, 8, 793; b) J. L. Allen, J. Wolfenstine, E. Rangasamy, J. Sakamoto, *J. Power Sources* **2012**, 206, 315.
- [62] Y. Kim, H. Jo, J. L. Allen, H. Choe, J. Wolfenstine, J. Sakamoto, *J. Am. Ceram. Soc.* **2016**, 99, 1367.
- [63] H. C. Lee, N. R. Oh, A. R. Yoo, Y. Kim, J. Sakamoto, *J. Korean Phys. Soc.* **2018**, 73, 1535.
- [64] E. Rangasamy, J. Wolfenstine, J. Sakamoto, *Solid State Ion.* **2012**, 206, 28.
- [65] D. Gao, R. Wu, P. Chen, T. Hong, J. Cheng, *Mater. Res. Express* **2019**, 6, 125539.
- [66] R. Kali, A. Mukhopadhyay, *J. Power Sources* **2014**, 247, 920.
- [67] T. Clemenceau, N. Andriamady, P. K. MK, A. Badran, V. Avila, K. Dahl, M. Hopkins, X. Vendrell, D. Marshall, R. Raj, *Scr. Mater.* **2019**, 172, 1.
- [68] J.-H. Seo, H. Nakaya, Y. Takeuchi, Z. Fan, H. Hikosaka, R. Rajagopalan, E. D. Gomez, M. Iwasaki, C. A. Randall, *J. Eur. Ceram. Soc.* **2020**, 40, 6241.
- [69] F. Chen, J. Li, Y. Zhang, D. Yang, Q. Shen, L. Zhang, Proceedings of the 3rd Pan American Materials Congress, Springer, Cham, Switzerland **2017**.
- [70] Y. Zhang, F. Chen, D. Yang, W. Zha, J. Li, Q. Shen, X. Zhang, L. Zhang, *J. Electrochem. Soc.* **2017**, 164, A1695.
- [71] a) A. Sharafi, H. M. Meyer, J. Nanda, J. Wolfenstine, J. Sakamoto, *J. Power Sources* **2016**, 302, 135; b) T. Thompson, A. Sharafi, M. D. Johannes, A. Huq, J. L. Allen, J. Wolfenstine, J. Sakamoto, *Adv. Energy Mater.* **2015**, 5, 1500096.
- [72] a) X. Zhang, X. Guan, Y. Zhang, W. Zhang, Q. Shen, *J. Power Sources* **2023**, 556, 232459; b) N. C. Rosero-Navarro, T. Yamashita, A. Miura, M. Higuchi, K. Tadanaga, *J. Am. Ceram. Soc.* **2017**, 100, 276; c) S. Kumazaki, Y. Iriyama, K.-H. Kim, R. Murugan, K. Tanabe, K. Yamamoto, T. Hirayama, Z. Ogumi, *Electrochim. Commun.* **2011**, 13, 509.

- [73] a) C. Li, A. Ishii, L. Roy, D. Hitchcock, Y. Meng, K. Brinkman, *J. Mater. Sci.* **2020**, *55*, 16470; b) X. Huang, Y. Lu, Z. Song, T. Xiu, M. E. Badding, Z. Wen, *J. Energy Chem.* **2019**, *39*, 8; c) J. Han, J. C. Kim, *Chem. Commun.* **2020**, *56*, 15197; d) K. B. Dermenci, *Mater. Chem. Phys.* **2022**, *281*, 125910.
- [74] a) Z. Qin, Y. Xie, X. Meng, D. Qian, D. Mao, Z. Zheng, L. Wan, Y. Huang, *ACS Appl. Mater. Interfaces* **2022**, *14*, 40959; b) Z. Qin, X. Meng, Y. Xie, D. Qian, H. Deng, D. Mao, L. Wan, Y. Huang, *Energy Storage Mater.* **2021**, *43*, 190.
- [75] L. Yang, X. Huang, C. Zou, X. Tao, L. Liu, K. Luo, P. Zeng, Q. Dai, Y. Li, L. Yi, Z. Luo, X. Wang, *Ceram. Int.* **2021**, *47*, 18196.
- [76] P. Zhao, Y. Wen, J. Cheng, G. Cao, Z. Jin, H. Ming, Y. Xu, X. Zhu, *J. Power Sources* **2017**, *344*, 56.
- [77] Z. Huang, L. Chen, B. Huang, B. Xu, G. Shao, H. Wang, Y. Li, C. A. Wang, *ACS Appl. Mater. Interfaces* **2020**, *12*, 56118.
- [78] K. Zhang, T. Xu, H. Zhao, S. Zhang, Z. Zhang, Y. Zhang, Z. Du, Z. Li, *Int. J. Energy Res.* **2020**, *44*, 9177.
- [79] S. Chen, X. Hu, W. Bao, Z. Wang, Q. Yang, L. Nie, X. Zhang, J. Zhang, Y. Jiang, Y. Han, C. Wan, J. Xie, Y. Yu, W. Liu, *Cell Rep. Phys. Sci.* **2021**, *2*, 100569.
- [80] a) E. Yi, W. Wang, J. Kieffer, R. M. Laine, *J. Mater. Chem. A* **2016**, *4*, 12947; b) Y. Zhang, F. Chen, J. Li, L. Zhang, J. Gu, D. Zhang, K. Saito, Q. Guo, P. Luo, S. Dong, *Electrochim. Acta* **2018**, *261*, 137.
- [81] B. Karasulu, S. P. Emge, M. F. Groh, C. P. Grey, A. J. Morris, *J. Am. Chem. Soc.* **2020**, *142*, 3132.
- [82] E. Yi, W. Wang, J. Kieffer, R. M. Laine, *J. Power Sources* **2017**, *352*, 156.
- [83] Amardeep, S. K. A. Mukhopadhyay, *Scr. Mater.* **2019**, *162*, 214.
- [84] a) X. Cheng, J. Huang, W. Qiang, B. Huang, *Ceram. Int.* **2020**, *46*, 3731; b) A. Paulus, S. Kammler, S. Heuer, M. C. Paulus, P. Jakes, J. Granwehr, R.-A. Eichel, *J. Electrochem. Soc.* **2019**, *166*, A5403.
- [85] E. Rangasamy, J. Wolfenstine, J. Allen, J. Sakamoto, *J. Power Sources* **2013**, *230*, 261.
- [86] M. Huang, W. Xu, Y. Shen, Y. H. Lin, C. W. Nan, *Electrochim. Acta* **2014**, *115*, 581.
- [87] A. Dumon, M. Huang, Y. Shen, C. W. Nan, *Solid State Ion.* **2013**, *243*, 36.
- [88] C. Fritsch, T. Zinkevich, S. Indris, M. Etter, V. Baran, T. Bergfeldt, M. Knapp, H. Ehrenberg, A.-L. Hansen, *RSC Adv.* **2021**, *11*, 30283.
- [89] D. Wang, G. Zhong, O. Dolotko, Y. Li, M. J. McDonald, J. Mi, R. Fu, Y. Yang, *J. Mater. Chem. A* **2014**, *2*, 20271.
- [90] Y. Zhang, J. Deng, D. Hu, F. Chen, Q. Shen, L. Zhang, S. Dong, *Electrochim. Acta* **2019**, *296*, 823.
- [91] H. Buschmann, S. Berendts, B. Mogwitz, J. Janek, *J. Power Sources* **2012**, *206*, 236.
- [92] B. Yan, M. Kotobuki, J. Liu, *Mater. Technol.* **2016**, *31*, 623.
- [93] D. Han, Z. Zhao, W. Wang, H. Wang, J. Shi, L. Zheng, *Ceram. Int.* **2023**, *49*, 7935.
- [94] T. Wang, W. Qiu, Q. Feng, K. Huang, X. Zhao, Q. Bao, Y. Wang, G. Zhu, J. Liu, *J. Mater. Chem. A* **2019**, *7*, 17008.
- [95] M. Wang, J. Sakamoto, *Ionics* **2018**, *24*, 1861.
- [96] L. J. Miara, W. D. Richards, Y. E. Wang, G. Ceder, *Chem. Mat.* **2015**, *27*, 4040.
- [97] X. Yang, D. Kong, Z. Chen, Y. Sun, Y. Liu, *J. Mater. Sci. Mater. Electron.* **2017**, *29*, 1523.
- [98] C. A. Geiger, E. Alekseev, B. Lazic, M. Fisch, T. Armbruster, R. Langner, M. Fechtelkord, N. Kim, T. Pettke, W. Weppner, *Inorg. Chem.* **2011**, *50*, 1089.
- [99] M. Ashuri, M. Golmohammad, A. Soleimany Mehranjani, M. Faghihi Sani, *J. Mater. Sci. Mater. Electron.* **2021**, *32*, 6369.
- [100] N. Bernstein, M. D. Johannes, K. Hoang, *Phys. Rev. Lett.* **2012**, *109*, 205702.
- [101] Y. Sun, O. Gorobstov, L. Mu, D. Weinstock, R. Bouck, W. Cha, N. Bouklas, F. Lin, A. Singer, *Nano Lett.* **2021**, *21*, 4570.
- [102] C. Im, D. Park, H. Kim, J. Lee, *J. Energy Chem.* **2018**, *27*, 1501.
- [103] J. F. Wu, E. Y. Chen, Y. Yu, L. Liu, Y. Wu, W. K. Pang, V. K. Peterson, X. Guo, *ACS Appl. Mater. Interfaces* **2017**, *9*, 1542.
- [104] H. El Shinawi, J. Janek, *J. Power Sources* **2013**, *225*, 13.
- [105] R. Wagner, G. J. Redhammer, D. Rettenwander, A. Senyshyn, W. Schmidt, M. Wilkening, G. Amthauer, *Chem. Mat.* **2016**, *28*, 1861.
- [106] C.-Y. Huang, Y.-T. Tseng, H.-Y. Lo, J.-K. Chang, W.-W. Wu, *Nano Energy* **2020**, *71*, 104625.
- [107] a) D. Rettenwander, G. Redhammer, F. Preishuber-Pflugl, L. Cheng, L. Miara, R. Wagner, A. Welzl, E. Suard, M. M. Doeff, M. Wilkening, J. Fleig, G. Amthauer, *Chem. Mat.* **2016**, *28*, 2384; b) S. Qin, X. Zhu, Y. Jiang, M. e. Ling, Z. Hu, J. Zhu, *Appl. Phys. Lett.* **2018**, *112*, 113901.
- [108] S. Narayanan, F. Ramezanipour, V. Thangadurai, *J. Phys. Chem. C* **2012**, *116*, 20154.
- [109] E. Rangasamy, J. Wolfenstine, J. Allen, J. Sakamoto, *J. Power Sources* **2013**, *230*, 261.
- [110] J. M. Valle, J. Sakamoto, *Solid State Ion.* **2020**, *345*, 115170.
- [111] a) B. P. Dubej, A. Sahoo, V. Thangadurai, Y. Sharma, *Solid State Ion.* **2020**, *351*, 115339; b) P. Zhao, G. Cao, Z. Jin, H. Ming, Y. Wen, Y. Xu, X. Zhu, Y. Xiang, S. Zhang, *Mater. Des.* **2018**, *139*, 65.
- [112] B. Zhang, R. Tan, L. Yang, J. Zheng, K. Zhang, S. Mo, Z. Lin, F. Pan, *Energy Storage Mater.* **2018**, *10*, 139.
- [113] M. Huang, M. Shoji, Y. Shen, C.-W. Nan, H. Munakata, K. Kanamura, *J. Power Sources* **2014**, *261*, 206.
- [114] X. Huang, Z. Song, T. Xiu, M. E. Badding, Z. Wen, *Ceram. Int.* **2019**, *45*, 56.
- [115] S. Ohta, T. Kobayashi, T. Asaoka, *J. Power Sources* **2011**, *196*, 3342.
- [116] K. Ishiguro, Y. Nakata, M. Matsui, I. Uechi, Y. Takeda, O. Yamamoto, N. Imanishi, *J. Electrochem. Soc.* **2013**, *160*, A1690.
- [117] A. Logéat, T. Köhler, U. Eisele, B. Stiaszny, A. Harzer, M. Tovar, A. Senyshyn, H. Ehrenberg, B. Kozinsky, *Solid State Ion.* **2012**, *206*, 33.
- [118] K. Miwa, R. Asahi, *Phys. Rev. Mater.* **2018**, *2*, 105404.
- [119] B. Gao, R. Jalem, Y. Tateyama, *ACS Appl. Mater. Interfaces* **2020**, *12*, 16350.
- [120] Y. Zhu, J. G. Connell, S. Tepavcevic, P. Zapol, R. Garcia-Mendez, N. J. Taylor, J. Sakamoto, B. J. Ingram, L. A. Curtiss, J. W. Freeland, D. D. Fong, N. M. Markovic, *Adv. Energy Mater.* **2019**, *9*, 1803440.
- [121] Y. Li, J.-T. Han, C.-A. Wang, H. Xie, J. B. Goodenough, *J. Mater. Chem.* **2012**, *22*, 15357.
- [122] S. Adams, R. P. Rao, *J. Mater. Chem.* **2012**, *22*, 1426.
- [123] R. Inada, A. Takeda, Y. Yamazaki, S. Miyake, Y. Sakurai, V. Thangadurai, *ACS Appl. Energy Mater.* **2020**, *3*, 12517.
- [124] S.-K. Jung, H. Gwon, H. Kim, G. Yoon, D. Shin, J. Hong, C. Jung, J.-S. Kim, *Nat. Commun.* **2022**, *13*, 7638.
- [125] S. Han, Z. Wang, Y. Ma, Y. Miao, X. Wang, Y. Wang, Y. Wang, *J. Adv. Ceram.* **2023**, *12*, 1201.
- [126] Y. Feng, L. Yang, Z. Yan, D. Zuo, Z. Zhu, L. Zeng, Y. Zhu, J. Wan, *Energy Storage Mater.* **2023**, *63*, 103053.
- [127] C. Chen, Y. Sun, L. He, M. Kotobuki, E. Hanc, Y. Chen, K. Zeng, L. Lu, *ACS Appl. Energy Mater.* **2020**, *3*, 4708.
- [128] W. Lan, H. Fan, V. W.-h. Lau, J. Zhang, J. Zhang, R. Zhao, H. Chen, *Sustain. Energ. Fuels* **2020**, *4*, 1812.
- [129] L. Buannic, B. Orayech, J.-M. L. Del Amo, J. Carrasco, N. A. Katcho, F. Aguesse, W. Manalastas, W. Zhang, J. Kilner, A. Llordés, *Chem. Mat.* **2017**, *29*, 1769.
- [130] X. Zhou, L. Huang, O. Elkedim, Y. Xie, Y. Luo, Q. Chen, Y. Zhang, Y. Chen, *J. Alloys Compd.* **2022**, *891*, 161906.
- [131] a) L. Shen, L. Wang, Z. Wang, C. Jin, L. Peng, X. Pan, J. Sun, R. Yang, *Solid State Ion.* **2019**, *339*, 114992; b) C. Lin, Y. Tang, J. Song, L. Han, J. Yu, A. Lu, *Appl. Phys. A* **2018**, *124*, 439.
- [132] Y. Meesala, Y.-K. Liao, A. Jena, N.-H. Yang, W. K. Pang, S.-F. Hu, H. Chang, C.-E. Liu, S.-C. Liao, J.-M. Chen, X. Guo, R.-S. Liu, *J. Mater. Chem. A* **2019**, *7*, 8589.

- [133] a) L. Cai, Z. Y. Wen, K. Rui, *J. Inorg. Mater.* **2015**, *30*, 995; b) Y. Wang, W. D. Richards, S. P. Ong, L. J. Miara, J. C. Kim, Y. Mo, G. Ceder, *Nat. Mater.* **2015**, *14*, 1026.
- [134] Y. Yang, H. Zhu, *ACS Appl. Energy Mater.* **2022**, *5*, 15086.
- [135] X. Ma, Y. Xu, *ACS Appl. Mater. Interfaces* **2022**, *14*, 2939.
- [136] A. Sodhiya, A. K. Singh, S. Soni, S. Patel, R. Kumar, *Appl. Phys. A* **2022**, *128*, 639.
- [137] Y. Lu, X. Meng, J. A. Alonso, M. T. Fernández-Díaz, C. Sun, *ACS Appl. Mater. Interfaces* **2018**, *11*, 2042.
- [138] B. Xu, H. Duan, W. Xia, Y. Guo, H. Kang, H. Li, H. Liu, *J. Power Sources* **2016**, *302*, 291.
- [139] S. H. Yang, M. Y. Kim, D. H. Kim, H. Y. Jung, H. M. Ryu, J. H. Han, M. S. Lee, H.-S. Kim, *J. Ind. Eng. Chem.* **2017**, *56*, 422.
- [140] P. Badami, J. M. Weller, A. Wahab, G. Redhammer, L. Ladenstein, D. Rettenwander, M. Wilkening, C. K. Chan, A. N. M. Kannan, *ACS Appl. Mater. Interfaces* **2020**, *12*, 48580.
- [141] Y. Tian, Y. Zhou, W. Wang, Y. Zhou, *Ceram. Int.* **2022**, *48*, 963.
- [142] a) S. Yu, D. J. Siegel, *Chem. Mat.* **2017**, *29*, 9639; b) C. Ma, K. Chen, C. Liang, C.-W. Nan, R. Ishikawa, K. More, M. Chi, *Energy Environ. Sci.* **2014**, *7*, 1638.
- [143] Y. Zhu, Degree Thesis, University of Maryland, College Park **2018**.
- [144] B. Gao, R. Jalem, H. K. Tian, Y. Tateyama, *Adv. Energy Mater.* **2022**, *12*, 2102151.
- [145] W. E. Tenhaeff, E. Rangasamy, Y. Wang, A. P. Sokolov, J. Wolfenstine, J. Sakamoto, N. J. Dudney, *ChemElectroChem* **2014**, *1*, 375.
- [146] X. Xiang, Y. Liu, F. Chen, W. Yang, J. Yang, X. Ma, D. Chen, K. Su, Q. Shen, L. Zhang, *J. Eur. Ceram. Soc.* **2020**, *40*, 3065.
- [147] L. J. Miara, S. P. Ong, Y. Mo, W. D. Richards, Y. Park, J.-M. Lee, H. S. Lee, G. Ceder, *Chem. Mat.* **2013**, *25*, 3048.
- [148] S. R. Yeandel, B. J. Chapman, P. R. Slater, P. Goddard, *J. Phys. Chem. C* **2018**, *122*, 27811.
- [149] J. M. Tarascon, M. Armand, *Nature* **2001**, *414*, 359.
- [150] C. Monroe, J. Newman, *J. Electrochem. Soc.* **2005**, *152*, A396.
- [151] a) S. Yu, R. D. Schmidt, R. Garcia-Mendez, E. Herbert, N. J. Dudney, J. B. Wolfenstine, J. Sakamoto, D. J. Siegel, *Chem. Mat.* **2015**, *28*, 197; b) J. E. Ni, E. D. Case, J. S. Sakamoto, E. Rangasamy, J. B. Wolfenstine, *J. Mater. Sci.* **2012**, *47*, 7978.
- [152] A. Sharafi, S. Yu, M. Naguib, M. Lee, C. Ma, H. M. Meyer, J. Nanda, M. Chi, D. J. Siegel, J. Sakamoto, *J. Mater. Chem. A* **2017**, *5*, 13475.
- [153] L. Truong, M. A. Howard, O. Clemens, K. S. Knight, P. R. Slater, V. Thangadurai, *J. Mater. Chem.* **2013**, *1*, 13469.
- [154] L. Truong, V. Thangadurai, *Chem. Mater.* **2011**, *23*, 3970.
- [155] H. Huo, J. Luo, V. Thangadurai, X. Guo, C.-W. Nan, X. Sun, *ACS Energy Lett.* **2020**, *5*, 252.
- [156] W. Xia, B. Xu, H. Duan, X. Tang, Y. Guo, H. Kang, H. Li, H. Liu, *J. Am. Ceram. Soc.* **2017**, *100*, 2832.
- [157] a) Y. Li, X. Chen, A. Dolocan, Z. Cui, S. Xin, L. Xue, H. Xu, K. Park, J. B. Goodenough, *J. Am. Chem. Soc.* **2018**, *140*, 6448; b) R. H. Brugge, F. M. Pesci, A. Cavallaro, C. Sole, M. A. Isaacs, G. Kerherve, R. S. Weatherup, A. Agüadero, *J. Mater. Chem. A* **2020**, *8*, 14265; c) T. Krauskopf, H. Hartmann, W. G. Zeier, J. Janek, *ACS Appl. Mater. Interfaces* **2019**, *11*, 14463.
- [158] B. Chen, J. Zhang, T. Zhang, R. Wang, J. Zheng, Y. Zhai, X. Liu, *Adv. Sci.* **2023**, *10*, 2207056.
- [159] H. Huo, Y. Chen, N. Zhao, X. Lin, J. Luo, X. Yang, Y. Liu, X. Guo, X. Sun, *Nano Energy* **2019**, *61*, 119.
- [160] Y. Ruan, Y. Lu, Y. Li, C. Zheng, J. Su, J. Jin, T. Xiu, Z. Song, M. E. Badding, Z. Wen, *Adv. Funct. Mater.* **2020**, *31*, 2007815.
- [161] G. Yu, Y. Wang, K. Li, S. Sun, S. Sun, J. Chen, L. Pan, Z. Sun, *Chem. Eng. J.* **2022**, *430*, 132874.
- [162] Y.-N. Yang, Y.-X. Li, Y.-Q. Li, T. Zhang, *Nat. Commun.* **2020**, *11*, 5519.
- [163] J. Zhang, C. Wang, M. Zheng, M. Ye, H. Zhai, J. Li, G. Tan, X. Tang, X. Sun, *Nano Energy* **2022**, *102*, 107672.
- [164] Z. Bi, Q. Sun, M. Jia, M. Zuo, N. Zhao, X. Guo, *Adv. Funct. Mater.* **2022**, *32*, 2208751.
- [165] H. Duan, W. P. Chen, M. Fan, W. P. Wang, L. Yu, S. J. Tan, X. Chen, Q. Zhang, S. Xin, L. J. Wan, *Angew. Chem.* **2020**, *132*, 12167.
- [166] M. Cai, J. Jin, T. Xiu, Z. Song, M. E. Badding, Z. Wen, *Energy Storage Mater.* **2022**, *47*, 61.
- [167] A. A. Delluva, J. Kulberg-Savercool, A. Holewinski, *Adv. Funct. Mater.* **2021**, *31*, 2103716.
- [168] J. Biao, B. Han, Y. Cao, Q. Li, G. Zhong, J. Ma, L. Chen, K. Yang, J. Mi, Y. Deng, M. Liu, W. Lv, F. Kang, Y.-B. He, *Adv. Mater.* **2023**, *35*, 2208951.
- [169] S. Vema, F. N. Sayed, S. Nagendran, B. Karagoz, C. Sternemann, M. Paulus, G. Held, C. P. Grey, *ACS Energy Lett.* **2023**, *8*, 3476.
- [170] N. Zhang, G. Ren, L. Li, Z. Wang, P. Yu, X. Li, J. Zhou, H. Zhang, L. Zhang, Z. Liu, X. Liu, *Nat. Commun.* **2024**, *15*, 2777.
- [171] Y. Zhou, A. Gao, M. Duan, X. Zhang, M. Yang, L. Gong, J. Chen, S. Song, F. Xie, H. Jia, Y. Wang, *ACS Appl. Mater. Interfaces* **2023**, *15*, 45465.
- [172] a) X. Min, H. Huo, R. Li, J. Zhou, Y. Hu, C. Dai, *J. Electroanal. Chem.* **2016**, *774*, 76; b) Z. Chen, D. Steinle, H.-D. Nguyen, J.-K. Kim, A. Mayer, J. Shi, E. Paillard, C. Ioioiu, S. Passerini, D. Bresser, *Nano Energy* **2020**, *77*, 105129.
- [173] a) Z.-J. Zhang, S.-L. Chou, Q.-F. Gu, H.-K. Liu, H.-J. Li, K. Ozawa, J.-Z. Wang, *ACS Appl. Mater. Interfaces* **2014**, *6*, 22155; b) X. Li, J. Liu, M. N. Banis, A. Lushington, R. Li, M. Cai, X. Sun, *Energy Environ. Sci.* **2014**, *7*, 768.
- [174] a) C. Shen, Y. Liu, W. Li, X. Liu, J. Xie, J. Jiang, Y. Jiang, B. Zhao, J. Zhang, *J. Colloid Interface Sci.* **2022**, *615*, 1; b) Y. Liang, J. Cai, D. Liu, Z. Chen, *Energy Technol.* **2021**, *9*, 2100422.
- [175] Y. Liu, N. Xu, Z. Cheng, H. Xie, Y. Ma, M. Wu, Y. Zhang, L. Chen, *Electrochim. Acta* **2020**, *349*, 136251.
- [176] Y.-F. Deng, S.-X. Zhao, D.-H. Hu, C.-W. Nan, *J. Solid State Electrochem.* **2013**, *18*, 249.
- [177] Y.-F. Deng, S.-X. Zhao, Y.-H. Xu, C.-W. Nan, *J. Mater. Chem. A* **2014**, *2*, 18889.
- [178] K. Heo, J.-S. Lee, H.-S. Kim, J. Kim, J. Lim, *J. Electrochem. Soc.* **2017**, *164*, A2398.
- [179] Y. Wei, J. Cheng, D. Li, Y. Li, Z. Zeng, H. Liu, H. Zhang, F. Ji, X. Geng, J. Lu, L. Ci, *Adv. Funct. Mater.* **2023**, *33*, 2214775.
- [180] J. Zhou, X. Sun, K. Wang, *Ceram. Int.* **2016**, *42*, 10228.
- [181] Y.-X. Bai, J. Zhang, Y.-B. Yang, R. Yang, Y.-L. Yan, J. Wang, *J. Alloys Compd.* **2020**, *843*, 154915.
- [182] Y. Cheng, R. Li, D. Mu, J. Ren, J. Liu, C. Dai, *J. Electrochem. Soc.* **2017**, *164*, A1545.
- [183] K. Heo, J.-S. Lee, H.-S. Kim, M.-Y. Kim, H. Jeong, J. Kim, J. Lim, *J. Electrochem. Soc.* **2018**, *165*, A2955.
- [184] Z. Zhao, Z. Wen, X. Liu, H. Yang, S. Chen, C. Li, H. Lv, F. Wu, B. Wu, D. Mu, *Chem. Eng. J.* **2021**, *405*, 127031.
- [185] F. Chen, Y. Zhang, Q. Hu, S. Cao, S. Song, X. Lu, Q. Shen, *J. Solid State Chem.* **2021**, *301*, 122341.
- [186] a) J. Sastre, X. Chen, A. Aribia, A. N. Tiwari, Y. E. Romanyuk, *ACS Appl. Mater. Interfaces* **2020**, *12*, 36196; b) T. Kato, T. Hamanaka, K. Yamamoto, T. Hirayama, F. Sagane, M. Motoyama, Y. Iriyama, *J. Power Sources* **2014**, *260*, 292; c) C. Hansel, S. Afyon, J. L. Rupp, *Nanoscale* **2016**, *8*, 18412.
- [187] H. Wakayama, H. Yonekura, Y. Kawai, *Chem. Mat.* **2016**, *28*, 4453.
- [188] D. Wang, Q. Sun, J. Luo, J. Liang, Y. Sun, R. Li, K. Adair, L. Zhang, R. Yang, S. Lu, H. Huang, X. Sun, *ACS Appl. Mater. Interfaces* **2019**, *11*, 4954.
- [189] C.-L. Tsai, Q. Ma, C. Dellen, S. Lobe, F. Vondahlen, A. Windmüller, D. Grüner, H. Zheng, S. Uhlenbruck, M. Finsterbusch, F. Tietz, D. Fattakhova-Rohlfing, H. P. Buchkremer, O. Guillon, *Sustain. Energ. Fuels* **2019**, *3*, 280.

- [190] A.-Y. Hou, C.-Y. Huang, C.-L. Tsai, C.-W. Huang, R. Schierholz, H.-Y. Lo, H. Tempel, H. Kungl, R.-A. Eichel, J.-K. Chang, W.-W. Wu, *Adv. Sci.* **2023**, *10*, 2205012.
- [191] G. T. Hitz, D. W. McOwen, L. Zhang, Z. Ma, Z. Fu, Y. Wen, Y. Gong, J. Dai, T. R. Hamann, L. Hu, E. D. Wachsman, *Mater. Today* **2019**, *22*, 50.
- [192] K. Fu, Y. Gong, G. T. Hitz, D. W. McOwen, Y. Li, S. Xu, Y. Wen, L. Zhang, C. Wang, G. Pastel, J. Dai, B. Liu, H. Xie, Y. Yao, E. D. Wachsman, L. Hu, *Energy Environ. Sci.* **2017**, *10*, 1568.
- [193] E. Yi, H. Shen, S. Heywood, J. Alvarado, D. Y. Parkinson, G. Chen, S. W. Sofie, M. M. Doeff, *ACS Appl. Energy Mater.* **2020**, *3*, 170.
- [194] K. J. Kim, J. L. M. Rupp, *Energy Environ. Sci.* **2020**, *13*, 4930.
- [195] Z. Jin, X. Kong, H. Huang, Y. Jiang, W. Xiang, Y. Xu, L. Zhang, R. Peng, C. Wang, *Energy Storage Mater.* **2023**, *59*, 102788.
- [196] H. Zhang, F. Okur, C. Cancellieri, L. P. H. Jeurgens, A. Parrilli, D. T. Karabay, M. Nesvadba, S. Hwang, A. Neels, M. V. Kovalenko, K. V. Kravchyk, *Adv. Sci.* **2023**, *10*, 2205821.
- [197] K. V. Kravchyk, D. T. Karabay, M. V. Kovalenko, *Sci. Rep.* **2022**, *12*, 1177.
- [198] K. V. Kravchyk, F. Okur, M. V. Kovalenko, *ACS Energy Lett.* **2021**, *6*, 2202.
- [199] R. A. Jonson, E. Yi, F. Shen, M. C. Tucker, *Energy Fuels* **2021**, *35*, 8982.
- [200] Y. Wu, K. Wang, K. Liu, Y. Long, C. Yang, H. Zhang, W. Pan, W. Si, H. Wu, *Adv. Energy Mater.* **2023**, *13*, 2300809.
- [201] X. Yan, Z. Li, Z. Wen, W. Han, *J. Phys. Chem. C* **2017**, *121*, 1431.
- [202] J. Sastre, A. Priebe, M. Döbeli, J. Michler, A. N. Tiwari, Y. E. Romanyuk, *Adv. Mater. Interfaces* **2020**, *7*, 2000425.
- [203] M. Saccoccio, J. Yu, Z. Lu, S. C. T. Kwok, J. Wang, K. K. Yeung, M. M. F. Yuen, F. Ciucci, *J. Power Sources* **2017**, *365*, 43.
- [204] a) S. Lobe, C. Dellen, M. Finsterbusch, H. G. Gehrke, D. Sebold, C. L. Tsai, S. Uhlenbruck, O. Guillon, *J. Power Sources* **2016**, *307*, 684; b) J. A. Oke, T.-C. Jen, *J. Mater. Res. Technol.* **2022**, *21*, 2481.
- [205] M. Du, Y. Sun, B. Liu, B. Chen, K. Liao, R. Ran, R. Cai, W. Zhou, Z. Shao, *Adv. Funct. Mater.* **2021**, *31*, 2101556.
- [206] a) F. Du, N. Zhao, Y. Li, C. Chen, Z. Liu, X. Guo, *J. Power Sources* **2015**, *300*, 24; b) S. Ohta, T. Kobayashi, J. Seki, T. Asaoka, *J. Power Sources* **2012**, *202*, 332.
- [207] K. Park, B.-C. Yu, J.-W. Jung, Y. Li, W. Zhou, H. Gao, S. Son, J. B. Goodenough, *Chem. Mat.* **2016**, *28*, 8051.
- [208] T. Demuth, T. Fuchs, F. Walther, A. Pokle, S. Ahmed, M. Malaki, A. Beyer, J. Janek, K. Volz, *Matter* **2023**, *6*, 2324.
- [209] R. Subramani, Y.-H. Tseng, Y.-L. Lee, C.-C. Chiu, S.-S. Hou, H. Teng, *J. Mater. Chem. A* **2019**, *7*, 12244.
- [210] S. Sarkar, B. Chen, C. Zhou, S. N. Shirazi, F. Langer, J. Schwenzel, V. Thangadurai, *Adv. Energy Mater.* **2023**, *13*, 2203897.
- [211] S.-S. Chi, Y. Liu, N. Zhao, X. Guo, C.-W. Nan, L.-Z. Fan, *Energy Storage Mater.* **2019**, *17*, 309.
- [212] L. Nie, S. Chen, M. Zhang, T. Gao, Y. Zhang, R. Wei, Y. Zhang, W. Liu, *Nano Res.* **2024**, *17*, 2687.
- [213] F. Wei, S. Wu, J. Zhang, H. Fan, L. Wang, V. W.-h. Lau, S. Hou, M. Zhang, J. Zhang, B. Liang, *J. Mater. Chem. A* **2021**, *9*, 17039.
- [214] Z. Chen, H.-P. Liang, Z. Lyu, N. Paul, G. Ceccio, R. Gilles, M. Zarrabeitia, A. Innocenti, M. Jasarevic, G. T. Kim, S. Passerini, D. Bresser, *Chem. Eng. J.* **2023**, *467*, 143530.
- [215] Z. Chen, G.-T. Kim, J.-K. Kim, M. Zarrabeitia, M. Kuenzel, H.-P. Liang, D. Geiger, U. Kaiser, S. Passerini, *Adv. Energy Mater.* **2021**, *11*, 2101339.
- [216] C. Deng, N. Chen, C. Hou, H. Liu, Z. Zhou, R. Chen, *Small* **2021**, *17*, 2006578.
- [217] W. Zhou, Z. Wang, Y. Pu, Y. Li, S. Xin, X. Li, J. Chen, J. B. Goodenough, *Adv. Mater.* **2019**, *31*, 1805574.
- [218] X. Yang, S. Tang, C. Zheng, F. Ren, Y. Huang, X. Fei, W. Yang, S. Pan, Z. Gong, Y. Yang, *Adv. Funct. Mater.* **2023**, *33*, 2209120.
- [219] Y. Chen, B. Ouyang, X. Li, W. Liu, B. Yang, P. Ning, Q. Xia, F. Zan, E. Kan, J. Xu, H. Xia, *ACS Appl. Mater. Interfaces* **2023**, *15*, 44962.
- [220] A. Sharafi, E. Kazyak, A. L. Davis, S. Yu, T. Thompson, D. J. Siegel, N. P. Dasgupta, J. Sakamoto, *Chem. Mat.* **2017**, *29*, 7961.
- [221] J. Li, Z. Gong, W. Xie, S. Yu, Y. Wei, D. Li, L. Yang, D. Chen, Y. Li, Y. Chen, *ACS Appl. Energy Mater.* **2023**, *6*, 12432.
- [222] a) Y. Lu, X. Huang, Y. Ruan, Q. Wang, R. Kun, J. Yang, Z. Wen, *J. Mater. Chem. A* **2018**, *6*, 18853; b) C.-L. Tsai, V. Roddatis, C. V. Chandran, Q. Ma, S. Uhlenbruck, M. Bram, P. Heitjans, O. Guillon, *ACS Appl. Mater. Interfaces* **2016**, *8*, 10617; c) W. Luo, Y. Gong, Y. Zhu, K. K. Fu, J. Dai, S. D. Lacey, C. Wang, B. Liu, X. Han, Y. Mo, *J. Am. Chem. Soc.* **2016**, *138*, 12258; d) T. Krauskopf, B. Mogwitz, C. Rosenbach, W. G. Zeier, J. Janek, *Adv. Energy Mater.* **2019**, *9*, 1902568; e) X. Han, Y. Gong, K. Fu, X. He, G. T. Hitz, J. Dai, A. Pearce, B. Liu, H. Wang, G. Rubloff, *Nat. Mater.* **2017**, *16*, 572; f) H. Xu, Y. Li, A. Zhou, N. Wu, S. Xin, Z. Li, J. B. Goodenough, *Nano Lett.* **2018**, *18*, 7414; g) K. Park, J. B. Goodenough, *Adv. Energy Mater.* **2017**, *7*, 1700732; h) J. Duan, W. Wu, A. M. Nolan, T. Wang, J. Wen, C. Hu, Y. Mo, W. Luo, Y. Huang, *Adv. Mater.* **2019**, *31*, 1807243.
- [223] Z. Wan, K. Shi, Y. Huang, L. Yang, Q. Yun, L. Chen, F. Ren, F. Kang, Y.-B. He, *J. Power Sources* **2021**, *505*, 230062.
- [224] M. Stockham, B. Dong, M. James, Y. Li, Y. Ding, E. Kendrick, P. Slater, *Dalton Trans.* **2021**, *50*, 13786.
- [225] a) Y. Liu, D. Lin, Y. Jin, K. Liu, X. Tao, Q. Zhang, X. Zhang, Y. Cui, *Sci. Adv.* **2017**, *3*, ea00713; b) B. Liu, M. Du, B. Chen, Y. Zhong, J. Zhou, F. Ye, K. Liao, W. Zhou, C. Cao, R. Cai, *Chem. Eng. J.* **2022**, *427*, 131001; c) Y. Zhang, J. Meng, K. Chen, H. Wu, J. Hu, C. Li, *ACS Energy Lett.* **2020**, *5*, 1167; d) Y. Chen, Y. Huang, H. Fu, Y. Wu, D. Zhang, J. Wen, L. Huang, Y. Dai, Y. Huang, W. Luo, *ACS Appl. Mater. Interfaces* **2021**, *13*, 28398.
- [226] O. Sreejith, R. Murugan, *J. Alloys Compd.* **2023**, *939*, 168774.
- [227] a) J. Zhu, X. Li, C. Wu, J. Gao, H. Xu, Y. Li, X. Guo, H. Li, W. Zhou, *Angew. Chem. Int. Ed.* **2020**, *60*, 3781; b) J. Gao, J. Zhu, X. Li, J. Li, X. Guo, H. Li, W. Zhou, *Adv. Funct. Mater.* **2021**, *31*, 2001918.
- [228] M. Gao, Z. Gong, H. Li, H. Zhao, D. Chen, Y. Wei, D. Li, Y. Li, L. Yang, Y. Chen, *Adv. Funct. Mater.* **2023**, *33*, 2300319.
- [229] M. Mishra, C.-W. Hsu, P. C. Rath, J. Patra, H.-Z. Lai, T.-L. Chang, C.-Y. Wang, T.-Y. Wu, T.-C. Lee, J.-K. Chang, *Electrochim. Acta* **2020**, *353*, 136536.
- [230] M. Golozar, A. Paoletta, H. Demers, S. Savoie, G. Girard, N. Delaporte, R. Gauvin, A. Guerfi, H. Lorrmann, K. Zaghib, *Sci. Rep.* **2020**, *10*, 18410.
- [231] Z. Chen, G.-T. Kim, Z. Wang, D. Bresser, B. Qin, D. Geiger, U. Kaiser, X. Wang, Z. X. Shen, S. Passerini, *Nano Energy* **2019**, *64*, 103986.
- [232] a) X. Wang, X. Hao, Y. Xia, Y. Liang, X. Xia, J. Tu, *J. Membr. Sci.* **2019**, *582*, 37; b) Z. He, L. Chen, B. Zhang, Y. Liu, L.-Z. Fan, *J. Power Sources* **2018**, *392*, 232.
- [233] J. Zhang, N. Zhao, M. Zhang, Y. Li, P. K. Chu, X. Guo, Z. Di, X. Wang, H. Li, *Nano Energy* **2016**, *28*, 447.
- [234] A. Wang, D. Pei, Z. Liu, S. Huang, G. Cao, H. Jin, S. Hou, *ACS Appl. Energy Mater.* **2023**, *6*, 8221.
- [235] a) M.-x. Jing, H. Yang, H. Chong, F. Chen, L.-k. Zhang, X.-y. Hu, F.-y. Tu, X.-q. Shen, *J. Electrochem. Soc.* **2019**, *166*, A3019; b) S. Song, X. Qin, Y. Ruan, W. Li, Y. Xu, D. Zhang, J. Thokchom, *J. Power Sources* **2020**, *461*, 228146; c) H. Xu, X. Zhang, J. Jiang, M. Li, Y. Shen, *Solid State Ion.* **2020**, *347*, 115227; d) Y. Li, K. W. Wong, K. M. Ng, *Chem. Commun.* **2016**, *52*, 4369; e) W. Liu, N. Liu, J. Sun, P.-C. Hsu, Y. Li, H.-W. Lee, Y. Cui, *Nano Lett.* **2015**, *15*, 2740.
- [236] Z. Wan, D. Lei, W. Yang, C. Liu, K. Shi, X. Hao, L. Shen, W. Lv, B. Li, Q. H. Yang, *Adv. Funct. Mater.* **2019**, *29*, 1805301.
- [237] L. Chen, Y. Li, S.-P. Li, L.-Z. Fan, C.-W. Nan, J. B. Goodenough, *Nano Energy* **2018**, *46*, 176.
- [238] R. Fan, C. Liu, K. He, S. Ho-Sum Cheng, D. Chen, C. Liao, R. K. Y. Li, J. Tang, Z. Lu, *ACS Appl. Mater. Interfaces* **2020**, *12*, 7222.

- [239] a) Y. Wang, Z. Chen, Y. Wu, Y. Li, Z. Yue, M. Chen, *ACS Appl. Mater. Interfaces* **2023**, *15*, 21526; b) Z. Huang, W. Pang, P. Liang, Z. Jin, N. Grundish, Y. Li, C.-A. Wang, *J. Mater. Chem. A* **2019**, *7*, 16425.
- [240] W. Li, C. Sun, J. Jin, Y. Li, C. Chen, Z. Wen, *J. Mater. Chem. A* **2019**, *7*, 27304.
- [241] Y. Rong, Z. Lu, C. Jin, Y. Xu, L. Peng, R. Shi, T. Gu, C. Lu, R. Yang, *ACS Sustain. Chem. Eng.* **2023**, *11*, 785.
- [242] R.-A. Tong, L. Chen, G. Shao, H. Wang, C.-A. Wang, *J. Power Sources* **2021**, *492*, 229672.
- [243] L. Peng, Z. Lu, L. Zhong, J. Jian, Y. Rong, R. Yang, Y. Xu, C. Jin, *J. Colloid Interface Sci.* **2022**, *613*, 368.
- [244] Z. Lu, L. Peng, Y. Rong, E. Wang, R. Shi, H. Yang, Y. Xu, R. Yang, C. Jin, *Energy Environ. Sci.* **2024**, *7*, e12498.
- [245] X. Yi, Y. Guo, S. Chi, S. Pan, C. Geng, M. Li, Z. Li, W. Lv, S. Wu, Q.-H. Yang, *Adv. Funct. Mater.* **2023**, *33*, 2303574.
- [246] M. Chen, W. Liu, Z. Yue, Y. Wang, Y. Wu, Y. Li, Z. Chen, *Batteries* **2023**, *9*, 270.
- [247] a) J. Yin, X. Xu, S. Jiang, H. Wu, L. Wei, Y. Li, J. He, K. Xi, Y. Gao, *Chem. Eng. J.* **2022**, *431*, 133352; b) S. Luo, E. Zhao, Y. Gu, J. Huang, Z. Zhang, L. Yang, S.-i. Hirano, *Chem. Eng. J.* **2021**, *421*, 127771.
- [248] L. Gao, J. Li, J. Ju, B. Cheng, W. Kang, N. Deng, *Compos. Sci. Technol.* **2020**, *200*, 108408.
- [249] M. Zhang, P. Pan, Z. Cheng, J. Mao, L. Jiang, C. Ni, S. Park, K. Deng, Y. Hu, K. K. Fu, *Nano Lett.* **2021**, *21*, 7070.
- [250] M. Wu, D. Liu, D. Qu, Z. Xie, J. Li, J. Lei, H. Tang, *ACS Appl. Mater. Interfaces* **2020**, *12*, 52652.
- [251] a) J. Bae, Y. Li, F. Zhao, X. Zhou, Y. Ding, G. Yu, *Energy Storage Mater.* **2018**, *15*, 46; b) L. W. Tian, J. W. Kim, S.-B. Hong, H.-H. Ryu, U.-H. Kim, Y.-K. Sun, D.-W. Kim, *Chem. Eng. J.* **2022**, *450*, 138043; c) H. Zhang, X. An, Z. Lu, L. Liu, H. Cao, Q. Xu, H. Liu, Y. Ni, *J. Power Sources* **2020**, *477*, 228752.
- [252] P. Pan, M. Zhang, Z. Cheng, L. Jiang, J. Mao, C. Ni, Q. Chen, Y. Zeng, Y. Hu, K. K. Fu, *Energy Storage Mater.* **2022**, *47*, 279.
- [253] L. Chen, X. Huang, R. Ma, W. Xiang, J. Ma, Y. Wu, D. Yang, C. Wang, W. Ping, H. Xiang, *Energy Storage Mater.* **2024**, *65*, 103140.
- [254] a) C. S. Martínez-Cisneros, B. Pandit, C. Antonelli, J. Y. Sánchez, B. Levenfeld, A. Varez, *J. Eur. Ceram. Soc.* **2021**, *41*, 7723; b) L. Buannic, M. Naviroj, S. M. Miller, J. Zagorski, K. T. Faber, A. Llordés, *J. Am. Ceram. Soc.* **2019**, *102*, 1021.
- [255] H. Shen, E. Yi, S. Heywood, D. Y. Parkinson, G. Chen, N. Tamura, S. Sofie, K. Chen, M. M. Doeff, *ACS Appl. Mater. Interfaces* **2019**, *12*, 3494.
- [256] J. Dai, K. Fu, Y. Gong, J. Song, C. Chen, Y. Yao, G. Pastel, L. Zhang, E. Wachsman, L. Hu, *ACS Mater. Lett.* **2019**, *1*, 354.



Yang Wang is currently a Ph.D. student under the supervision of Prof. Minghua Chen and Prof. Zhen Chen at Harbin University of Science and Technology. Her research interest focuses on organic/inorganic composite solid electrolyte, especially the polymer/ceramic interface modification, to enable high energy density lithium-metal batteries.



Zhen Chen is currently a professor at the Harbin University of Science and Technology. She received her B.S. degree at the Southeast University (SEU) in China in 2014, and Ph.D. degree at the Nanyang Technological University (NTU) in Singapore in 2018. From 2019 to 2022, she worked as a scientist at the Helmholtz Institute Ulm (HIU), Karlsruhe Institute of Technology (KIT) in Germany. Her research activities mainly focus on the development of key materials and relevant applications in the field of electrochemical energy storage with a special focus on developing high-performance solid-state secondary batteries.



Kai Jiang is currently a professor at Huazhong University of Science and Technology. He received his B.S. degree and Ph.D. degree from Wuhan University in 1999 and 2006, respectively. From 2007 to 2009, he worked as a visiting scientist at Auburn University in the United States. Before joining Huazhong University of Science and Technology in 2012, he worked as a postdoctoral researcher at the Massachusetts Institute of Technology. His main research directions are new energy materials and new energy storage technologies.



Zexiang Shen is a Professor at Harbin University of Science and Technology and Nanyang Technological University. He has accumulated nearly 30 years of experience in academic and research roles in China, London, and Singapore. His ongoing research interests encompass near-field Raman microscopy, plasmonics, nanomaterials and devices, graphene and nanosphere lithography, graphene-based supercapacitors and batteries. Over 200 of his papers have been published in prestigious international journals. His scholarly contributions have garnered substantial recognition, evidenced by his remarkable h-index of 121 and over 60 000 citations.



Stefano Passerini is Distinguished Senior Fellow at Karlsruhe Institute of Technology (Germany). His research focuses on the understanding and development of materials for high-energy batteries, with the goal to create sustainable energy storage systems from environmentally friendly and available materials and processes. Co-author of about 800 scientific papers (Scopus H-Index: 119; > 50 000 citations), a few book chapters and several international patents, he has been awarded the Research Award of the Electrochemical Society Battery Division. He is fellow of the International Society of Electrochemistry and the Electrochemical Society Inc., and member of the Leopoldina German Academy of Science.



Minghua Chen is professor at Harbin University of Science and Technology since 2017. He received his Ph.D. from Harbin University of Science and Technology, followed by exchange student and visiting scientist at Nanyang Technological University (NTU) from 2013 to 2016. His research interests are dielectric insulation characteristics of engineering dielectric, and the application and development of new energy materials and devices.